



**EXPERIMENTAL INVESTIGATION OF
OBLIQUE WING AERODYNAMICS AT LOW
SPEED**

THESIS

Matthew J. Dillsaver, Captain, USAF
AFIT/GAE/ENY/07-M10

**DEPARTMENT OF THE AIR FORCE
AIR UNIVERSITY**

AIR FORCE INSTITUTE OF TECHNOLOGY

Wright-Patterson Air Force Base, Ohio

APPROVED FOR PUBLIC RELEASE; DISTRIBUTION UNLIMITED

The views expressed in this thesis are those of the author and do not reflect the official policy or position of the United States Air Force, Department of Defense, or the United States Government.

AFIT/GAE/ENY/07-M10

EXPERIMENTAL INVESTIGATION OF OBLIQUE WING AERODYNAMICS AT
LOW SPEED

THESIS

Presented to the Faculty

Department of Aeronautics and Astronautics

Graduate School of Engineering and Management

Air Force Institute of Technology

Air University

Air Education and Training Command

In Partial Fulfillment of the Requirements for the
Degree of Master of Science in Aeronautical Engineering

Matthew J. Dillsaver, BSME

Captain, USAF

March 2007

APPROVED FOR PUBLIC RELEASE; DISTRIBUTION UNLIMITED.

AFIT/GAE/ENY/07-M10

EXPERIMENTAL INVESTIGATION OF OBLIQUE WING AERODYNAMICS AT
LOW SPEED

Matthew J. Dillsaver, BSME
Captain, USAF

Approved:

Dr. Milton Franke (Chairman)

date

Dr. Paul King (Member)

date

Lt. Col. Raymond Maple (Member)

date

Abstract

In an effort to increase the range of missiles and guided bombs, the USAF is looking at options for new wing configurations. One such configuration being considered is oblique wings. An oblique wing is a wing that pivots about a point on the aircraft fuselage thereby having one side swept forward and the other swept aft. Additional interest is looking at a wing only configuration that also rotates with one wing tip forward of the other. Studies have shown that this configuration can provide less drag for a given lift at both supersonic cruise and subsonic loiter conditions. This experiment focused on the low speed performance of a missile model with an oblique wing. The wing was tested at seven different sweep angles and at two different speeds. In order to simulate the missile dropping from an aircraft the model was inverted over a stationary ground plane in the tunnel and tested at the same wing obliquity angles. Stalling was found at certain conditions including sweep angles of 0, 15, and 30 deg. The ground plane was shown to result in an increase in lift as well as an increase in drag. The ground plane was also shown to add more longitudinal stability, thus making the missile better performing when dropped from an aircraft.

AFIT/GAE/ENY/07-M10

To my fiancé for all of her love and support throughout this project

Acknowledgements

I would like to thank everyone who assisted me throughout this study. I would especially like to thank my thesis advisor, Dr. Franke, for his vast knowledge and guidance. I would also like to express my sincere gratitude to Mr. Dwight Gehring, AFIT/ENY, for his invaluable help in set-up, calibration, and operation of the wind tunnel. Lastly, I would like to thank Mr. Jay Anderson for the set-up and operation of the ENY 3-D rapid prototyping machine.

Matthew J. Dillsaver

Table of Contents

	Page
Abstract	iv
Acknowledgements	vi
Table of Contents	vii
List of Figures	ix
List of Tables	xiii
List of Symbols	xiv
 I. Introduction	 1
Section 1 - Oblique Wings.....	1
Section 2 - Ground Effects.....	3
Section 3 – Research Objectives and Approach	3
 II. Literature Review	 5
Section 1 - Oblique Wings.....	5
Section 2 - Ground Effects.....	7
 III. Experimental Setup	 15
Section 1 - Wind Tunnel	15
Section 2 - Balance	17
Section 3 - Missile Model and Wing	18
Section 4 - Ground Plane	21
Section 5 - Experimental Procedure	24
Section 6 - Data Analysis.....	29
 IV. Results and Analysis.....	 30
Verification of Balance and Data Reduction Program	30
Middle Wing	34
In-Ground Effects	39
Front Wing.....	52
Uncertainty Analysis.....	58

	Page
V. Conclusions and Recommendations	60
Section 1 - Conclusions	60
Section 2 - Recommendations	61
Appendix A. Data Reduction Sample Calculation	63
Appendix B. Additional Plots	66
Appendix C. MATLAB Data Reduction Program	77
References	85
Vita	88

List of Figures

Figure	Page
Figure 1. Blohm and Voss P-202 [1].....	2
Figure 2. NASA AD-1 [4].....	2
Figure 3. Illustration of 2X length for oblique wings [1].....	5
Figure 4. Comparison of induced drag for oblique and delta wing [9].....	6
Figure 5. Airflow around wing OGE and wing IGE [1].....	8
Figure 6. Graph of Weiselsberger's induced drag formula [7].....	9
Figure 7. McCormick's induced drag factor [14].....	10
Figure 8. Conditions needing an endless belt ground plane [22].....	13
Figure 9. Wind tunnel converging section dimensions.....	16
Figure 10. AFIT wind tunnel schematic.....	16
Figure 11. Wind tunnel test section.....	17
Figure 12. Missile model mounted in tunnel.....	18
Figure 13. Airfoil profile.....	19
Figure 14. Sweep angle convention used.....	20
Figure 15. SolidWorks drawing of wing.....	21
Figure 16. Ground plane [5].....	22
Figure 17. Top view of ground plane with pieces separated [5].....	23
Figure 18. Ground plane leading edge [5].....	24
Figure 19. Tunnel coordinate system [29].....	25
Figure 20. Force directions for OGE testing at $\lambda = 0$	28
Figure 21. Force directions for IGE testing at $\lambda = 0$	28

	Page
Figure 22. Bare missile CL vs alpha - 60 mph.....	31
Figure 23. Bare missile CL vs alpha - 100 mph.....	32
Figure 24. My lambda UCAV results.....	33
Figure 25. In's lambda UCAV results [29].....	33
Figure 26. Middle wing CL vs alpha - 50 mph.....	35
Figure 27. Middle wing CL vs alpha - 60 mph.....	35
Figure 28. Middle wing CD vs alpha - 50 mph.....	36
Figure 29. Middle wing CD vs alpha - 60 mph.....	37
Figure 30. Middle wing Cm vs alpha - 50 mph.....	38
Figure 31. Middle wing Cm vs alpha - 60 mph.....	38
Figure 32. Middle wing CL vs alpha – $\lambda = 0$ deg IGE.....	40
Figure 33. Middle wing CL vs alpha – $\lambda = 15$ deg IGE.....	41
Figure 34. Middle wing CL vs alpha – $\lambda = 30$ deg IGE.....	41
Figure 35. Middle wing CL vs alpha – $\lambda = 45$ deg IGE.....	42
Figure 36. Middle wing CL vs alpha – $\lambda = 60$ deg IGE.....	42
Figure 37. Middle wing CL vs alpha – $\lambda = 75$ deg IGE.....	43
Figure 38. Middle wing CL vs alpha – $\lambda = 90$ deg IGE.....	43
Figure 39. Middle wing CD vs alpha – $\lambda = 0$ deg IGE.....	45
Figure 40. Middle wing CD vs alpha – $\lambda = 15$ deg IGE.....	45
Figure 41. Middle wing CD vs alpha – $\lambda = 30$ deg IGE.....	46
Figure 42. Middle wing CD vs alpha – $\lambda = 45$ deg IGE.....	46
Figure 43. Middle wing CD vs alpha – $\lambda = 60$ deg IGE.....	47

	Page
Figure 44. Middle wing CD vs alpha – $\lambda = 75$ deg IGE.....	47
Figure 45. Middle wing CD vs alpha – $\lambda = 90$ deg IGE.....	48
Figure 46. Middle wing C_m vs alpha – $\lambda = 0$ deg IGE.....	49
Figure 47. Middle wing C_m vs alpha – $\lambda = 15$ deg IGE.....	49
Figure 48. Middle wing C_m vs alpha – $\lambda = 30$ deg IGE.....	50
Figure 49. Middle wing C_m vs alpha – $\lambda = 45$ deg IGE.....	50
Figure 50. Middle wing C_m vs alpha – $\lambda = 60$ deg IGE.....	51
Figure 51. Middle wing C_m vs alpha – $\lambda = 75$ deg IGE.....	51
Figure 52. Middle wing C_m vs alpha – $\lambda = 90$ deg IGE.....	52
Figure 53. Front wing C_L vs alpha - 50 mph.....	53
Figure 54. Front wing C_L vs alpha - 60 mph.....	54
Figure 55. Front wing CD vs alpha - 50 mph.....	55
Figure 56. Front wing CD vs alpha - 60 mph.....	55
Figure 57. Front wing C_m vs alpha - 50 mph.....	57
Figure 58. Front wing C_m vs alpha - 60 mph.....	57
Figure 59. Front wing C_L vs alpha – $\lambda = 0$ deg IGE.....	66
Figure 60. Front wing C_L vs alpha – $\lambda = 15$ deg IGE.....	66
Figure 61. Front wing C_L vs alpha – $\lambda = 30$ deg IGE.....	67
Figure 62. Front wing C_L vs alpha – $\lambda = 45$ deg IGE.....	67
Figure 63. Front wing C_L vs alpha – $\lambda = 60$ deg IGE.....	68
Figure 64. Front wing C_L vs alpha – $\lambda = 75$ deg IGE.....	68
Figure 65. Front wing C_L vs alpha – $\lambda = 90$ deg IGE.....	69

	Page
Figure 66. Front wing C_D vs $\alpha - \lambda = 0$ deg IGE.....	69
Figure 67. Front wing C_D vs $\alpha - \lambda = 15$ deg IGE.....	70
Figure 68. Front wing C_D vs $\alpha - \lambda = 30$ deg IGE.....	70
Figure 69. Front wing C_D vs $\alpha - \lambda = 45$ deg IGE.....	71
Figure 70. Front wing C_D vs $\alpha - \lambda = 60$ deg IGE.....	71
Figure 71. Front wing C_D vs $\alpha - \lambda = 75$ deg IGE.....	72
Figure 72. Front wing C_m vs $\alpha - \lambda = 90$ deg IGE.....	72
Figure 73. Front wing C_m vs $\alpha - \lambda = 0$ deg IGE.....	73
Figure 74. Front wing C_m vs $\alpha - \lambda = 15$ deg IGE.....	73
Figure 75. Front wing C_m vs $\alpha - \lambda = 30$ deg IGE.....	74
Figure 76. Front wing C_m vs $\alpha - \lambda = 45$ deg IGE.....	74
Figure 77. Front wing C_m vs $\alpha - \lambda = 60$ deg IGE.....	75
Figure 78. Front wing C_m vs $\alpha - \lambda = 75$ deg IGE.....	75
Figure 79. Front wing C_m vs $\alpha - \lambda = 90$ deg IGE.....	76

List of Tables

Table	Page
Table 1. Justification for use of stationary ground plane.....	14
Table 2. Fan and Motor Specifications [24].....	15
Table 3. Maximum loads for 25lb balance.....	18
Table 4. Ground plane dimensions [5].....	22
Table 5. Experimental test matrix.....	26
Table 6. h/b for varying λ	27
Table 7. Missile model flight conditions.....	30
Table 8. Lambda UCAV flight conditions.....	30
Table 9. Measurement uncertainties.....	59

List of Symbols

Symbol	Name
a	Speed of sound
A	Axial force
α	Angle of attack
b	Wing span, varies with λ
c	Tunnel cross section
C_D	Drag coefficient
CG	Center of gravity
C_L	Lift coefficient
C_m	Pitch moment coefficient
D	Drag
ϕ	Induced drag factor
h	Height above ground plane, measured from ground plane to closest point on wing at $\alpha = 0$ deg
IGE	In ground effect
λ	Sweep angle
L	Lift
l	Roll moment, measured about CG
l^*	Length
m	Pitch moment, measured about CG
M	Mach number
N	Normal force
n	Yaw moment, measured about CG
OGE	Out of ground effect
ρ	Air density
q	Dynamic pressure, $\frac{1}{2} \rho V^2$
q_{corr}	Corrected dynamic pressure
P	Air pressure
R	Universal gas constant
Re	Reynolds number
S	Wing area
S^*	Side force
T	Temperature
V	Velocity
V_{corr}	Corrected velocity
Y	Yaw force
μ	Air viscosity
ψ	Yaw angle
γ	Ratio of specific heats
θ	Flight path angle
ϵ_{sb_b}	Solid body blockage correction
κ_3	Body shape factor
τ_1	Tunnel shape factor

EXPERIMENTAL INVESTIGATION OF OBLIQUE WING AERODYNAMICS AT LOW SPEED

I. Introduction

Section 1 - Oblique wings

Ever since Chuck Yeager broke the sound barrier in 1947, aircraft designers have been looking for wing designs that perform well at both subsonic and supersonic speeds. The general consensus is that the only way to accomplish this goal was through wing morphing of some kind providing variable wing geometry. The purpose of wing morphing is to provide a high aspect ratio for low-speed flight and for loitering and also a low aspect ratio for high speed flight.

The first generation of variable geometry wings was the swing wing designs. These designs utilized a pivoting wing that could swing back into a delta configuration at high speeds. Several swing wing airplanes were utilized by the United States Military in the 1960s and 1970s. The most notable and popular designs were the F-14, F-111, and B-1. These aircraft experienced some success, but the added mass and complexity of the swing wing mechanism made their more widespread use undesirable.

Another variable geometry concept currently garnering more research is the oblique wing design. The oblique wing “can vary the wing sweep with a single pivot that is primarily loaded in tension, trading aspect ratio for fineness ratio by sweeping one wing tip forward and the other wing tip back” [1]. Oblique wing aircraft have fewer moving parts than swing wing aircraft, thus making them lighter and less complex.

The first known oblique wing design was the Blohm and Voss P-202, designed in Germany by Richard Vogt in 1942. The P-202 can be seen in Fig. 1. The aircraft was a

single engine fighter that featured a top mounted wing designed to rotate in order to slow the onset of Mach divergence [1]. In 1952, R.T. Jones proved that for any flight Mach number the minimum drag for a given lift could be achieved by an oblique swept wing with an elliptic planform [2]. Other wind tunnel tests have shown that oblique wings are very effective at reducing wave drag at supersonic speeds [3]. More recently NASA test flew a full scale demonstrator, the AD-1. The AD-1 flew for 79 hours and performed well, although there were serious handling qualities issues at wing sweeps of greater than 45 deg [4]. Fig. 2 shows the AD-1.

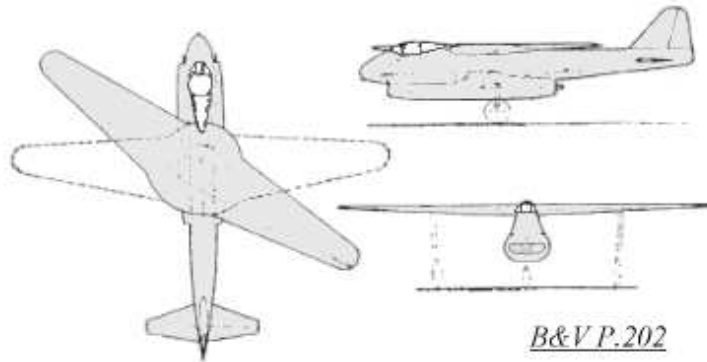


Figure 1. Blohm and Voss P-202 [1].



Figure 2. NASA AD-1 [4].

Section 2 - Ground effects

Ever since the advent of powered flight, pilots have experienced a “pillow effect” when flying close to the ground. This phenomenon is most felt during the most critical and dangerous phases of flight, takeoff and landing. Most aircraft experience a significant increase in lift and a decrease in induced drag. Pilots must manually account for this phenomenon because aircraft are not designed to deal with this condition [5].

An aircraft is normally considered to be in-ground effect (IGE) when it is flying within one wingspan, b , of the ground. When the aircraft is IGE the induced drag is usually reduced because of the interaction between the wingtip vortices and the ground [6]. While the aircraft is flying out-of-ground effect (OGE) the vortices are shed off the wing in a cylindrical pattern. During IGE flight the vortices begin to flatten out because the presence of the ground prevents them from forming cylindrically. This causes an increase in effective aspect ratio and wingspan. Since aspect ratio and induced drag are inversely proportional, an aircraft flying IGE will experience a lower induced drag and therefore a decreased total drag, assuming profile drag remains constant [6].

Along with the reduction in induced drag, aircraft flying IGE can be expected to have a higher lift and pitching moment. An important measure of aircraft aerodynamic efficiency is the lift to drag ratio, L/D . Since an aircraft IGE has a higher lift and lower drag it performs much more efficiently than an identical one flying OGE at the same flight conditions. This fact led Russian designer Rostislav Alexiev to develop what he called an ekranoplan. He designed the KM Caspian Sea Monster, a 550 ton vehicle for fast transportation and heavy cargo carrying over water. The Soviets designed several more ekranoplans before the program was cancelled due to lack of funding in the late

1980s [7]. Boeing is also currently examining the viability of a similar vehicle to the Russian's designs capable of carrying an entire Army Division or up to 17 M-1 tanks [8].

Section 3 - Research objectives and approach

The goals of this research were to determine the aerodynamic properties of a missile with an oblique wing installed and to see how the model performed in ground effect. The AFIT low speed wind tunnel was used, both without a ground plane for OGE tests and with the ground plane installed to determine IGE behavior. The IGE tests were run with the missile inverted above the ground plane, with the ground plane simulating an aircraft. The IGE tests were accomplished to determine any undesirable effects of an oblique winged weapon shortly after separation from an aircraft. The tests were performed at low speed for applicability to low speed guided bomb drops

II. Literature Review

Section 1: Oblique Wings

Oblique wings have been studied since World War II due to their promise of aerodynamic efficiency for aircraft flying at both transonic and supersonic speeds [1]. In 1958, R. T. Jones noted that wave drag and induced drag could be minimized by a variable sweep oblique wing with an elliptical lift distribution [2]. At low speed the most efficient wing has a high aspect ratio and is elliptically loaded due to the fact that induced drag is inversely proportional to aspect ratio. At supersonic speeds drag on an aircraft is dominated by wave drag. One major advantage of oblique wings for supersonic flight is that for equivalent span, sweep, and volume they distribute the lift over twice the length of a more conventional swept wing planform. Fig. 3 illustrates this point. This reduces lift dependent wave drag by a factor of four and volume dependent wave drag by a factor of 16 [1].

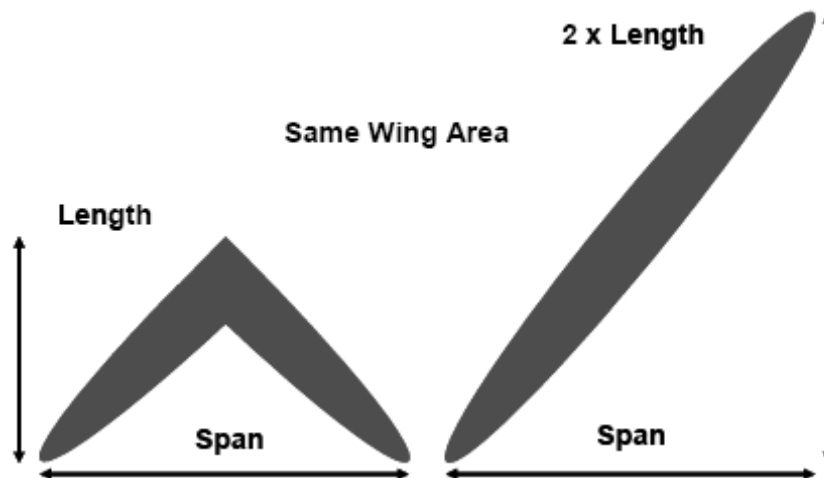


Figure 3. Illustration of 2X length for oblique wings [1].

Jones also showed that the induced drag of an oblique wing at optimal sweep is half of that for a delta wing of the same span [2]. Fig. 4 shows the induced drag of an oblique wing and delta wing.

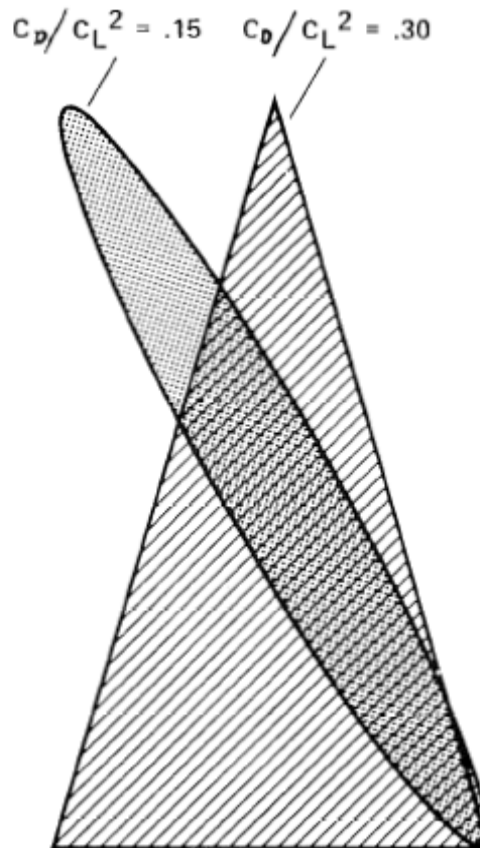


Figure 4. Comparison of induced drag for oblique and delta wing [9]

One of the main problems associated with the use of oblique wings is controllability. At low sweep angles, an oblique winged aircraft can be controlled much like a conventionally winged vehicle. In fact, using the NASA Langley tunnel, Campbell noted that at sweep angles of 40 deg or less there were no serious controllability issues encountered [10]. However, he also noted that at sweep angles above 60 deg ailerons become unsatisfactorily weak. He theorized that, “The aileron rolling effectiveness was not reduced by skewing the wing from 0 deg to 40 deg because the damping in roll

decreased approximately the same amount as the aileron rolling moments [10].” He also noted that at a sweep angle of 40 deg a large pitching moment was present, although this was not experienced during flight testing. This is because “the lift forces on the wing produced by rolling introduced pitch moments were equal to and opposite of the aileron pitching moments [10].”

Kempel et al. [11] performed flying qualities testing on the NASA F-8 oblique wing research aircraft. They noted that in general, as the sweep angle and dynamic pressure increased, pilot ratings decreased. They also noticed that in open loop configurations there was significant pitch-to-roll coupling and an unacceptable amount of pitch-to-sideforce coupling. At high dynamic pressures one pilot even described the lateral response to a pitch up command as “scary” [11]. This clearly means that sophisticated multi-input-multi-output control systems will need to be developed for oblique wing aircraft before they begin flying on a larger scale.

Section 2: Ground Effects

Ground effect is a phenomenon caused by the presence of a boundary near a wing altering the airflow around a wing. This altered airflow causes an increase in the lift and a decrease in the induced drag of a wing. The closer the wing is to the boundary, the more exaggerated this effect becomes. This is caused by the air flowing underneath the wing not being able to expand as it would in free air [12]. The difference in the airflow around a wing OGE and one flying IGE can be seen in Fig. 5. Halloran and O’Meara [12] describe the effect in terms of pressure:

“In terms of the total pressure of the flow, the additional lift is due to a rise in static pressure under the wing. The total pressure of the flow field can be divided between the static pressure (surface pressure) and dynamic pressure (the pressure associated with

velocity). As the total pressure remains constant throughout the flow field, the sum of the static and dynamic pressure must also remain constant. As the flow is forced into the region between the wing and the boundary, the decrease in dynamic pressure is transformed into a rise in the static pressure. This rise in the static pressure is often referred to as ‘ram pressure’. The resulting altered pressure distribution causes a net increase in the lift and a change to many of the other aerodynamic characteristics of the wing [12].”

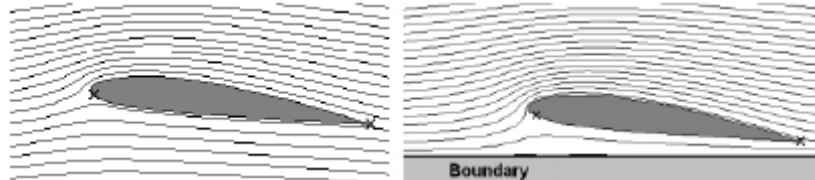


Figure 5. Airflow around wing OGE and wing IGE [12].

Also, there is not enough space for the vortices to fully develop when a wing is approaching the ground. Therefore the amount of leakage of pressure from the lower side to the upper side is less and the vortices become weaker. The vortices are also pushed outward by the ground, causing the effective aspect ratio to become higher than the geometric aspect ratio [12].

The “pillow effect” caused by the increase in lift an aircraft experiences when close to the ground has been experienced by pilots since the beginning of manned flight. In the early 1920s, a German engineer named Carl Wieselsberger used Prandl’s three-dimensional lifting line theory to develop an equation for the reduction in induced drag for an aircraft flying near the ground [13]. This equation has been used as the standard and has been verified by flight tests throughout the years [5]. The Wieselsberger equation relates the induced drag, C_{Di} , to the h/b of the wing. Fig. 6 shows a plot of Wieselsberger’s equation, with C_{Di} normalized to the value OGE.

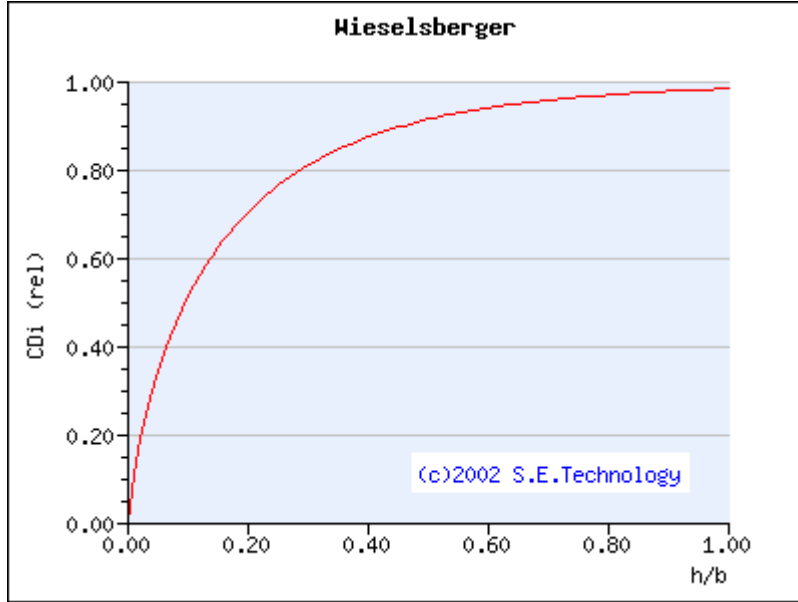


Figure 6. Graph of Wieselsberger's induced drag formula [7].

McCormick took a different approach when developing equations for lift and drag to determine ground roll of an aircraft. He used the lifting line theory and the Biot-Savart law to come up with an equation for the ratio of C_{Di} IGE to C_{Di} OGE. He modeled the wing as a horseshoe vortex with the ground simulated by having the vertical velocities canceling each other out. He used the height as the difference between the reflection plane and the vortices. Next, the Biot-Savart law estimated the velocities induced at a certain point from every horseshoe vortex. This allowed him to come up with the following relationship [14]:

$$\phi = \frac{C_{Di}(IGE)}{C_{Di}(OGE)} = \frac{16\left(\frac{h}{b}\right)^2}{1 + \left(\frac{h}{b}\right)^2} \quad (1)$$

Fig. 7 shows a plot of McCormick's induced drag factor. It can be seen that although McCormick and Wieselsberger took different approaches they both came up with very similar results.

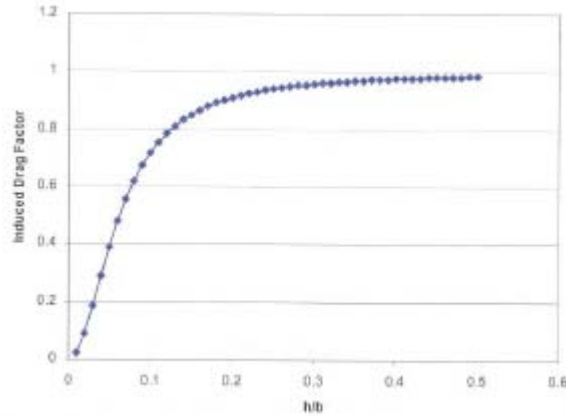


Figure 7. McCormick's induced drag factor [14]

Some of the first ground effects tests were accomplished by Raymond at the Massachusetts Institute of Technology in 1921 [15]. He installed a flat plate in the tunnel and tested three different airfoils at varying heights above the plate. He also attempted to use reflection to create an imaginary ground plane. Both sets of tests showed that near the ground a wing will experience an increase in lift and a decrease in induced drag [15].

Raymond's technique of using a fixed ground plane height and model has become known as static wind tunnel testing. Different ground heights were tested by moving the ground plane either closer or farther from the model. Pilots flew ground effect tests known as 'fly-by' patterns in an attempt to validate the tunnel results. Angle of attack and altitude were kept constant to find the location of the ground effect region [5]. This technique fails to capture the true dynamics of an aircraft as it approaches a runway because the aircraft has no sink rate. Schweikhard developed a method in 1967 to measure the ground effect of an aircraft in flight [16]. Test pilots would fly the aircraft at a set angle of attack and throttle setting, but would allow the sink rate to vary. This technique ensured that lift, drag, and pitch moment were constant as the ground approached. Engineers then measured any change in flight path angle, velocity, or

control surface deflection as the aircraft entered the ground effect region. The engineers discovered this technique saved time and required less data analysis than previous techniques [16].

Since wind tunnel testing saves a lot of time and money over flight testing, engineers developed new ways to dynamically test ground effects in the wind tunnel. A dynamic wind tunnel test moves the model mechanically or manually towards the ground plane to better simulate take off or landing approach [5]. Chang et al. noted the need for dynamic testing because of the disparity between static tests and flight test data [17]. He tested several wings and aircraft models both statically and dynamically in the wind tunnel. He and Baker et al. noted that at $h/b < 0.4$, the static wind tunnel results over estimated the change in lift due to ground effect [18].

Most of the time an aircraft flying in the ground effect region will experience an increase in lift and a decrease in drag, but this is not always the case. Lee et al. [19] experienced an increase in lift and drag as height above the ground plane decreased during their tests of a 60 deg delta wing, F106, and XB-70-1 models. They tested h/b from 0.2 to 1.6 and Reynolds numbers from 3×10^5 to 7.5×10^5 for all three models. Jones [5] extrapolated the data from the C_D vs h/b and C_L vs h/b to analyze trends in L/D . He noted the 60 deg delta wing experienced a small decrease in L/D and that the F-106 and XB-70-1 both had a decrease and a small increase in L/D depending on h/b . The XB-70-1 experienced a downward trend in C_D between h/b and 0.3 and 0.2, which explains the increase in L/D [5].

Curry [20] also tested the F-16XL for ground effects using both a wind tunnel and flight testing. He noted that C_D increased as h/b decreased. He stated that for an aircraft

flying close to the ground, an increase or decrease in drag is possible. An increase in drag was also noted on the Tu-144 supersonic transporter when flying close to the ground by Curry and Owens [21].

One main concern when using a ground plane in a wind tunnel is the boundary layer build-up on the top surface of the ground plane. Any surface that has direct contact with a moving fluid will experience a boundary layer forming. This boundary layer can cause inaccurate data when a ground plane is installed. The solution to this problem is a boundary layer removal system [5].

The most common way to remove a boundary layer is through the use of a moving belt system. The belt moves in the tunnel at the same speed as the airflow thus better simulating an aircraft flying over a stationary ground. However, several studies have shown that a moving belt is not required to get accurate results at all flight conditions. It has been shown that the need for a moving belt is dependent on the maximum C_L of the aircraft. Turner [22] determined the conditions under which an endless belt system would be needed for accurate results. He showed that the necessity of a moving belt depended on the spanwise lift coefficient and height above the ground [22]. Fig. 8 shows the criteria Turner established for when an endless belt ground plane was needed.

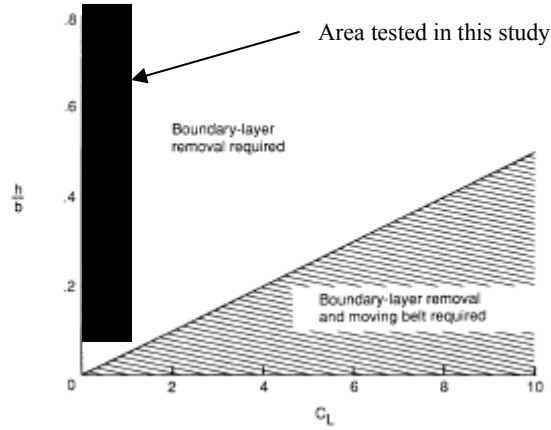


Figure 8. Conditions needing an endless belt ground plane [22]

The shaded region represents the tunnel conditions tested in the current study. Therefore, based on Turner's study [22], a moving belt was not required for this study, and one was not used.

Kemmerly and Paulson [23] did another study on the necessity of the use of a moving plane. They found that if equation 2 was met, then the use of a moving ground plane is needed.

$$\frac{h/b}{C_L} < 0.05 \quad (2)$$

Table 1 shows the values used in this study. It can be seen that none of the configurations gives a value of less than 0.05, so once again it is confirmed that a moving ground plane is not needed for boundary layer removal. You can also see that if equation (2) was plotted similarly to Fig. 8, it would give almost equal results.

Table 1. Justification for use of stationary ground plane

Sweep angle, λ (deg)	C_L max	h/b min	(h/b)/ $C_{L \text{ max}}$	< 0.05
0	0.78	0.071	0.09	No
15	0.3	0.074	0.25	No
30	0.45	0.082	0.18	No
45	0.7	0.101	0.14	No
60	0.55	0.143	0.26	No
75	0.3	0.276	0.92	No
90	0.22	0.625	2.84	No

III. EXPERIMENTAL SETUP

Section 1 - Wind Tunnel

The AFIT 3' X 3' wind tunnel was used for this experiment. The tunnel was manufactured by New York Blower Company. The wind tunnel is powered by an ACF/PLR class IV fan with a Toshiba Premium Efficiency (EQP III) fan motor. Both the fan and the motor are controlled by a Siemens (13710) Adjustable Frequency Tunnel Controller. The tunnel has an operating speed of 1785 rpm and has a maximum speed of 150 mph. Table 2 shows the fan and motor specifications:

Table 2. Fan and Motor Specifications [24].

Motor	Controller
3 phase induction	
1785 RPM operating speed	
Maximum theoretical speed – 150 mph	
Maximum tested speed – 148 mph	
200 brake horsepower	250 maximum horsepower
230/460 volts	460 volts
444/222 amps	315 amps
60 Hz	
4 poles	

The tunnel is an Eiffel-type with an open circuit configuration and a closed test section 44" X 31" in size. The fan is at the end of the tunnel and pulls in ambient air through a 122" W X 111" H X 70" L intake plenum. The plenum consists of four steel

mesh anti-turbulence screens with $\frac{1}{4}$ " aluminum honeycomb flow straighteners with a minimum aspect ratio of 15 to give the tunnel good, laminar streamlines [25]. The flow travels to the test section through a 95.5" long converging section with a contraction ratio of 9.5:1. The height of the tunnel is 111" through the anti-turbulence screens and contracts to the test section height of 31". Fig. 9 shows the dimensions of the converging section of the tunnel and Fig. 10 displays a schematic of the tunnel.

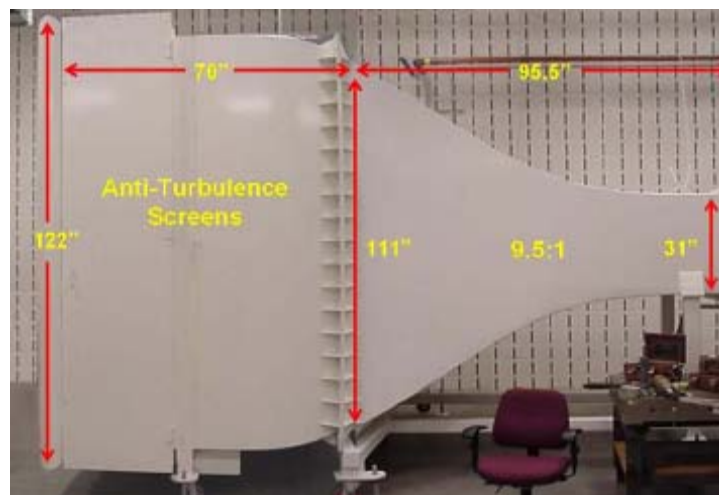


Figure 9. Wind tunnel converging section dimensions.

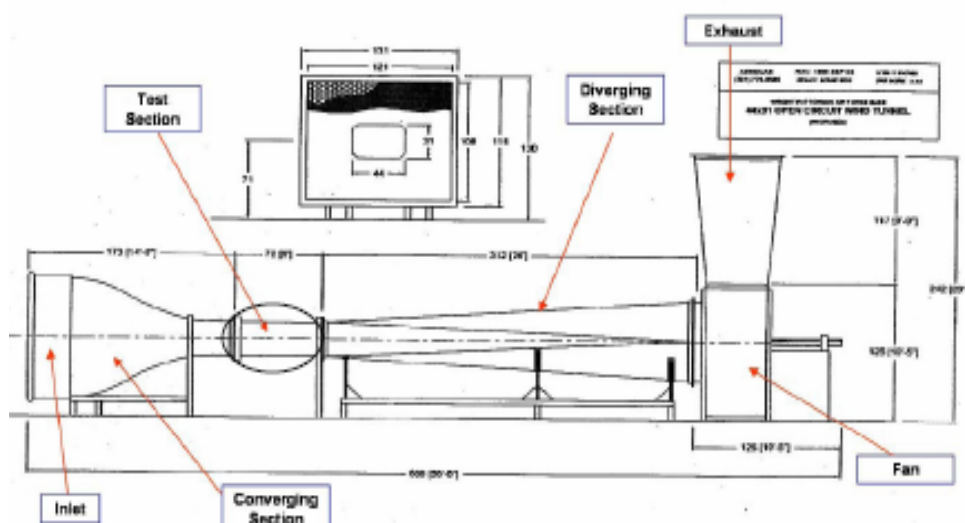


Figure 10. AFIT wind tunnel schematic.

The test section has an octagonal shape to reduce corner interference [24]. It has dimensions of 31”H X 44”W X 72”L. The test section is shown in Fig. 11. The test section sting mechanism is remotely controlled and can vary angles of attack from -25 to 25 degrees.

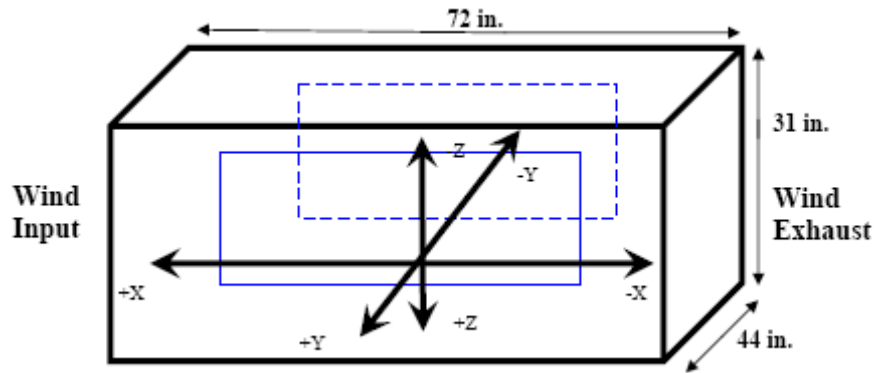


Figure 11. Wind tunnel test section.

The tunnel diverges after the test section and the air exits through a vertical exhaust plume. There is a fence at the end of the tunnel to prevent any debris from impacting the fan or motor.

Section 2 - Balance

The balance used for this experiment was AFIT's eight component 25-lb balance manufactured by the Able Corporation (0.5 MK VI). It is an internal balance and uses strain gauge rosettes to measure loads in the various directions. The maximum loads of this balance in the each specific direction are shown in Table 3.

Table 3. Maximum loads for 25lb balance.

Component	Maximum
Normal Force (N1)	25 lbs
Pitch Moment (N2)	25 in-lbs
Side Force (S1)	15 lbs
Yaw Moment (S2)	15 in-lbs
Axial Force (A1)	30 lbs
Roll Moment (L1)	15 in-lbs

The balance measures forces in terms of changes in voltage. LabView, which is used to write data acquisition and calibration programs, collects the data and converts the voltages to pounds force for use in calculating, lift, drag, moments, and other parameters.

Section 3 - Missile Model and Wing

An aluminum missile model 28.44 in long with a projected diameter of 2 in was used in this experiment. The missile has four identical tailfins, two horizontal and two vertical, made from a symmetric airfoil. The bare missile weighs 7.33 lbf. The missile is shown in Fig. 12.



Figure 12. Missile model mounted in tunnel.

The wing section used for the wing is shown in Fig. 13. It has a chord of 2 in, a span at $\lambda=0$ of 17.5 in, has no twist or dihedral, but does have a positive camber. This airfoil was chosen in order to be able to compare the results of this experiment to previous data using this missile model. Corneille [26] tested a joined wing configuration to determine if it was beneficial over a missile with a single wing. Dike [25] then tested the joined wing as it morphed out to full extension. In both cases the missile model was the same one used in this study and the joined wings tested had the same basic airfoil shape. For this experiment the chord was doubled in order to add more stiffness and strength to support the loading of the entire span.

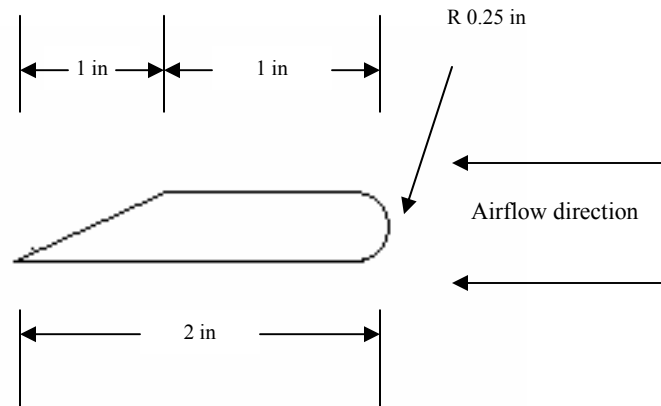


Figure 13. Airfoil profile.

In this study, the sweep angle λ is measured with the wing perpendicular to the missile being 0 deg and the wing parallel to the missile being 90 deg. The convention used to define the sweep angle is shown in Fig. 14.

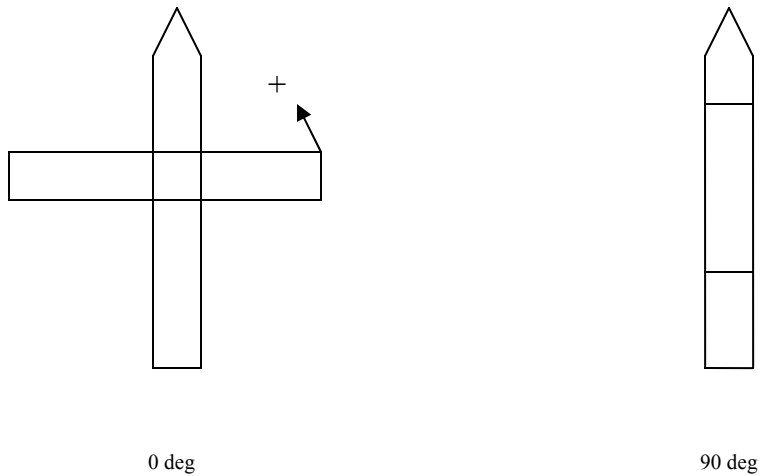


Figure 14. Sweep angle convention used

The wing was first drawn in SolidWorks[®] and then sent to AFIT's 3-D rapid prototyping machine. The Stratasys EDEN 333 rapid prototyping machine lays down 0.0006 in layers of UV plastic (also called photopolymer plastic) and a gel-like UV plastic for support materials using eight small jets. The eight jets traverse the printed region in 2 in strips and then a UV light cures the plastics simultaneously [27]. The Full Cure 700 series photopolymer plastic model material can be machined, drilled, and painted [28]. The SolidWorks drawing of the wing can be seen in Fig. 15.

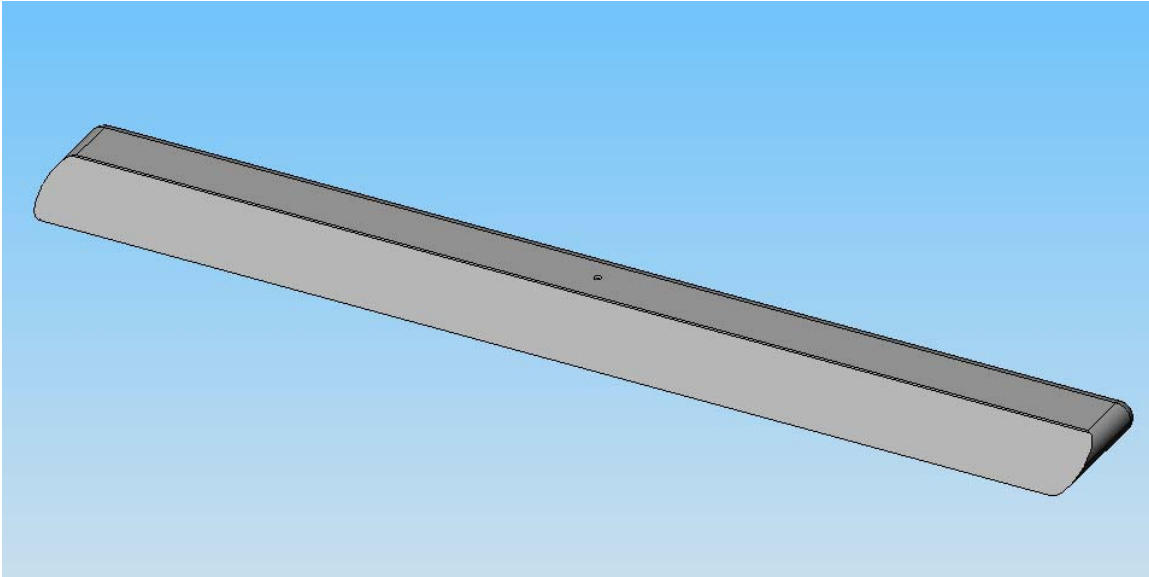


Figure 15. SolidWorks drawing of wing.

The wing was installed on the missile at two different locations. The tests were run with the leading edge of the wing installed 4 in from the nose of the missile, referred to as front wing in this study, and were also run with the wing at 8 ½ in from the nose, referred to as middle wing, to try and determine if the wing was getting airflow disturbed by the nose of the missile.

Section 4 - Ground Plane

A ground plane was installed in the tunnel to simulate the missile model separating from the aircraft. The ground plane was made of two steel plates and eight cylindrical steel legs. The dimensions are shown in Table 4, and a picture of the ground plane is shown in Fig. 16.



Figure 16. Ground plane [5].

Table 4. Ground plane dimensions [5].

Plate	
Thickness, in	0.25
Diameter/width, in	35.31
Max length, in	44.31
Legs	
Diameter	1.5
Length, in	
Height 1	9.77
Height 2	12.17
Height 3	12.97
Height 4	13.77

The circular plate is the same size as the bottom plate of the test section, which is rotated to simulate yaw angles. Mounting the circular plate in this manner allows models being tested with the ground plane to be run at the same yaw angles as those tested without the ground plane. There is also a slit in the circular plate to reduce interference caused by the sting mechanism rotating to simulate angle of attack. The front piece is rounded and beveled and provides a straight leading [5]. Fig. 17 shows the two ground plane plates separated and Fig. 18 shows the ground plane leading edge.

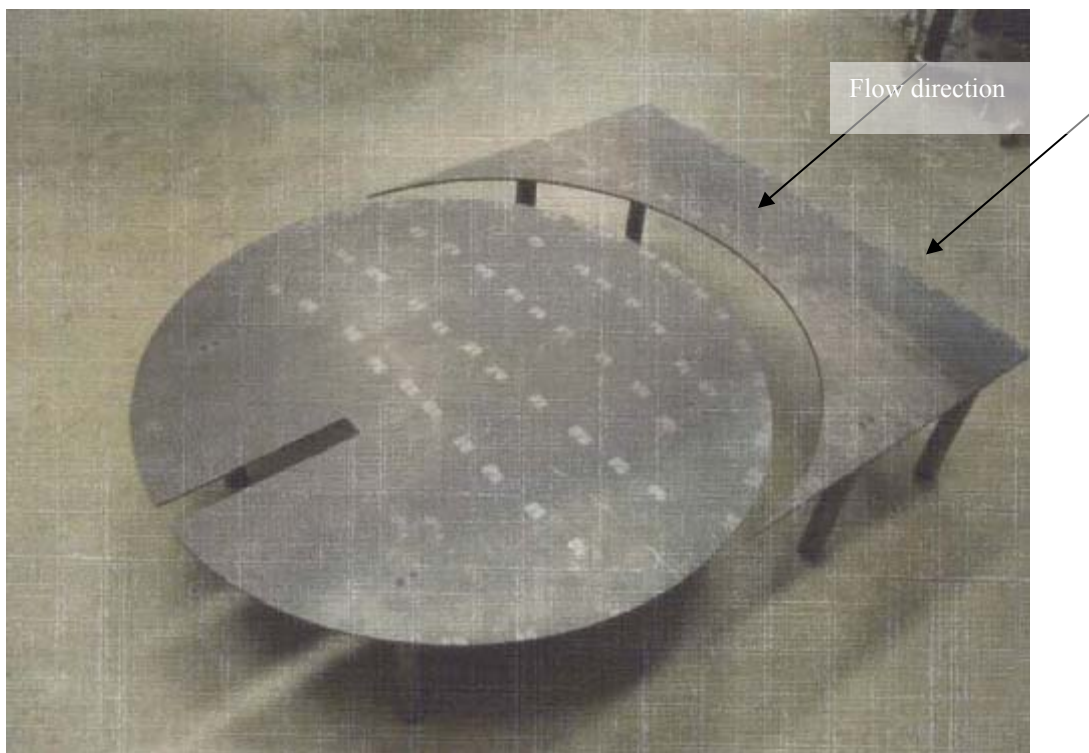


Figure 17. Top view of ground plane with pieces separated [5].

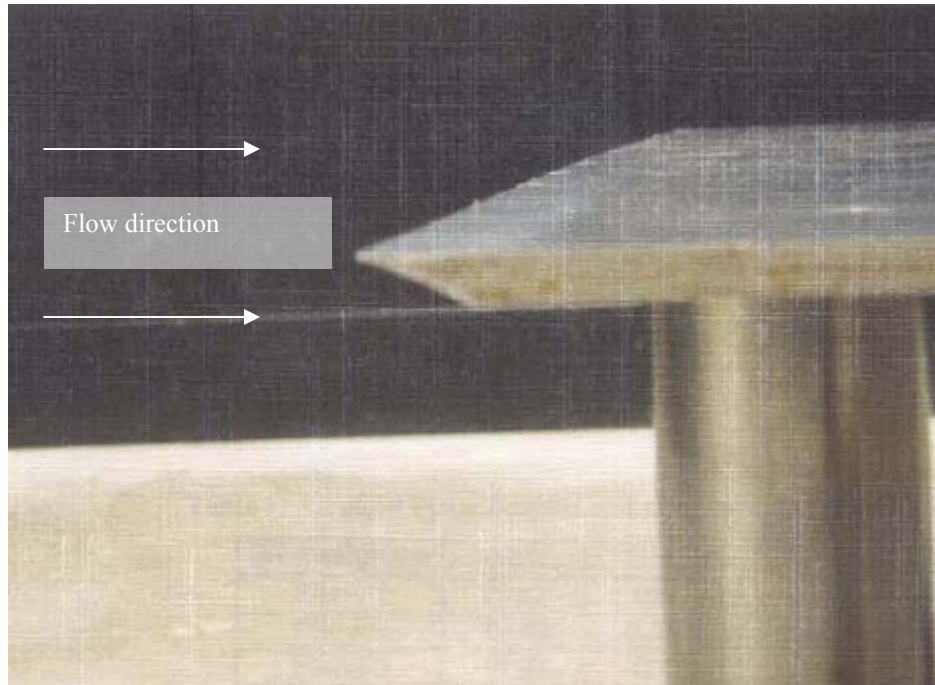


Figure 18. Ground plane leading edge [5].

Section 5 - Experimental Procedure

The first step in taking data was to perform a balance calibration using static weights. Known loads were applied in the different directions to the balance and the calibration constants were calculated by the software by matching the loads on the balance to the loads recorded in the software. It was ensured that the registered voltages corresponded linearly to the increases of the applied weights so that linearity could be verified. LabView Virtual Instrument[®] was used to control all tunnel parameters. These parameters include angle of attack, yaw angle, and tunnel velocity. In order to provide analog backups for the angle of attack and sideslip angle, there are also optical encoders mounted on the sting. For the velocity, a pressure transducer and pitot-static tube were used as the analog measurement. These measurements were used as the main guide for tunnel velocities throughout all of the testing [5].

The balance data were stored as two normal force components (N_1 and N_2), two side force components (S_1 and S_2), an axial force component (A_1), and roll moment (ℓ_1). The strain gage rosette experienced a continuous flow of voltage, with the resistance being constantly measured. Any increase in the length of the wire was caused by an increase in the resistance. The output voltages caused by the increased resistance were equated to strain and ultimately force through a series of calibration equations. A conventional coordinate system was used with the positive x-direction pointing towards the intake, the positive y-direction pointing right when looking in the positive x-direction, and the positive z-direction pointing down [5]. Fig. 19 is an illustration of the coordinate system used.

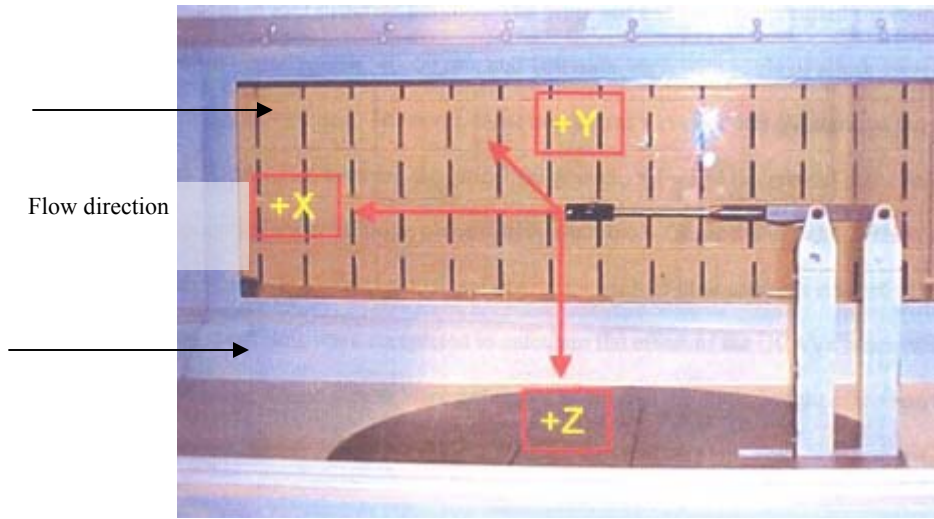


Figure 19. Tunnel coordinate system [29].

The missile and wing were tested in two different flight conditions. The first was with the wing mounted on top of the missile to measure forces out-of-ground-effect (OGE). The proposed test conditions include runs at speeds of 100, 130, and 145 mph. At each speed the sweep angle, λ , was varied from 0 to 90 deg, in 15 deg increments while angle of attack, α , was varied from -4 to 15 degrees in 2 deg increments until the

final 1 deg increment from 14 deg to 15 deg. On the first run, with $\lambda = 0$ deg and speed of 100 mph, the model began to oscillate violently up and down at $\alpha = 4$ deg so the run was aborted. The decision was then made to run the tests at 50 and 60 mph, with all other parameters as proposed. A tare run was also completed to determine the effects of the missile's and wing's static weight on the balance.

Once the OGE tests were complete, the missile was rotated 180 degrees and the wing mounted inverted underneath the missile and above the ground plane. This was done to simulate launch from an aircraft, and to determine the forces caused by in-ground-effects (IGE). The original plan was to run the tests with all four ground plane heights. After running the tests at the first two heights it was determined that testing at the other two ground plane heights would not be possible due to inadequate clearance. With the first ground plane, α was varied from -4 to 15 deg to match the testing without the ground plane. With the second plane α could only be varied from -2 to 5 deg due to limited clearance and the possibility of interference between the model and the ground plane. Table 5 shows the experimental test matrix.

Table 5. Experimental test matrix.

Tunnel Speed (mph)	OGE (deg)	IGE Plane 1 (deg)	IGE Plane 2 (deg)
50	$-4 < \alpha < 15$	$-4 < \alpha < 15$	$-2 < \alpha < 5$
60	$-4 < \alpha < 15$	$-4 < \alpha < 15$	$-2 < \alpha < 5$

A very important parameter when calculating IGE forces and moments is h/b , with h being the height above the ground plane measured from the plane to the nearest point on the missile at 0 deg angle of attack, and b being the wing span. When dealing

with oblique wings h/b is not constant, because as λ varies so does b . As the wing is swept to higher sweep angles, the wing span decreases to a minimum of 2-in, the chord, when the wing is at a 90 deg sweep angle. Table 6 shows the relationships between λ and h/b .

Table 6. h/b for varying λ .

λ (deg)	b (in)	h/b	
		Plane 1	Plane 2
0	17.5	0.221	0.071
15	16.9	0.229	0.074
30	15.16	0.248	0.082
45	12.37	0.313	0.101
60	8.75	0.443	0.143
75	4.53	0.855	0.276
90	2	1.94	0.625

During the OGE testing the normal convention for coordinate systems was used. Lift was in the negative Z-direction, drag in the negative X-direction, and a positive pitching moment, measured about the center of gravity, causing the nose of the missile to move in the negative Z-direction. A positive angle of attack also causes the nose to move in the negative Z-direction. Fig. 20 shows this configuration.

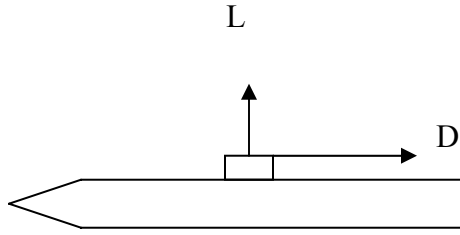


Figure 20. Force directions for OGE testing at $\lambda = 0$.

When the model was tested with the ground plane, lift and pitching moment now acted in the opposite direction. Now the lift the wing created acted in the positive Z-direction. Also, since lift and positive angle of attack should act in the same direction, angle of attack now caused the nose to move in the positive Z-direction. The drag acts in the same direction for both configurations. Fig. 21 shows the direction in which the IGE forces acted.

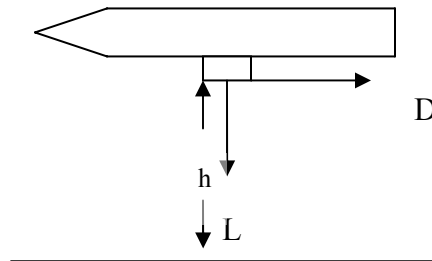


Figure 21. Force directions for IGE testing at $\lambda = 0$.

To account for the directions the forces acted in, some of the data had to be altered before they could be analyzed. For the analysis, the lift, angle of attack, and pitch moment that was registered by the balance was multiplied by negative one. This ensured that all of the forces and moments measured in the OGE and IGE tests were acting in the same direction so they could be compared.

Section 6 – Data Analysis

A data acquisition program was set up within the control computer to store the data in a tab delimited text file at a sampling rate of 2 Hz. First, the flow velocity was increased from zero up to the desired velocity. After ensuring the balance was accurately taking data, the model was dropped to its lowest α value and data was acquired for ten seconds. The angle of attack was then increased by 2 deg and held for an additional ten seconds. This was repeated until an angle of attack of 14 deg was reached, at which time it was increased by one degree to 15 degrees. For the tests with the second ground plane α was increased in one degree increments until five degrees was met.

A MATLAB[®] code written by Deluca [24] and Gebbie [30] and altered by Jones [5] and In [29] was used to reduce the acquired force and moment data. The reduction program first loads the appropriate tare and experiment text files. It then combines the readings for each α and averages them into a single test point for each α . Before the data were exported as aerodynamic coefficients, the testing conditions, balance interactions, and blockage corrections were calculated [5].

After the MATLAB[®] code reduced the data, an output file was created in EXCEL[®] format that consisted of Mach number, Reynolds number, dynamic pressure, velocity, angle of attack, lift, drag, roll moment, pitch moment, yaw moment, and side force for every angle of attack tested [5]. See Appendix A for a sample calculation of the data reduction.

IV. RESULTS & ANALYSIS

Verification of balance and data reduction program

Several tests were run to verify that the balance was properly calibrated and recording accurate raw data and to ensure the MATLAB[®] program was correctly reducing the raw data. The missile model was run without the wing installed at identical conditions to the ones run by Corneille [26] and Dike [25]. The lambda UCAV model was also tested at the same conditions run by In [29]. Tables 7 and 8 show a summary of flight conditions tested using these two models.

Table 7. Missile model flight conditions.

Speed (mph)	Mach no.	q (lbf/ft ²)
60	0.082	9.77
100	0.136	26.50

Table 8. Lambda UCAV flight conditions.

Speed (mph)	Mach no.	q (lbf/ft ²)	Re
60	0.082	9.72	3.5e5
80	0.109	17.13	4.6e5

The values for the lift coefficient, C_L , as a function of angle of attack, α , for the bare missile are shown in Figs. 22 and 23. The results agree somewhat in the 60 mph case and much better in the 100 mph case. The main problem is that even at its maximum the missile is only producing around 0.2 lbf of force, depending on α . This is

too small a number to expect accurate numbers from this 25-lb balance, which was also used by Dike. One possible explanation is differences in how the model was installed. All three of these runs were accomplished with the model removed in between. Different tare runs were accomplished for each run, with the tare possibly having small discrepancies. Finally, the calibrations done for this study and the Dike [25] study were slightly different. All of these errors more than likely combined to give the differences shown in the curves. The missile with the wing installed produced significantly more lift than the bare missile. These tests also prove some measure of repeatability because run one was accomplished as the first test done, and run two was accomplished after all other runs were complete.

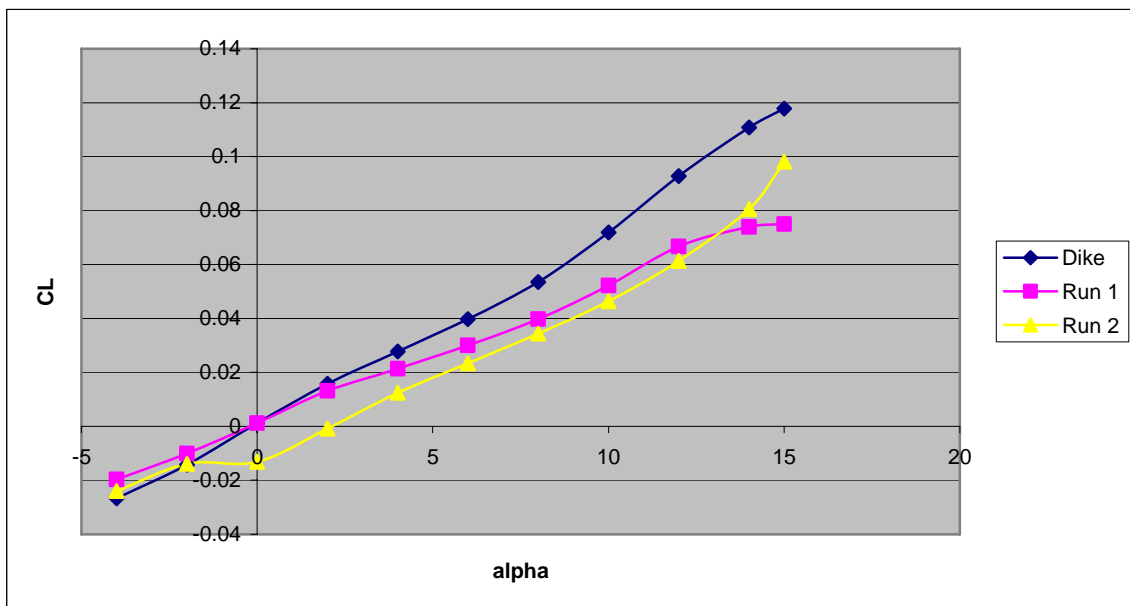


Figure 22. Bare missile C_L vs alpha - 60 mph.

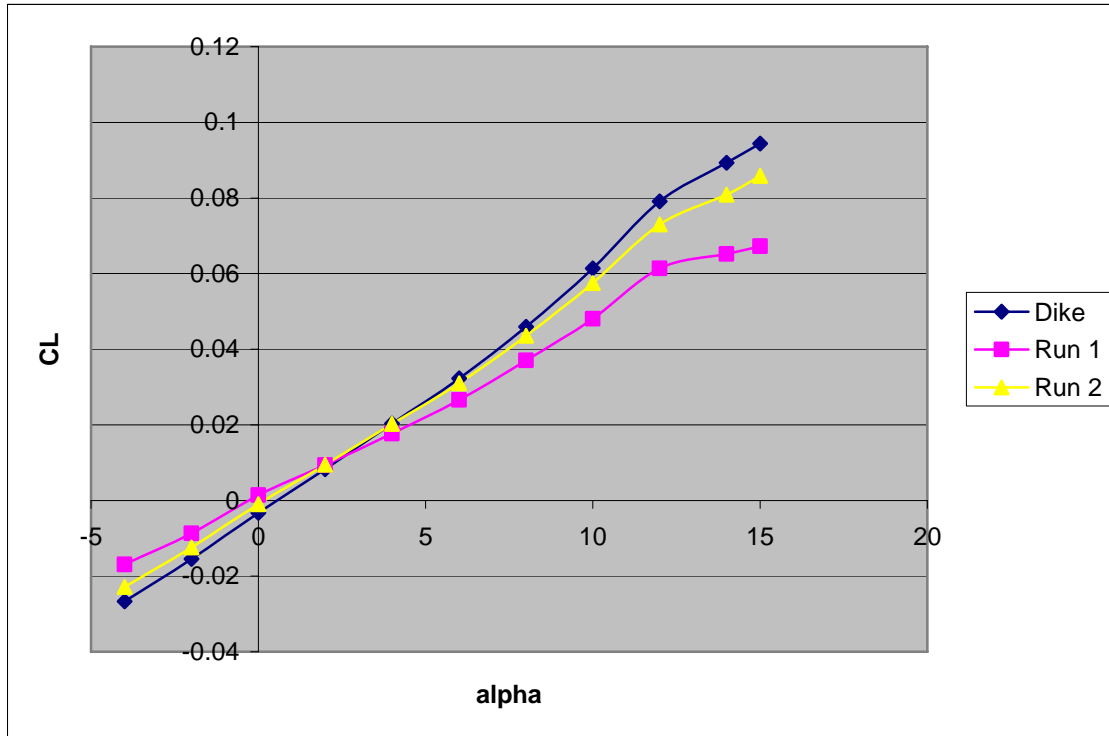


Figure 23. Bare missile C_L vs α - 100 mph.

In order to try and get a better measure the accuracy of the balance and data reduction, the lambda UCAV model was tested at identical conditions to the ones used by In [29]. The results can be seen in Figs. 24 and 25.

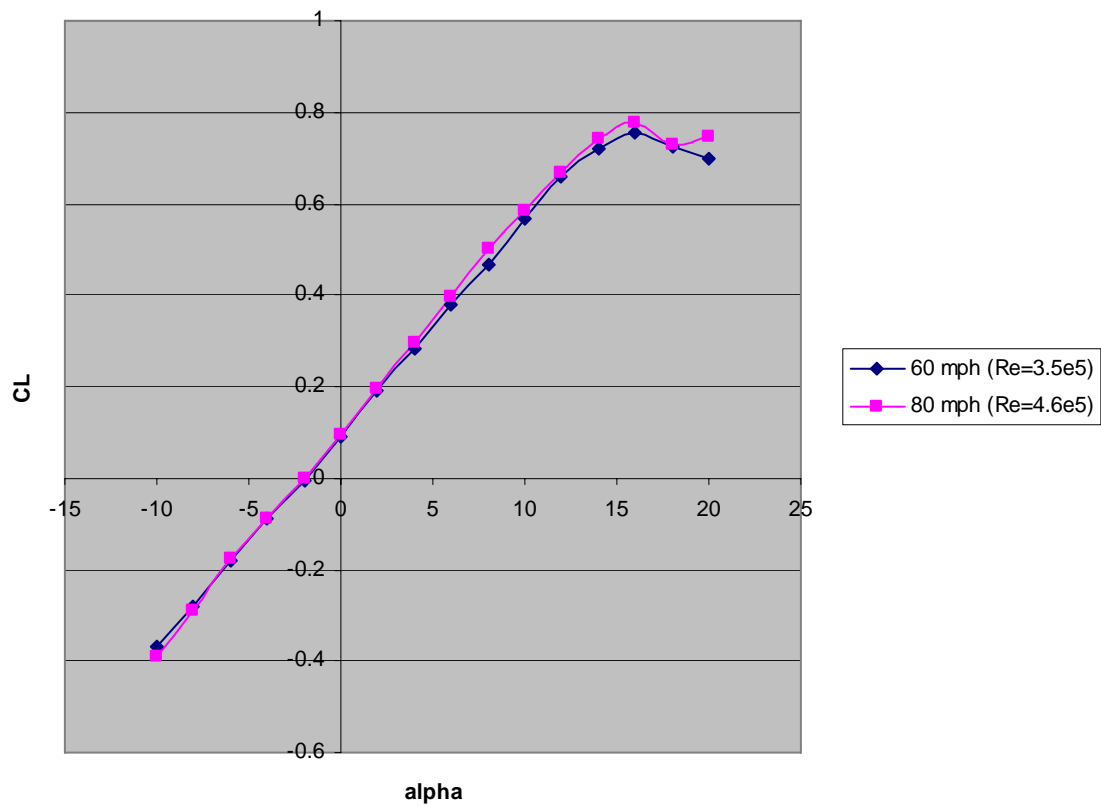


Figure 24. My lambda UCAV results.

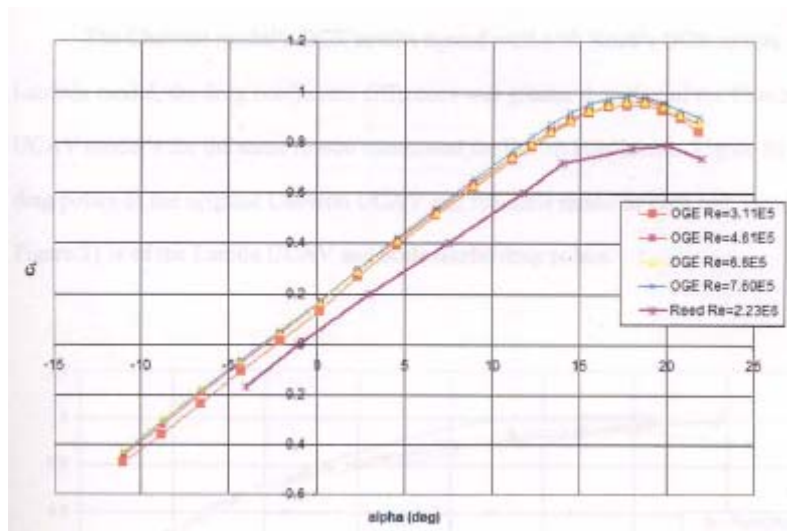


Figure 25. In's lambda UCAV results [In].

My results match up very well to the Reed results shown by In [29]. They differ somewhat in the values of the other runs, but the shape is almost identical. The differences are probably due to the fact that In used a 100-lbf balance, where a 25-lbf balance was used in this experiment, giving slightly different values.

Middle Wing

The lift coefficient is plotted versus angle of attack in Figs. 26 and 27. In these figures the sweep angle, λ , was varied from 0 to 90 deg in 15 deg increments. For all cases S, the reference area used to calculate C_L was the planform area, and was kept constant regardless of the sweep angle. At both speeds the wing stalled at $\lambda = 0$ and 15 deg at around α of 4 deg, but then recovered causing C_L to once again begin to rise. This can be seen in the large drop off of C_L . The wing stalling could have also been what caused the model to oscillate up and down in the original 100 mph run at $\alpha = 4$ deg. In this configuration the $\lambda = 45$ deg configuration still performs well, delaying stall until around 14 deg. C_L maximum occurs at $\lambda = 0$ deg.

The value of C_L at stall at $\lambda = 0$ was slightly higher for the 50 mph case than for the 60 mph case. The maximum values for C_L at $\lambda = 0$ are virtually identical for 50 and 60 mph.

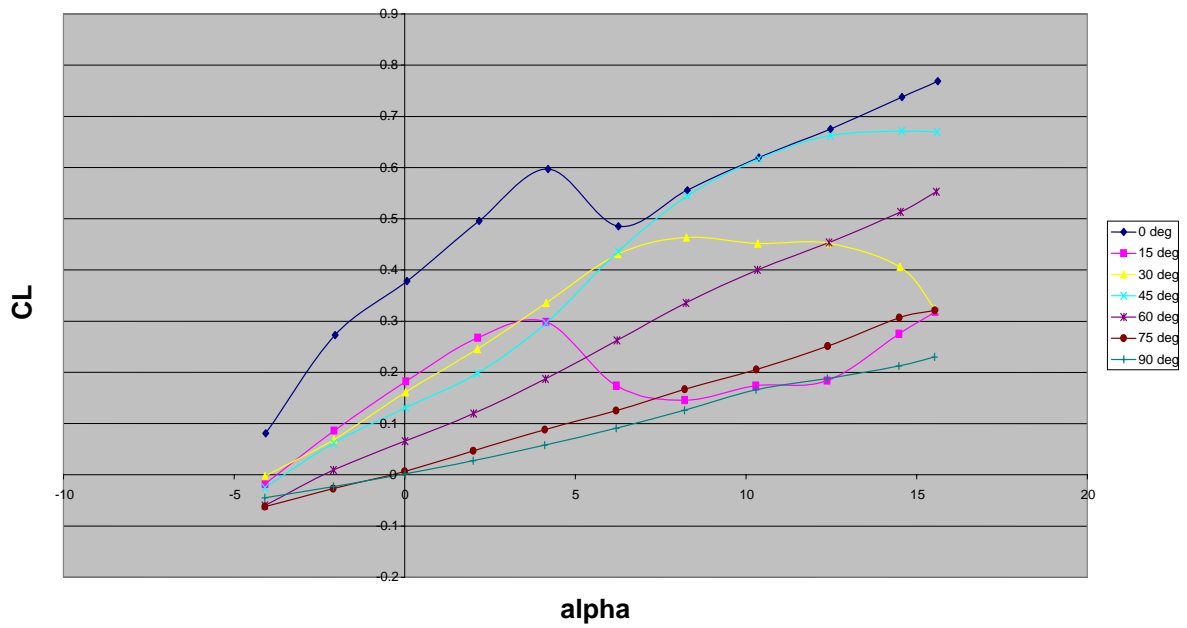


Figure 26. Middle wing C_L vs α - 50 mph.

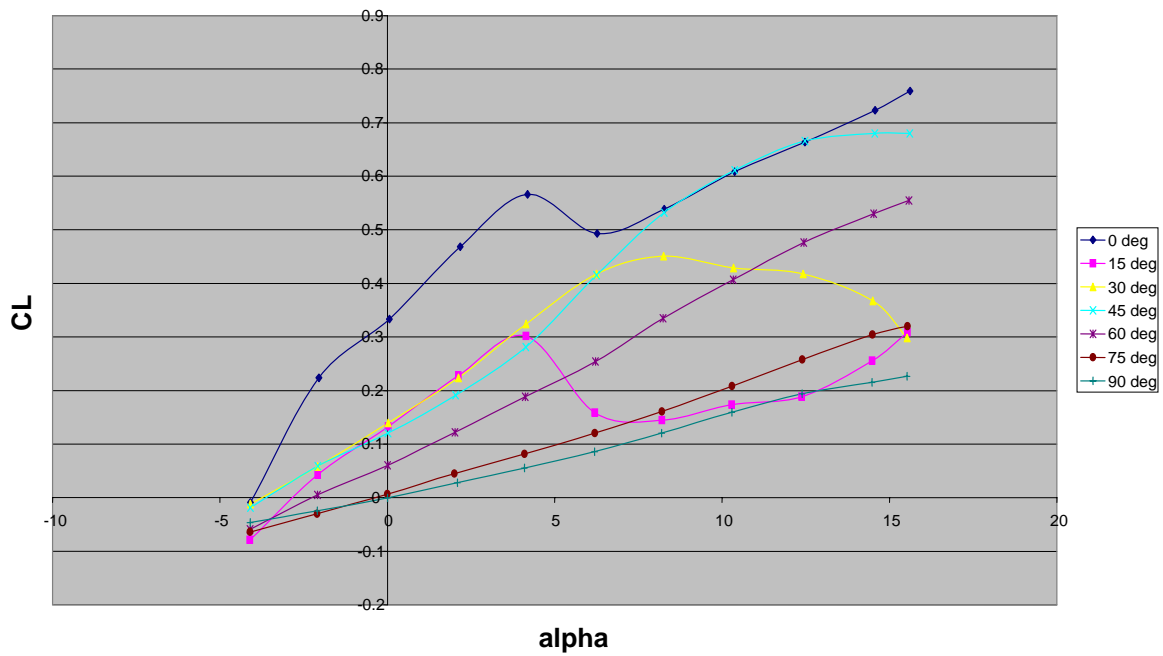


Figure 27. Middle wing C_L vs α - 60 mph.

C_D is plotted versus α in Figs. 28 and 29 for the middle wing configuration. These plots look like typical C_D versus α plots. The drag reaches a minimum value but never goes negative and then steadily increases as the angle of attack increases. Also, at high angles of attack the drag increases as λ decreases. This agrees with Tang et al. [34] who showed that for an oblique wing projectile traveling at $M = 0.8$, the drag is inversely proportional to sweep angle. One possible explanation could be that the decrease in friction drag caused by less frontal area being presented to the air stream as the sweep angle increases is larger than the increase in pressure drag caused by the fact that the wing is becoming less streamlined as it is swept, although no pressure measurements were taken in this study to verify this. One puzzling result is at both speeds both $\lambda = 15$ and 30 deg have a higher C_D than $\lambda = 0$ deg at $\alpha = 0$ deg.

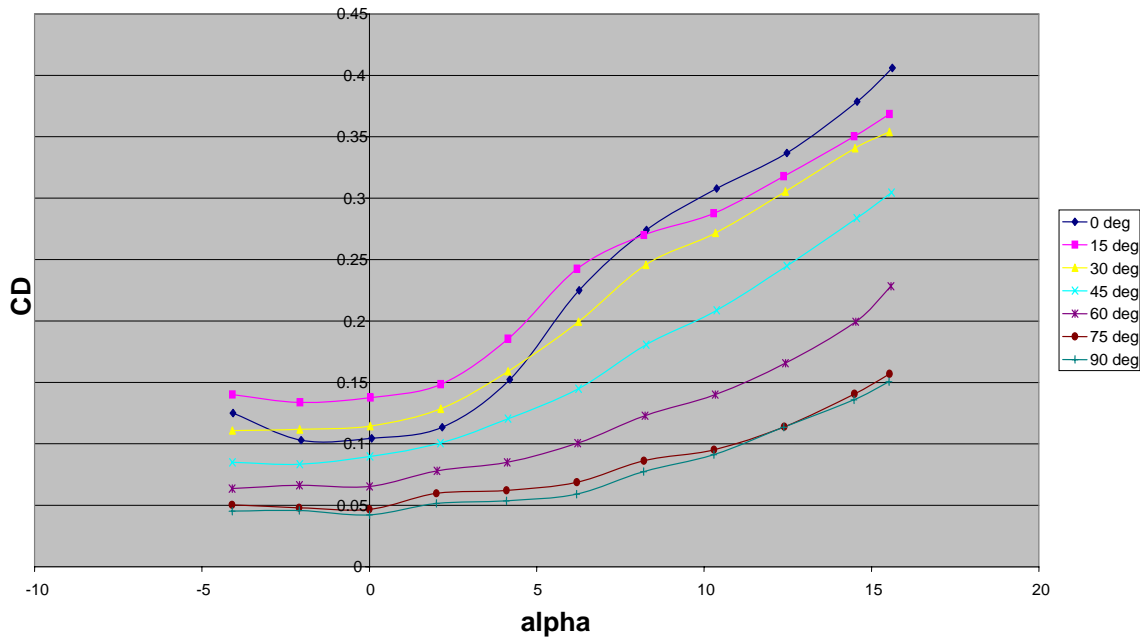


Figure 28. Middle wing C_D vs alpha - 50 mph.

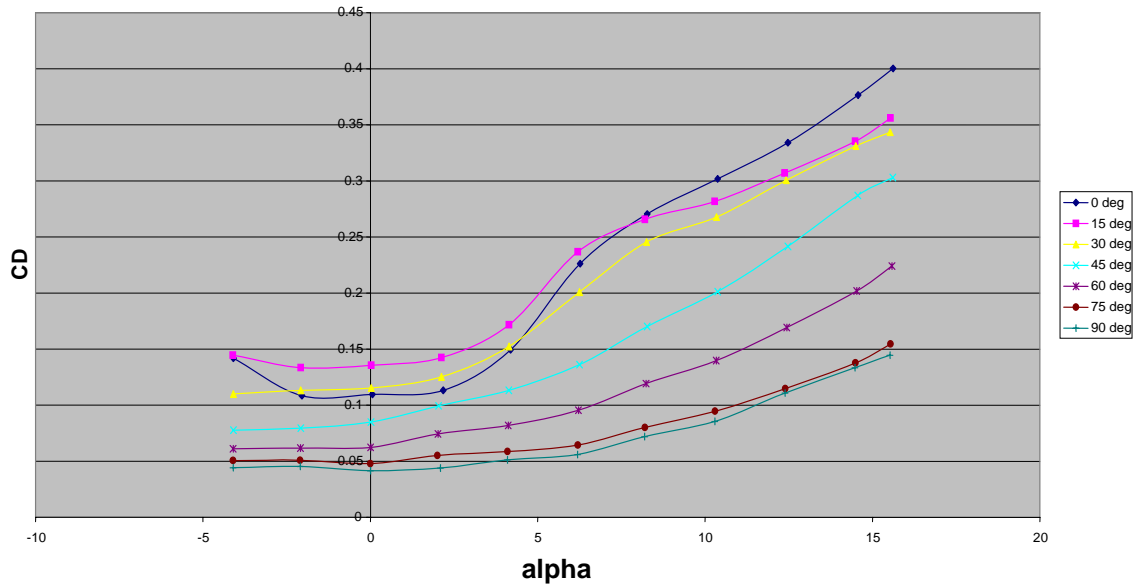


Figure 29. Middle wing C_D vs α - 60 mph.

Lastly, C_m is plotted as a function of α for the middle wing configuration, measured about the center of gravity. This can be seen below in Figs. 30 and 31. According to Nelson [31], in order for an aircraft to have longitudinal stability, the slope of the C_m versus α curve should be negative. This is so that if the aircraft encounters an upward gust it would tend to want to respond nose down therefore returning itself back toward equilibrium [31]. With the exception of high angles of attack all of the slopes are negative or near zero. At both speeds at $\lambda = 0$ the slope is very negative indicating very good pitch stability. Most of the other configurations are only slightly negative or near zero so the tail could still have to be enlarged or moved farther back.

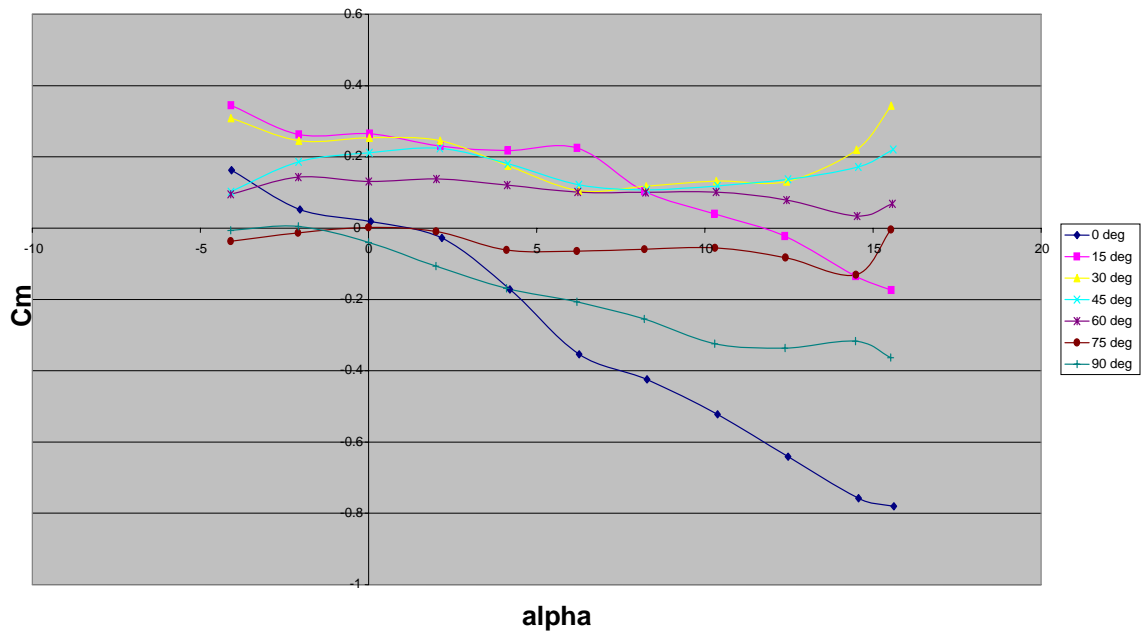


Figure 30. Middle wing C_m vs alpha - 50 mph.

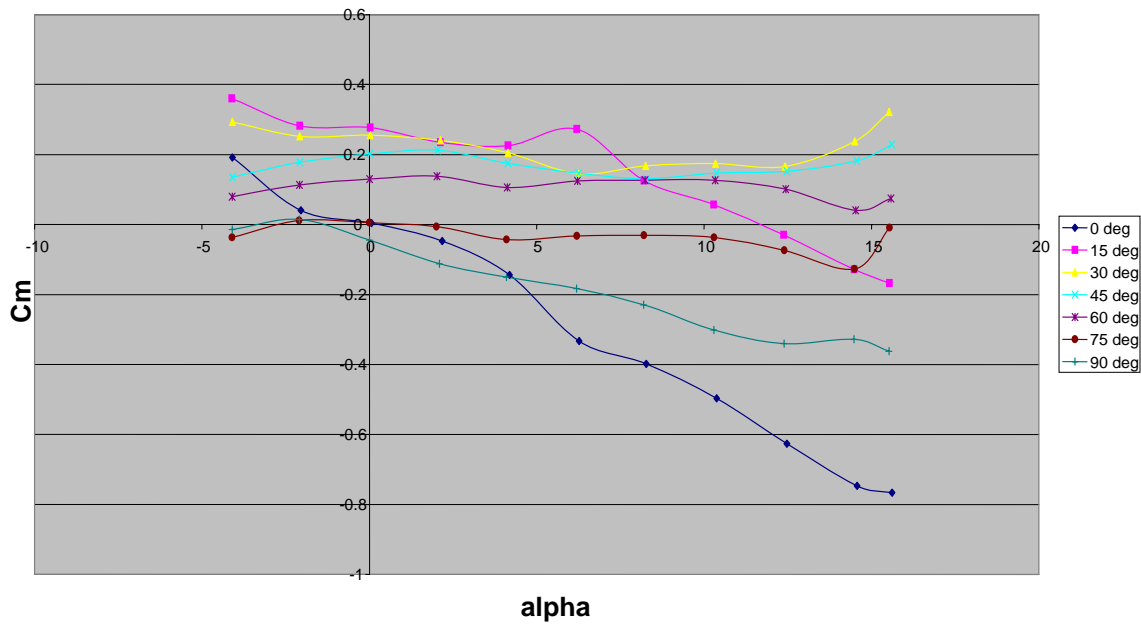


Figure 31. Middle wing C_m vs alpha - 60 mph.

In-ground effects

The missile and wing were run upside down over a ground plane in order to simulate release from an aircraft. This puts the missile in-ground effect. The model was run at two different speeds, 50 and 60 mph, and at two different heights with h/b ranging from 0.071 with plane 2 at $\lambda = 0$ to 1.94 with plane 1 and $\lambda = 90$. The h/b is different for every configuration because as λ varies so does b . A complete list of all h/b values can be found in Table 6.

The values of C_L versus alpha for all different configurations with the wing in middle, including the runs without the ground plane, are shown below in Figs. 32 to 38. For all cases plane one refers to the ground plane farther away from the wing. In all cases the lift goes up dramatically as the ground planes get closer to the model. This was to be expected. It is somewhat hard to get a true idea of what is occurring because the ground plane tests had to be limited due to the model coming in contact with the plane above certain angles of attack. With plane one installed the model could only be run to -5 deg angle of attack, which after swapping the sign becomes +5 deg, because any less angle of attack would have caused the missile nose to strike the ground plane. Similarly, with plane two installed the angle of attack could not be lower than -2 deg. It should also be noted that for $\lambda = 90$ deg and plane one installed the h/b is 1.94 which is outside of the normally recognized limit for IGE of $h/b = 1$. Although this is the case, you can still see a clear increase in lift coefficient with ground plane one installed in Fig. 38.

For all cases there is not much difference between the data at 50 and 60 mph. At $\lambda = 0$ deg the difference between the IGE and OGE results is not as dramatic as it was for the other configurations, although it did stall at 2 deg IGE as opposed to 4 deg OGE. The

smallest increases in C_L are at $\lambda = 0$ and 90 deg, with the largest being at $\lambda = 30, 45$ and 60 deg. Also, for the cases where there is a large difference between C_L IGE and OGE, most notably $\lambda = 30, 45$ and 60 deg, the increase between plane one and plane two is nowhere near as large as the difference between OGE and plane one. The IGE curves for 0, 15, 30, 45, and 60 deg are all pretty similar. The increase in C_L is then caused by the differences in the OGE curves.

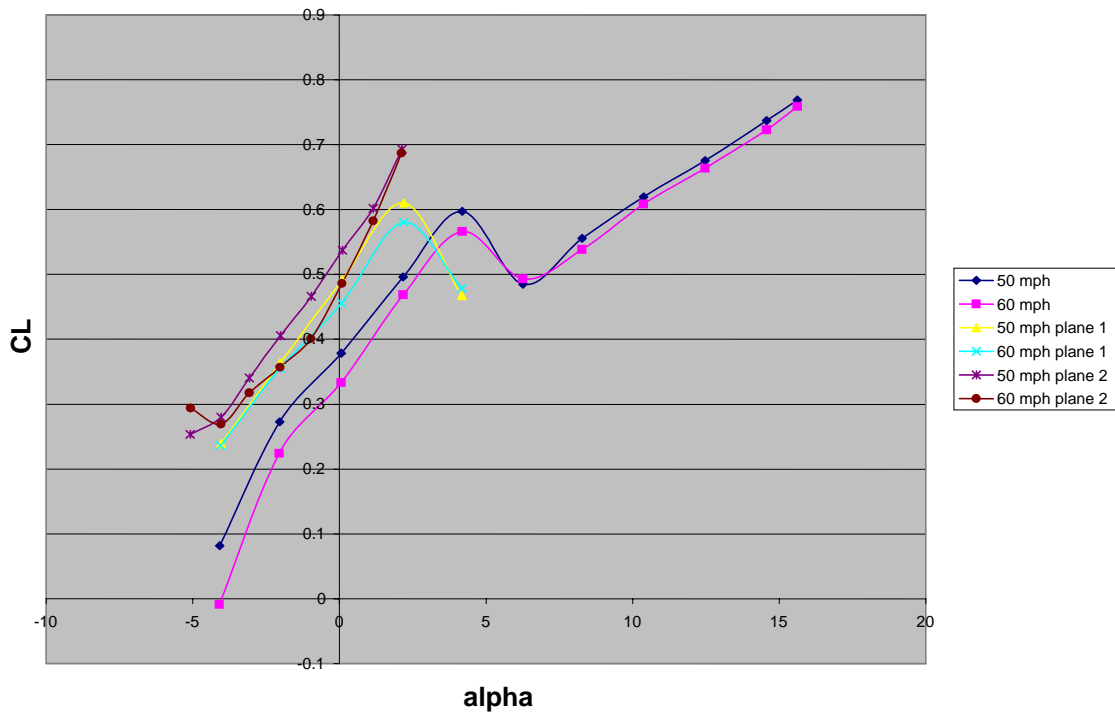


Figure 32. Middle wing C_L vs α – $\lambda = 0$ deg IGE.

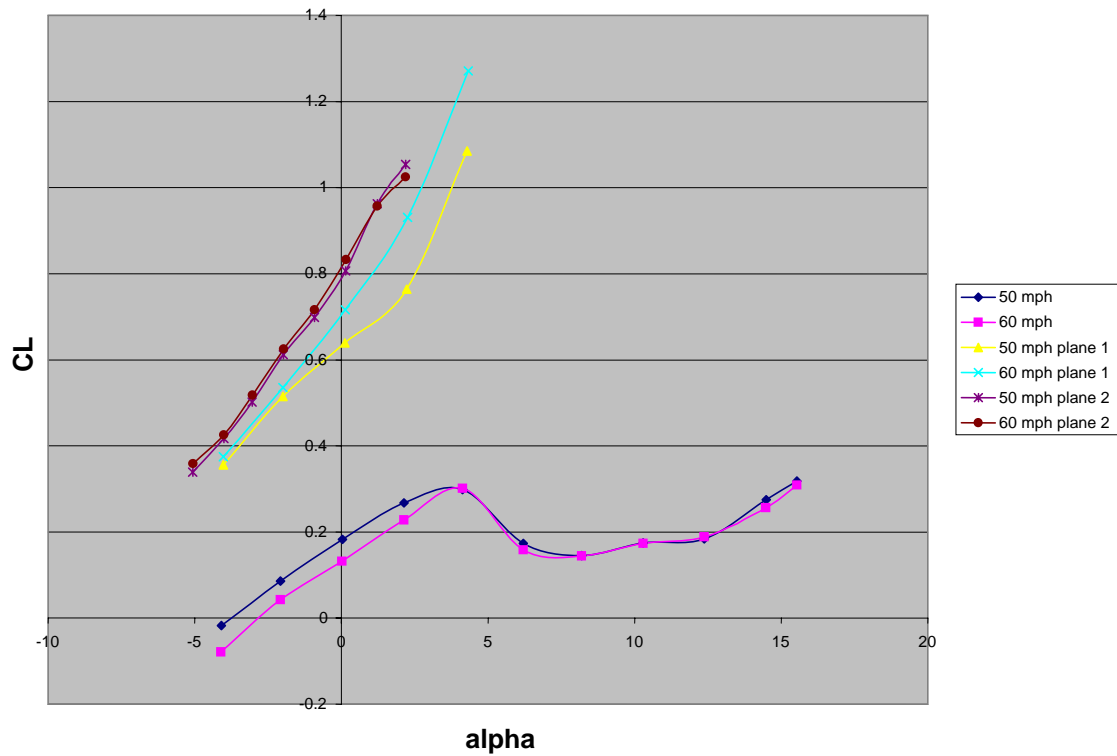


Figure 33. Middle wing C_L vs α – $\lambda = 15$ deg IGE.

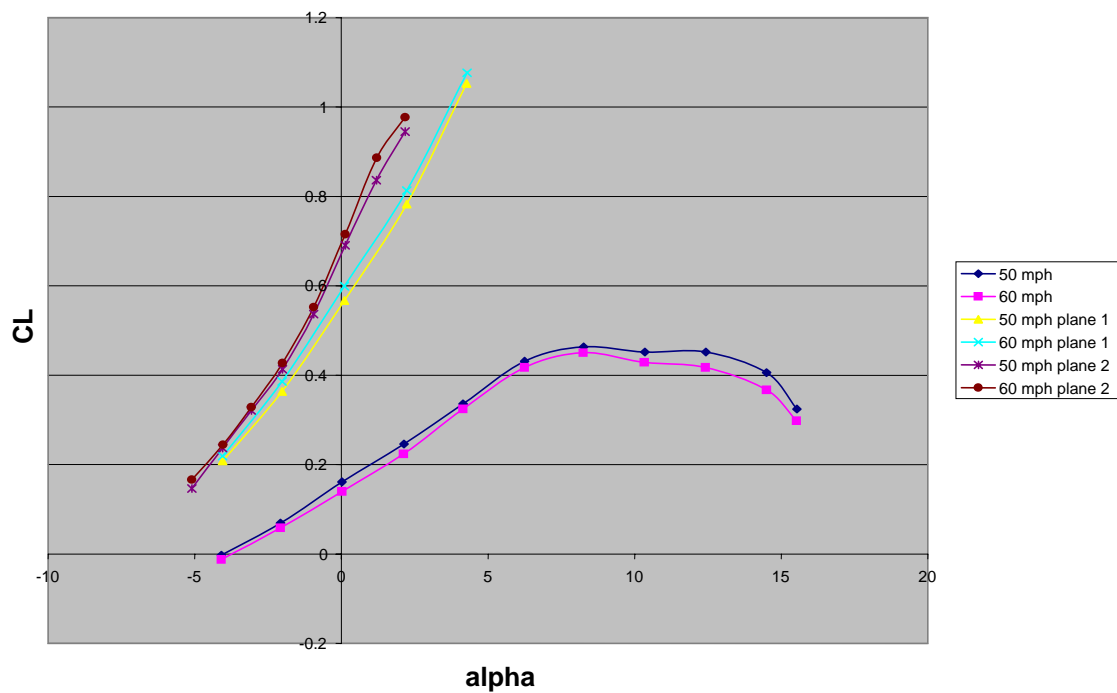


Figure 34. Middle wing C_L vs α – $\lambda = 30$ deg IGE.

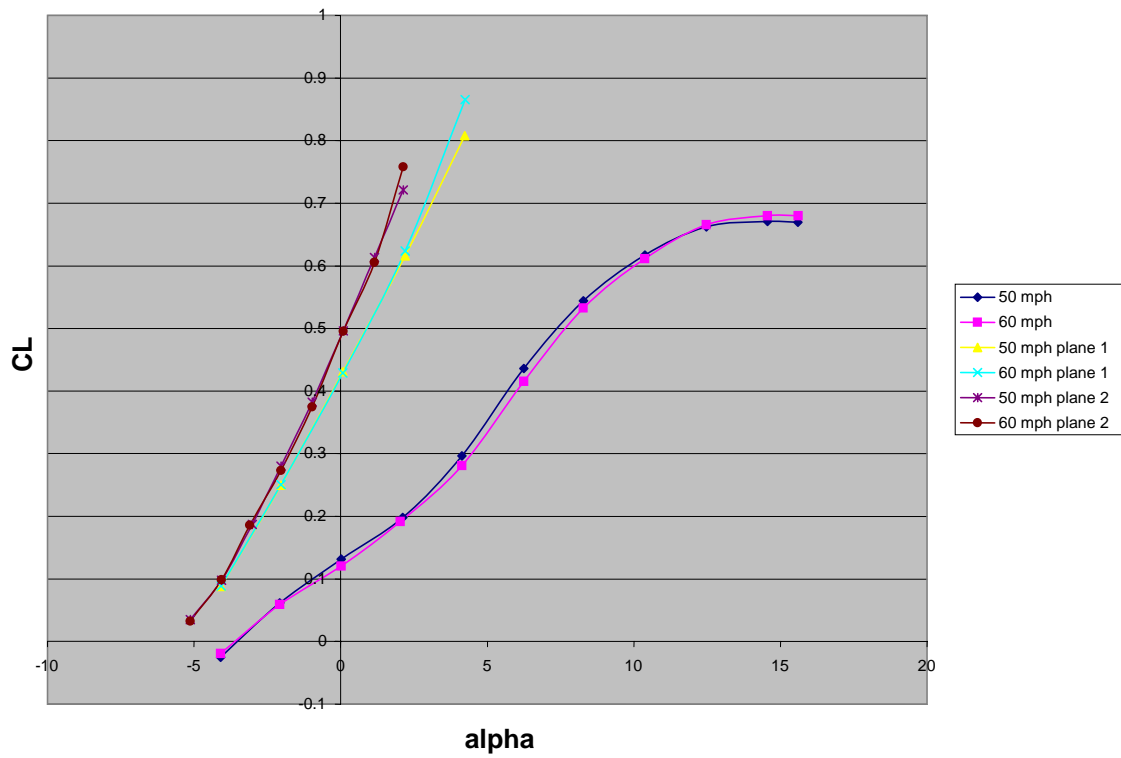


Figure 35. Middle wing C_L vs α – $\lambda = 45$ deg IGE.

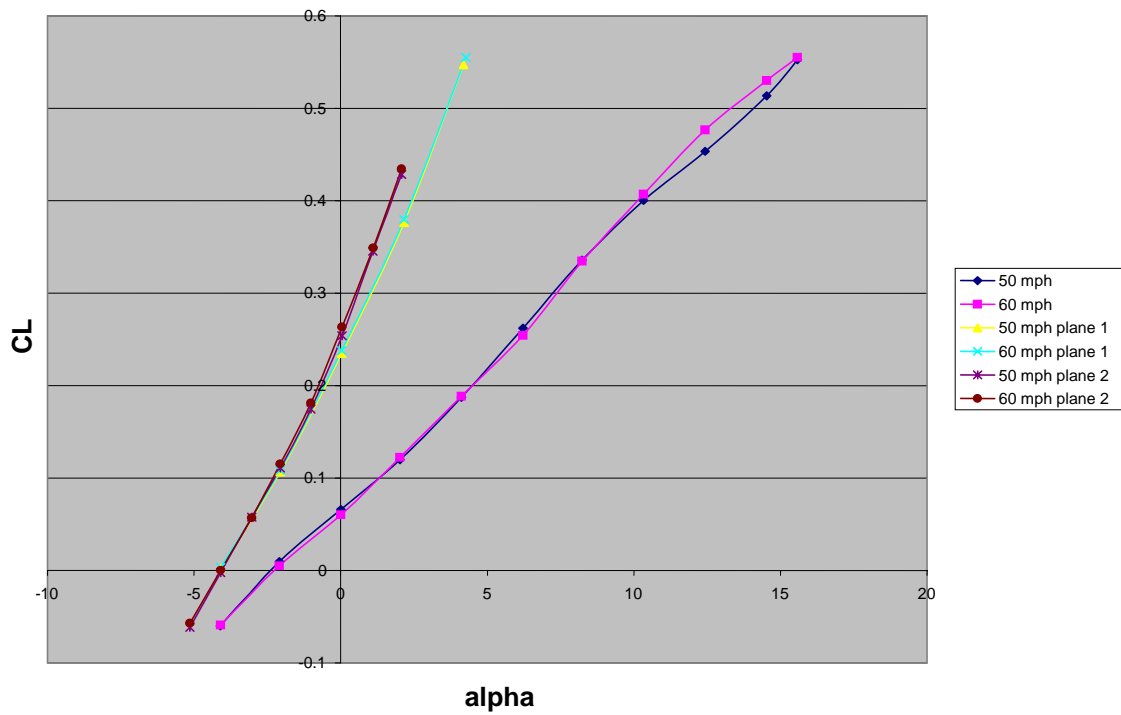


Figure 36. Middle wing C_L vs α – $\lambda = 60$ deg IGE.

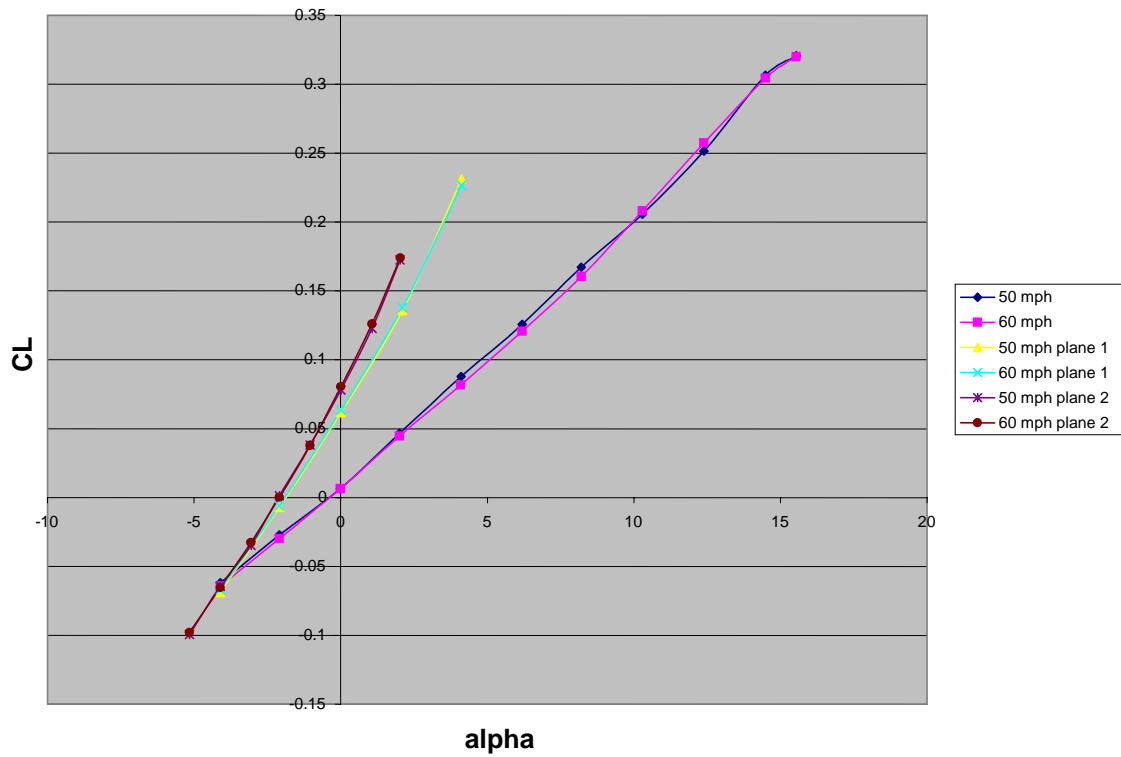


Figure 37. Middle wing C_L vs $\alpha - \lambda = 75$ deg IGE.

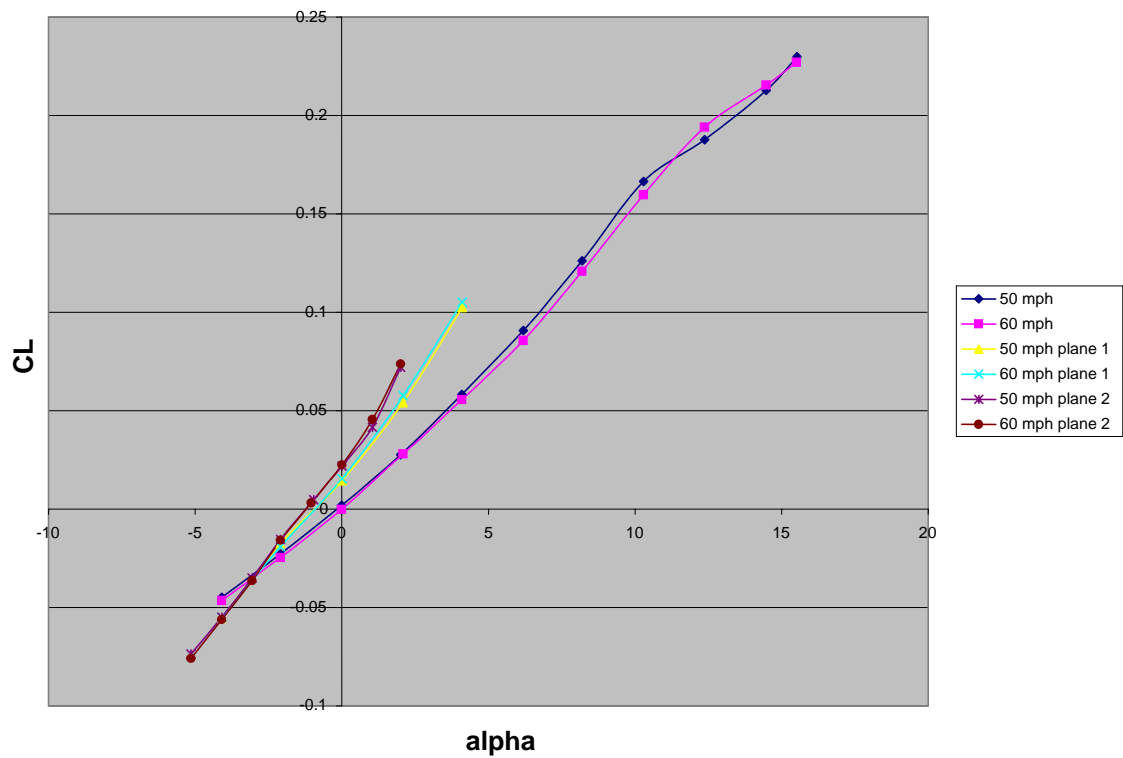


Figure 38. Middle wing C_L vs $\alpha - \lambda = 90$ deg IGE.

Next the drag coefficient variation with ground plane height was analyzed for every middle wing configuration. The plots of C_D versus α are shown in Figs. 39 to 45. These plots are zoomed in on the area where the ground plane measurements were taken to get a better picture of what is happening. With the exception of $\lambda = 75$ and 90 deg, the values of C_D increase as the ground plane gets closer as long as α is positive. This was a somewhat expected result when looking at the C_L curves when IGE. A major contributor to the overall drag is the induced drag, also known as drag due to lift. The results don't match very well with the results predicted using McCormick's induced drag factor. According to his formula, any h/b value of less than around 0.5 should give a lower induced drag [14]. In this study, all h/b values tested gave a higher induced drag, which does agree with Lee [18] and Curry [20] who state that any increase in drag is possible while IGE.

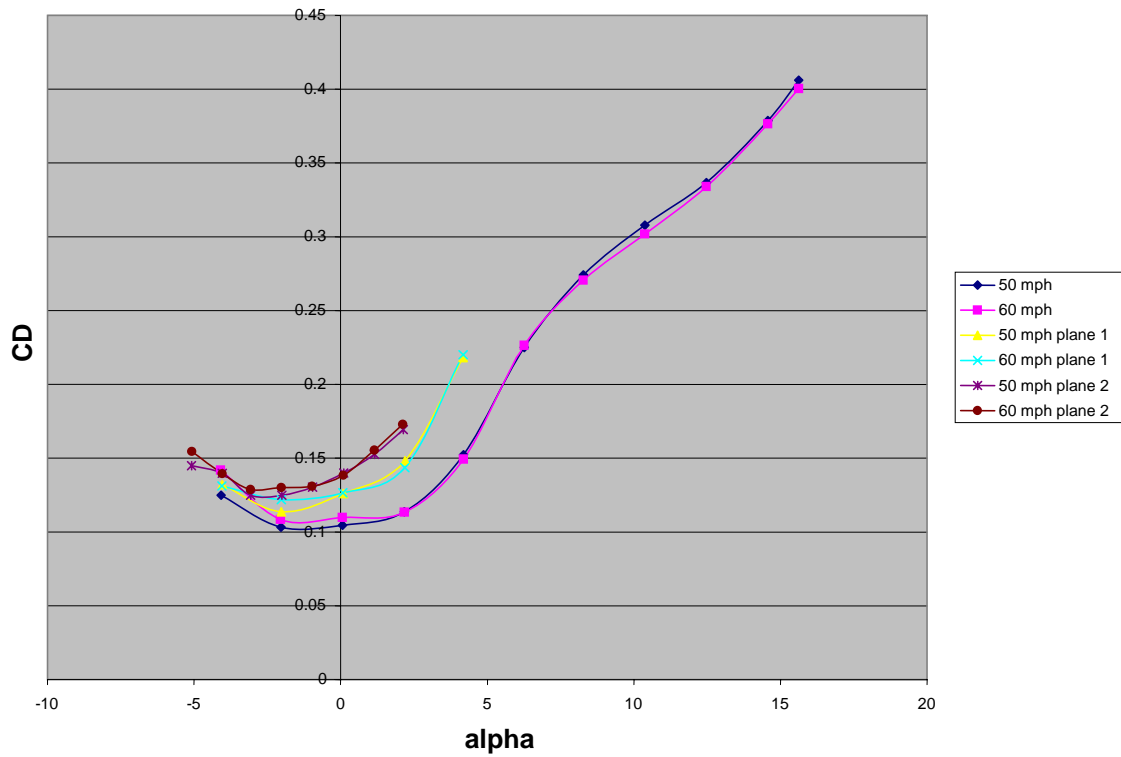


Figure 39. Middle wing C_D vs α – $\lambda = 0$ deg IGE.

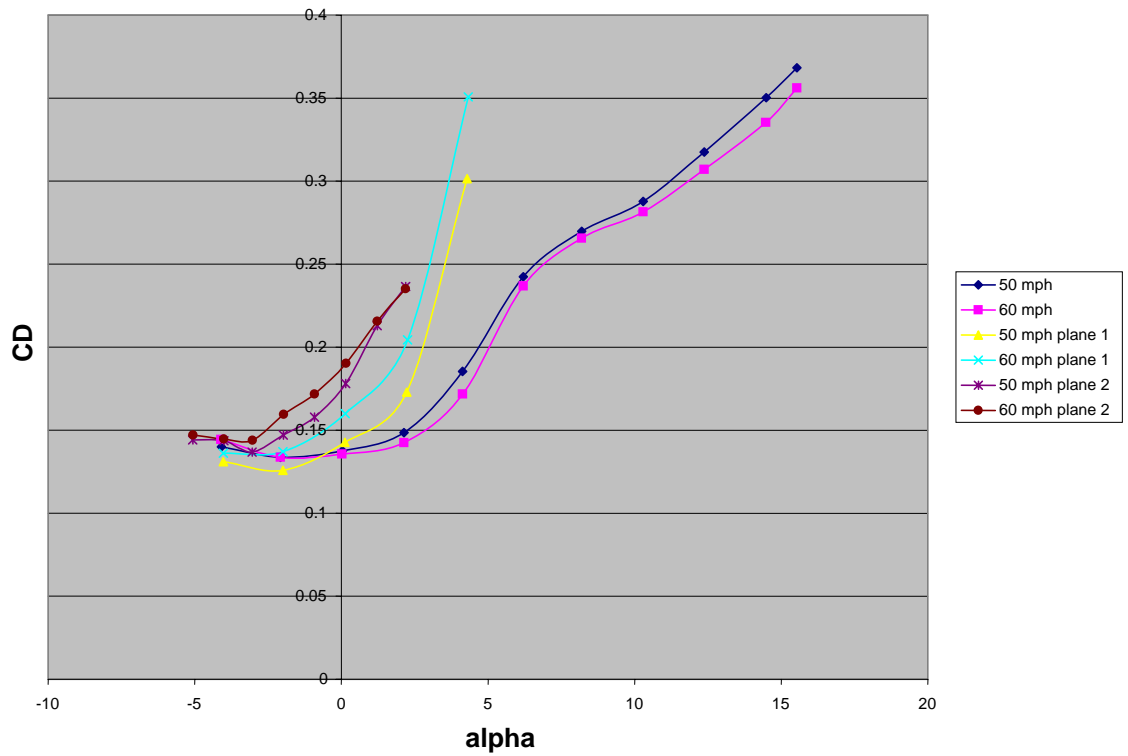


Figure 40. Middle wing C_D vs α – $\lambda = 15$ deg IGE.

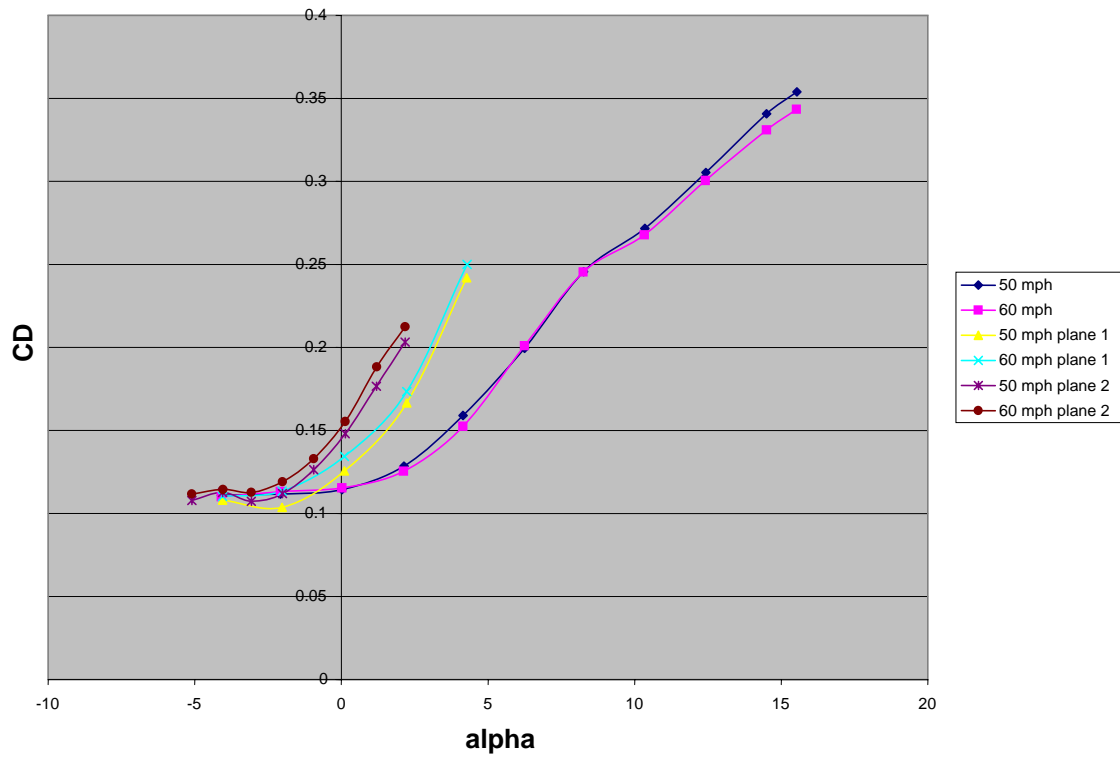


Figure 41. Middle wing C_D vs α – $\lambda = 30$ deg IGE.

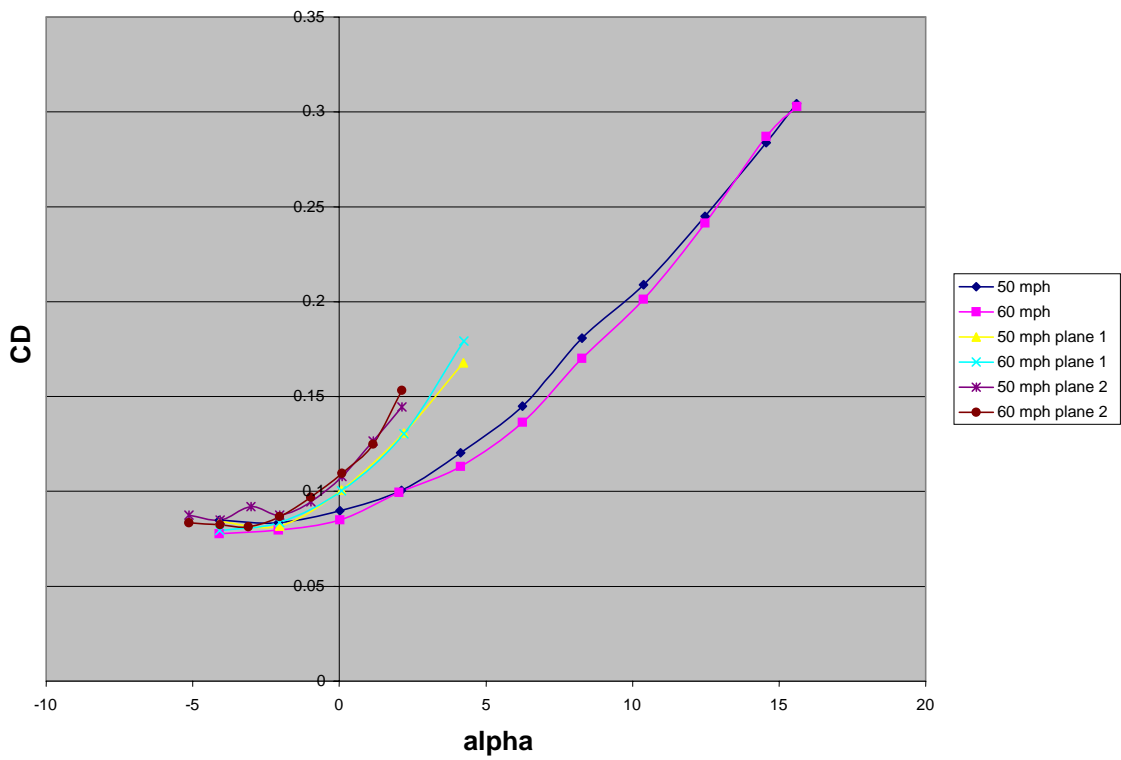


Figure 42. Middle wing C_D vs α – $\lambda = 45$ deg IGE.

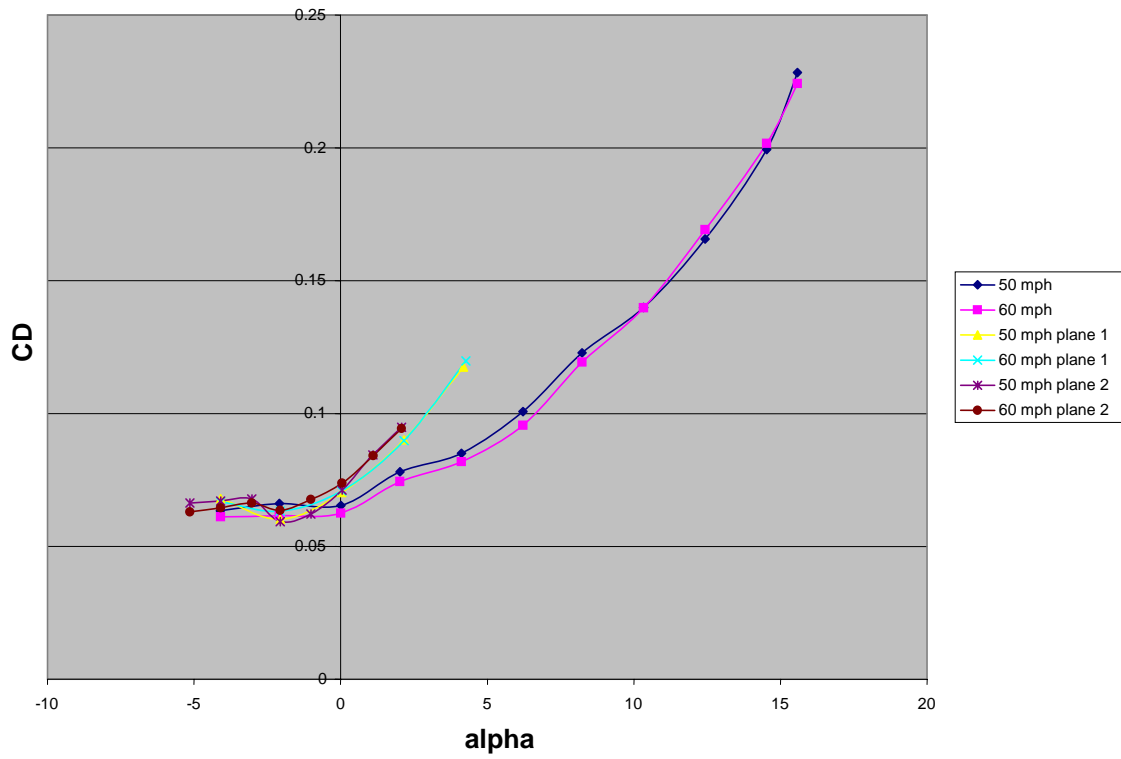


Figure 43. Middle wing C_D vs $\alpha - \lambda = 60^\circ$ IGE.

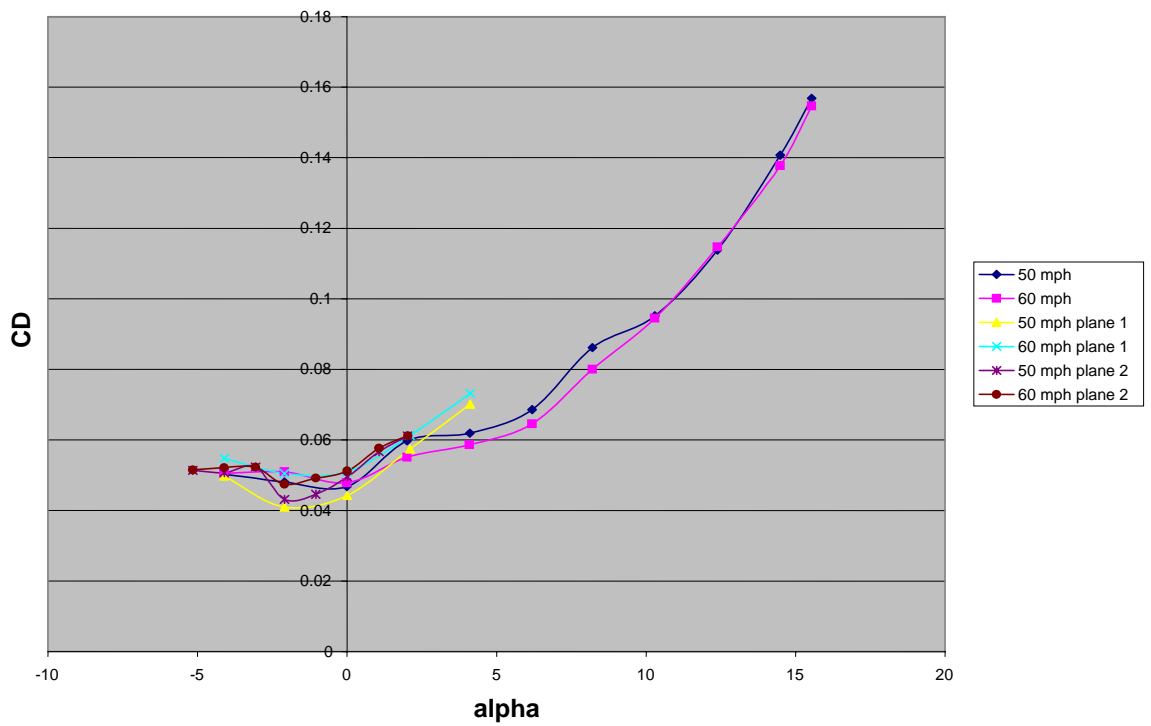


Figure 44. Middle wing C_D vs $\alpha - \lambda = 75^\circ$ IGE.

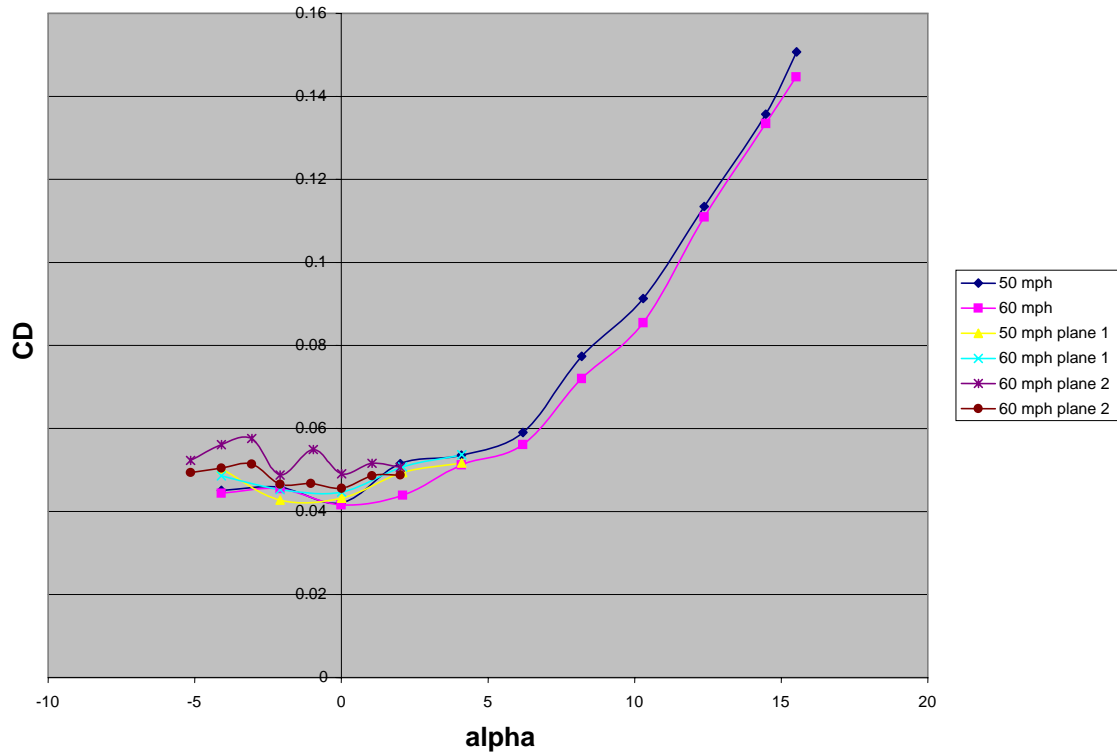


Figure 45. Middle wing C_D vs α – $\lambda = 90$ deg IGE.

A very important consideration in the release of weapons is the variation of C_m with the ground plane in place. This will dictate if the missile is going to tend to want to fly back up into the aircraft in the presence of a small disturbance. The C_m versus α curves are shown in Figs. 46 to 52. The model shows much better longitudinal stability IGE than it did OGE. The only configuration of concern would be at $\lambda = 0$, shown in Fig. 46. The slope of the line is virtually zero. Assuming the missile would be released at $\lambda = 90$ and then morph into a $\lambda = 0$ configuration, the missile should be well clear of the aircraft before any effects would be seen and the model performed very well longitudinally at $\lambda = 0$ OGE. All of the other configurations had a nice, negative slope which is desirable for pitch stability.

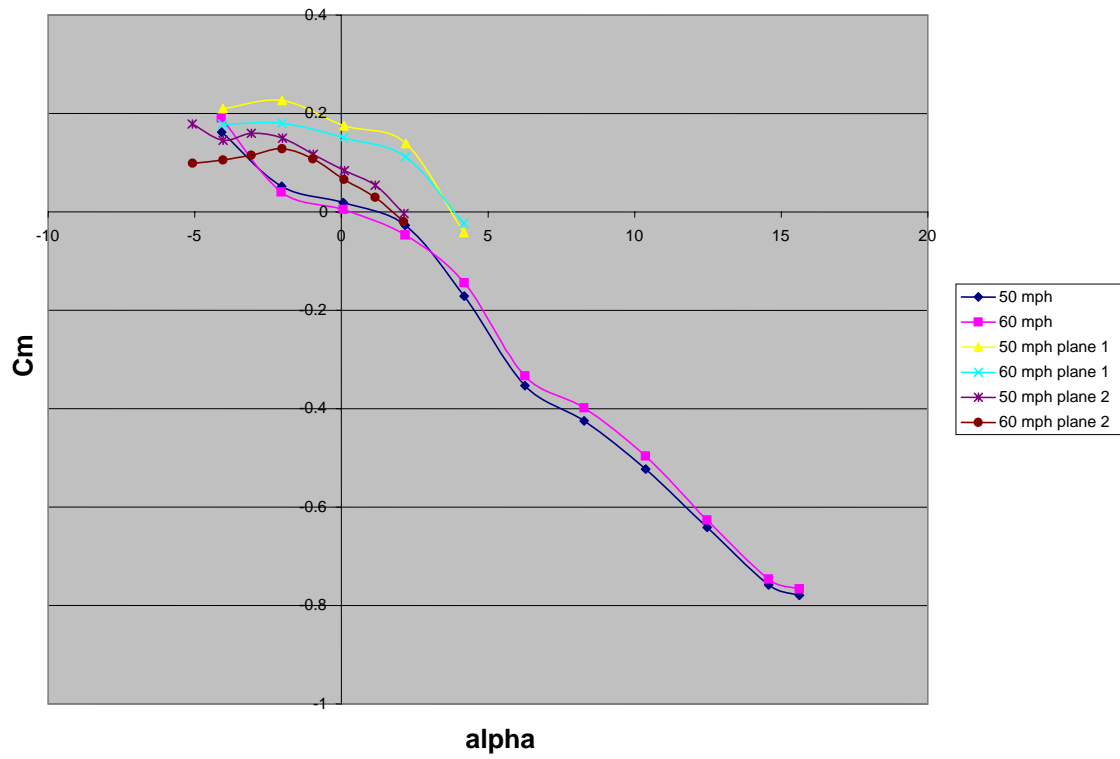


Figure 46. Middle wing C_m vs α – $\lambda = 0$ deg IGE.

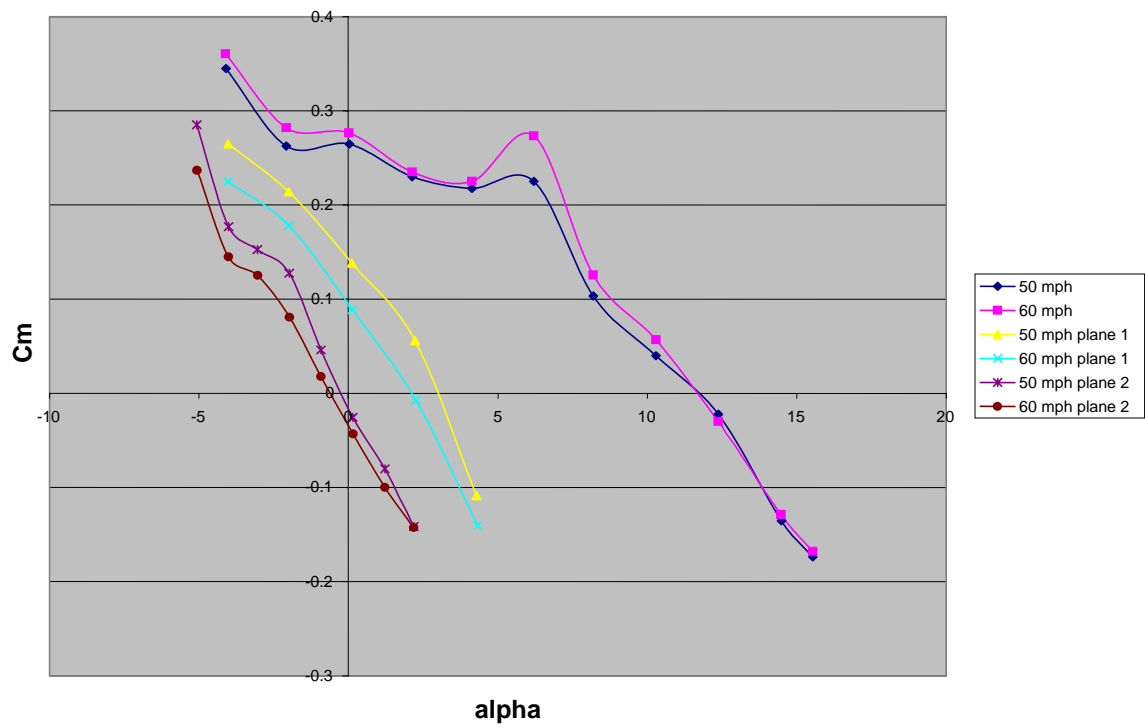


Figure 47. Middle wing C_m vs α – $\lambda = 15$ deg IGE.

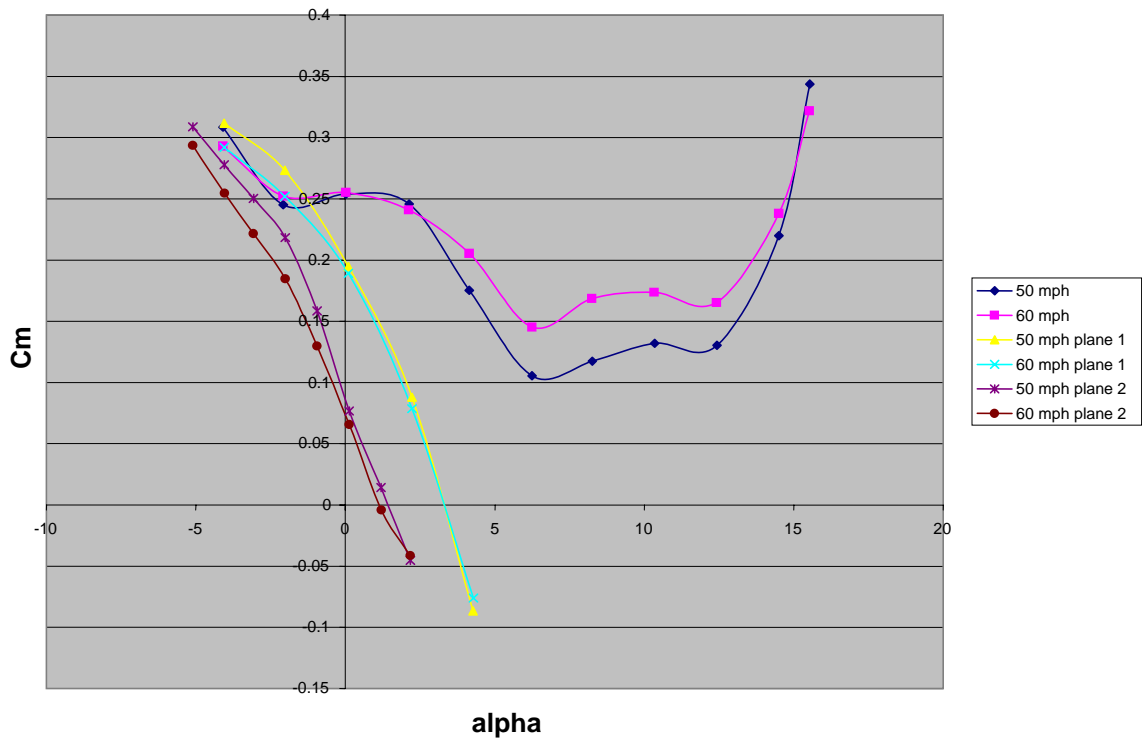


Figure 48. Middle wing C_m vs α – $\lambda = 30$ deg IGE.

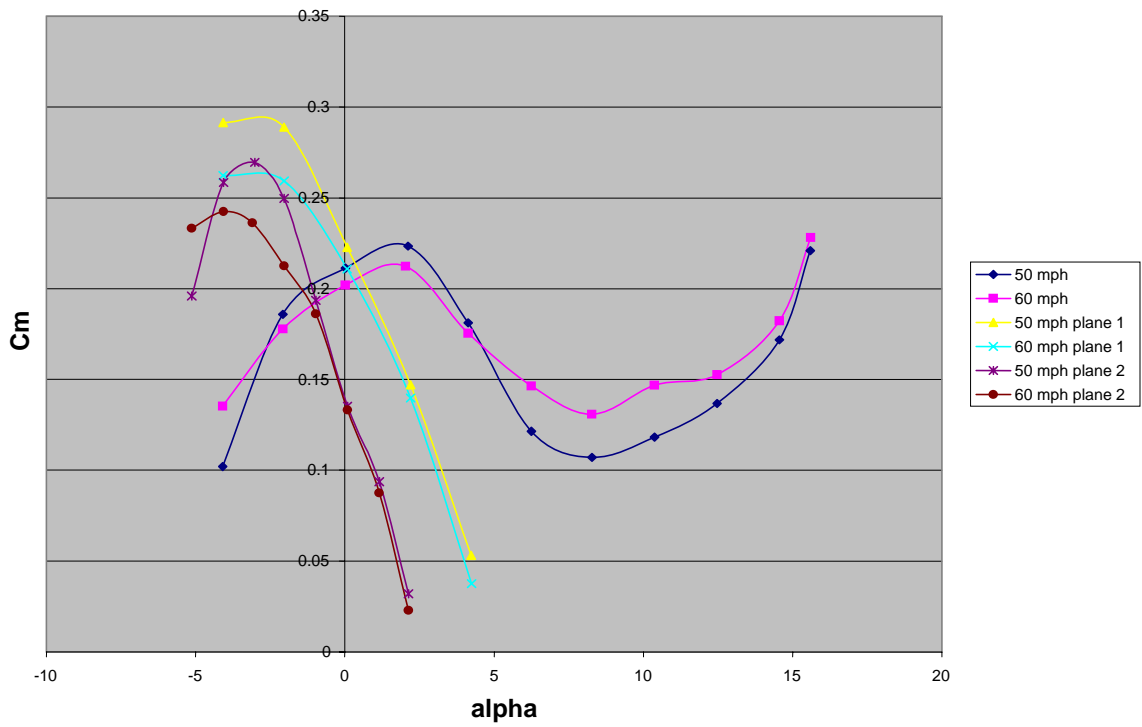


Figure 49. Middle wing C_m vs α – $\lambda = 45$ deg IGE.

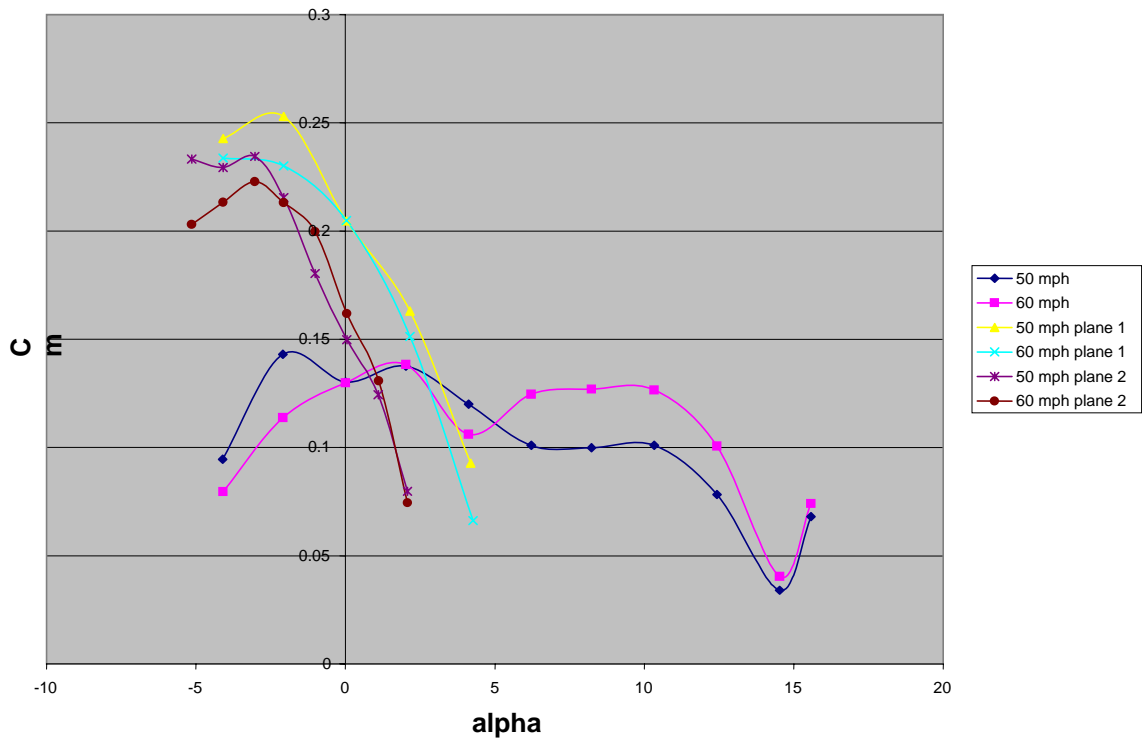


Figure 50. Middle wing C_m vs α – $\lambda = 60$ deg IGE.

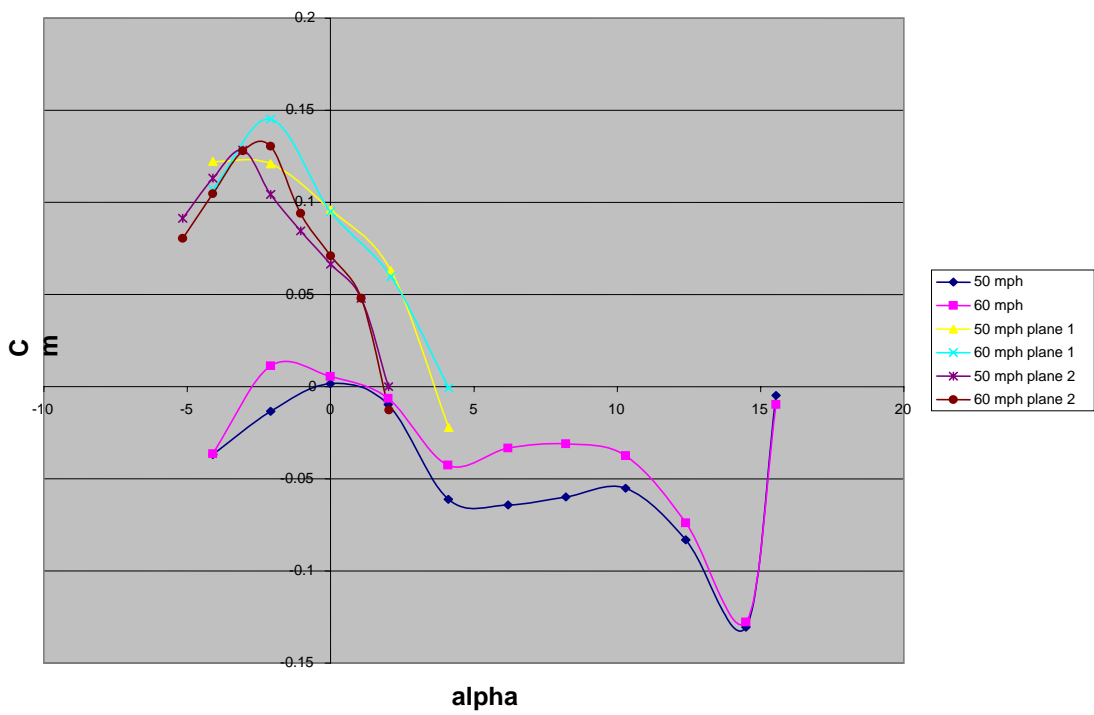


Figure 51. Middle wing C_m vs α – $\lambda = 75$ deg IGE.

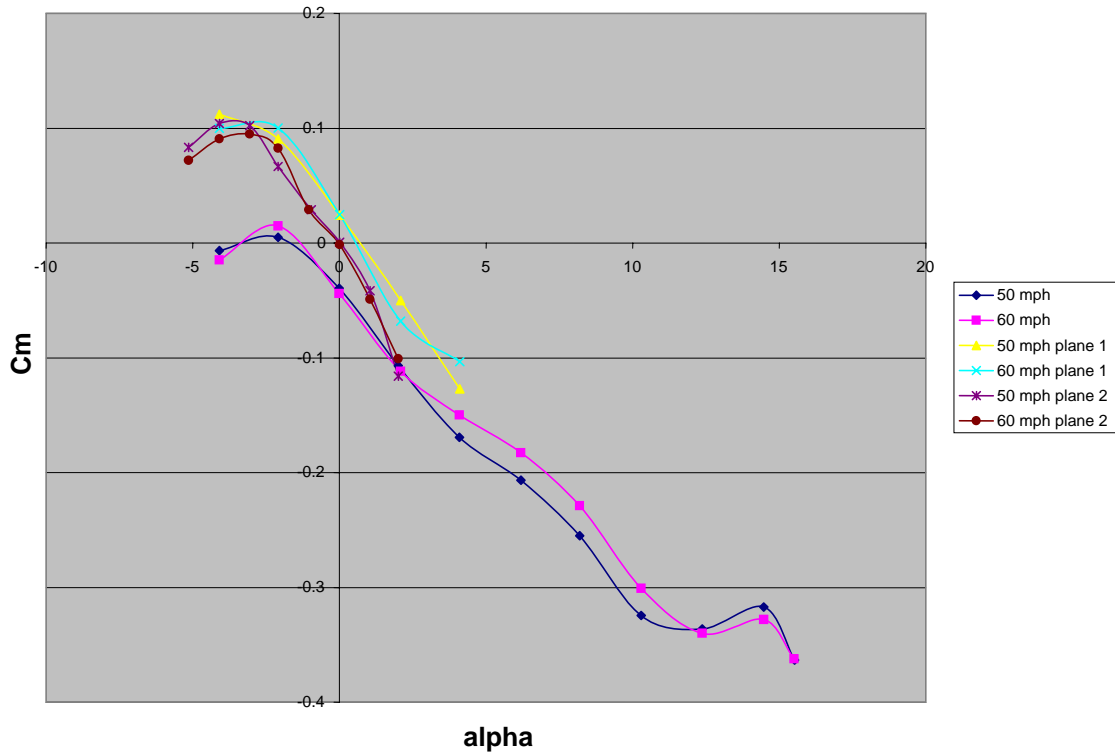


Figure 52. Middle wing C_m vs α – $\lambda = 90$ deg IGE.

Front wing

There were additional attachment points at the front of the missile used in the joined wing experiments, so the wing was mounted at that point and the tests repeated. Figs. 53 and 54 show C_L as a function of α for 50 and 60 mph. Once again the wing stalls, but this time at an angle of attack of 2 deg, and this configuration does not recover as quickly as when the wing is in the middle. This causes a lower C_L maximum than with the middle wing. The maximum C_L at $\alpha = 0$ is just under 0.3 and occurs at $\lambda = 0$ with C_L decreasing as λ is increased, as would be expected. There is not much difference between the curves for 50 and 60 mph. At both speed the maximum C_L occurred at $\lambda = 45$ deg, as opposed to occurring at $\lambda = 0$ deg for the middle wing configuration. Also, the maximum

value of C_L is only about one-half of the maximum value for the middle wing. For the sweep angles that did not stall, C_L increased as the sweep angle decreased.

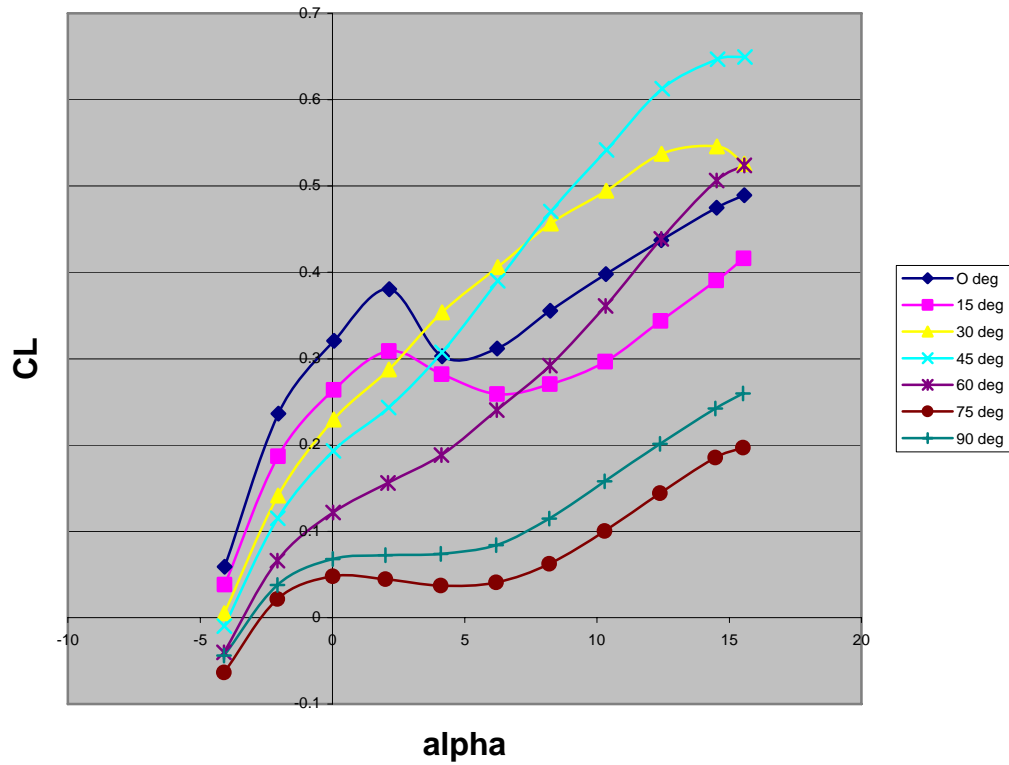


Figure 53. Front wing C_L vs α - 50 mph.

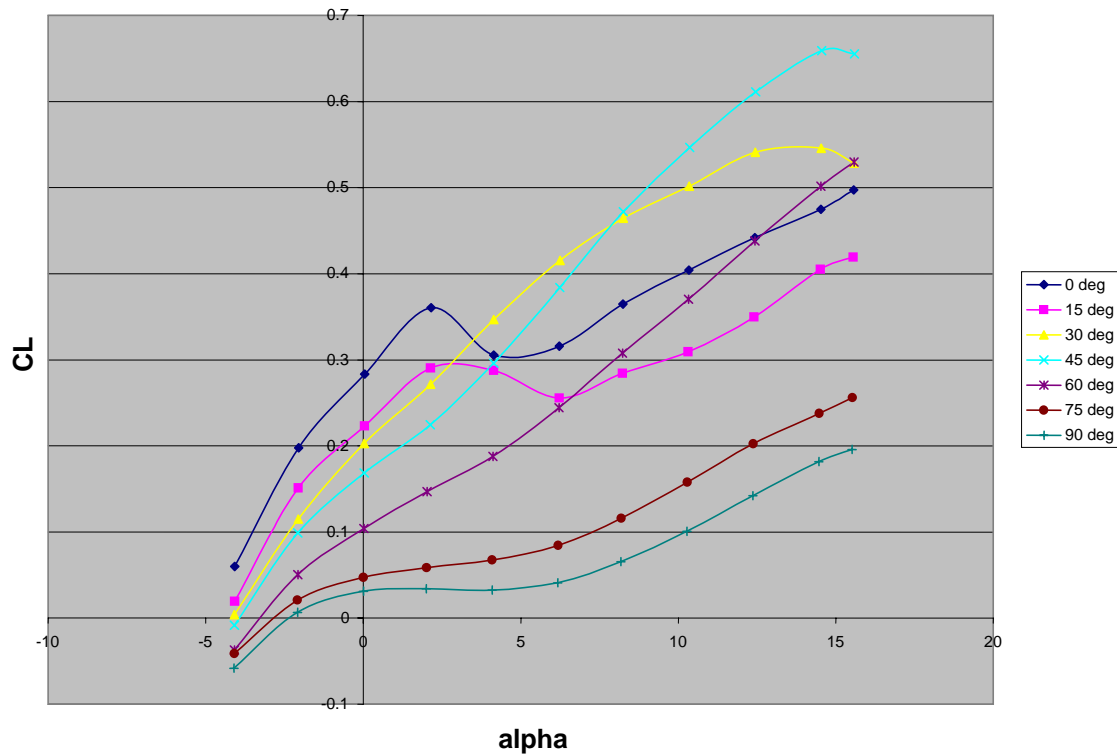


Figure 54. Front wing C_L vs alpha - 60 mph.

The drag coefficient, C_D , is plotted as a function of α in Figs. 55 and 56. All the curves have the same basic shape with the exception of $\lambda = 0$ and 15 deg around the time when stall occurred at $\alpha = 4$ deg. It is interesting to note that at $\alpha = 0$, C_D values are in order of increasing λ with 0 deg having the lowest value and 90 deg registering the highest drag. These values switch at higher angles of attack with $\lambda = 0$ having the highest value at $\alpha = 15$ and $\lambda = 90$ having the lowest value of C_D . You can also see that at $\alpha = 0$ deg the drag on the $\lambda = 0, 15, 30$ and 45 deg configurations is essentially zero. The C_D for $\lambda = 0, 30, 45$, and 60 deg drops below 0, which is also puzzling. This could partially be due to the disturbed airflow due to the nose causing a suction effect. Another anomaly caused by the interaction between the wing on the front of the missile and the nose could also be the cause. Pressure measurements and possibly flow visualization are needed to

accurately diagnose the cause of these drag curves. The shape of the curves also differs from parabolic shape normally seen in C_D versus alpha plots.

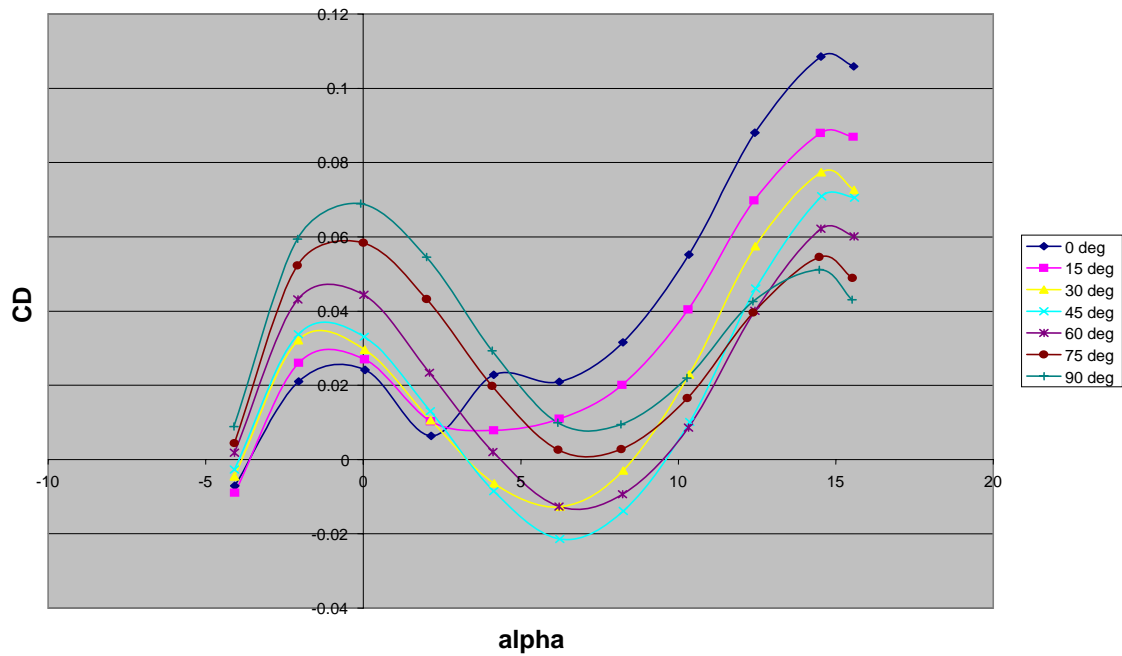


Figure 55. Front wing C_D vs alpha - 50 mph.

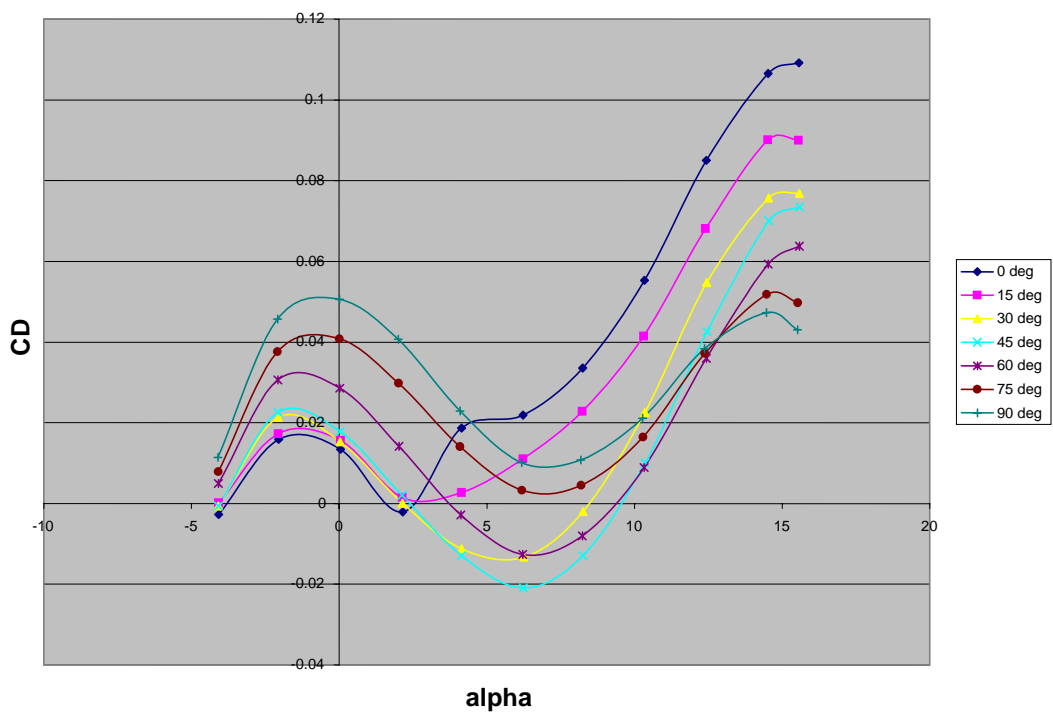


Figure 56. Front wing C_D vs alpha - 60 mph.

The next parameter to be examined is the pitch moment coefficient, C_m , measured about the center of gravity, CG, of the model. C_m as a function of α is shown in Figs. 57 and 58. This configuration provides much worse pitch stability than the middle wing configuration. This is primarily due to the placement of the wing. With the wing located near the CG, the moment arm is greatly reduced producing a much smaller pitch up moment due to the lift created by the wing. This smaller moment can be much more easily counteracted by the small tail. The only configuration that is truly longitudinally stable is at $\lambda = 90$ deg and even this configuration is only very slightly stable. The rest of the configurations begin longitudinally unstable, although the $\lambda = 0$ and 15 deg configurations do become slightly stable after stall. There is also very little difference between the 50 and 60 mph data.

This missile was designed without the wing so therefore has a relatively small tail when compared to the wing. The tail is too small to overcome the upward pitching moment created by the wing producing lift. If this model were to fly the tail would have to be redesigned and made much bigger to achieve longitudinal stability.

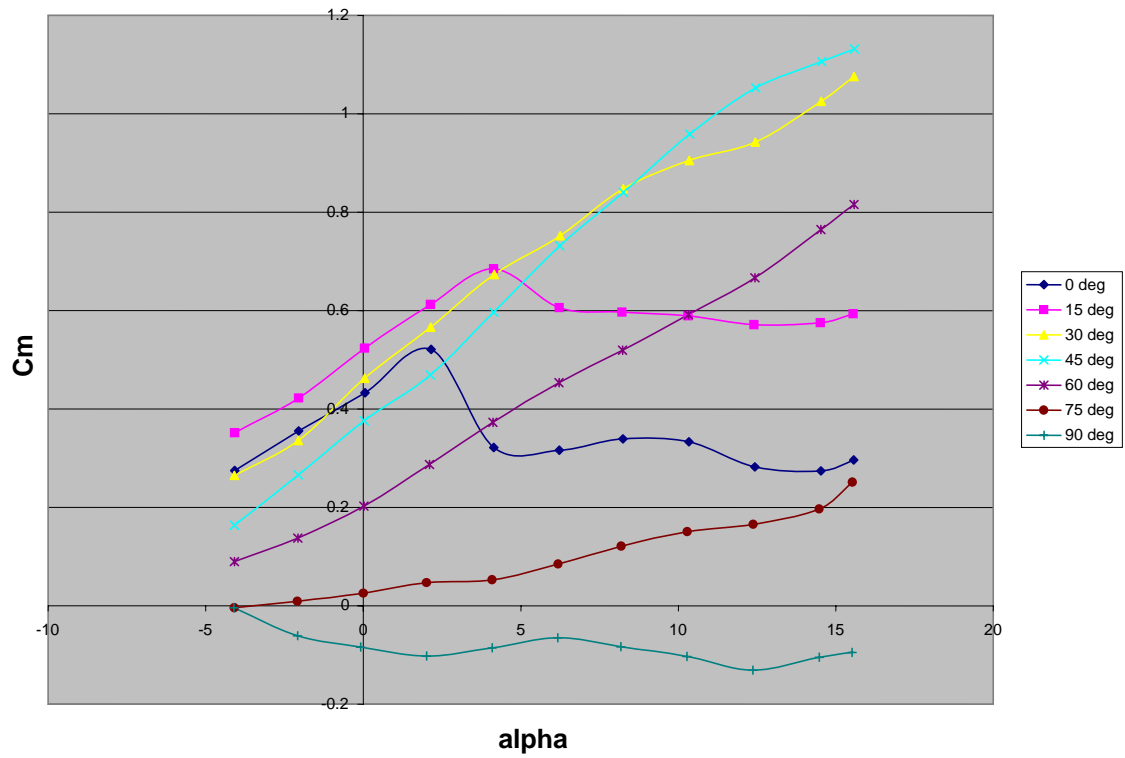


Figure 57. Front wing C_m vs alpha - 50 mph.

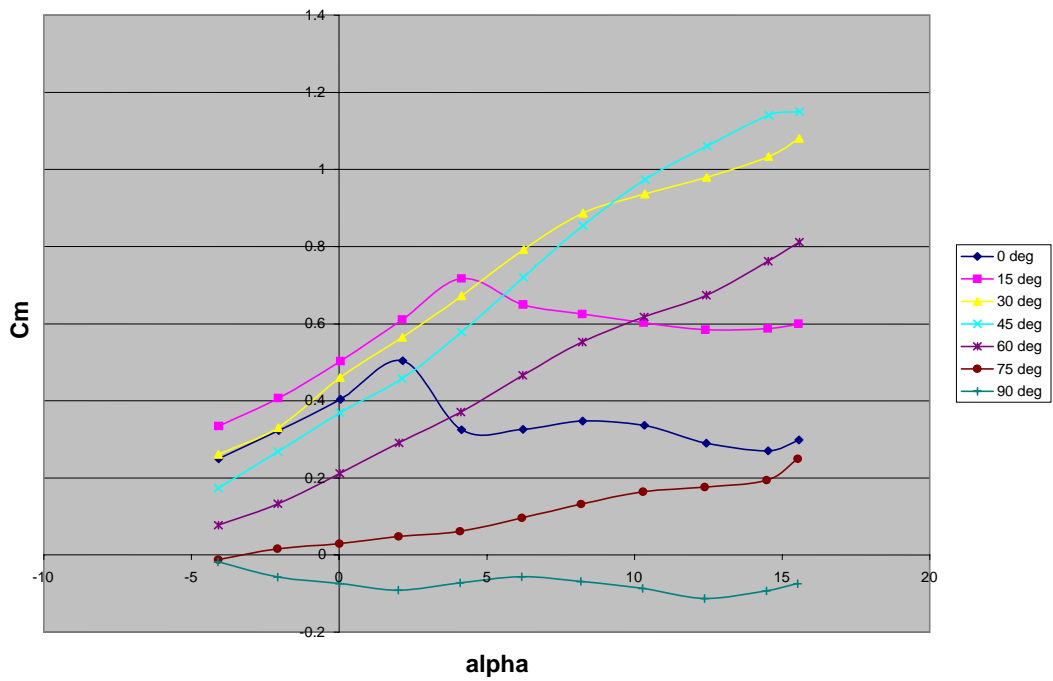


Figure 58. Front wing C_m vs alpha - 60 mph.

The IGE plots for the front wing configuration can be seen in Appendix B. Overall the increase in C_L IGE for the front wing, shown in Figs. 59 to 65, was not as large as for the middle wing and in the case of $\lambda = 60, 75$, and 90 deg it actually went down. The C_D increase IGE, shown in Figs. 66 to 72, was also much higher than the increase for the middle wing for most configurations. The IGE C_D values were similar for the front and middle wings, but the OGE values for the front wing were so low that the net increase from OGE to IGE was higher. Also, with the ground planes installed the drag never goes negative like it does OGE. The pitch moment performance is bad IGE, shown in Figs. 73 to 79, with the front wing, like it was OGE.

Uncertainty Analysis

The uncertainty of a function of several variables can be found using the partial derivatives. For instance, if $y = f(x_1, x_2, \dots)$ the uncertainty dy can be found using equation (3) [33].

$$dy = \sqrt{\left(\frac{\partial y}{\partial x_1} dx_1\right)^2 + \left(\frac{\partial y}{\partial x_2} dx_2\right)^2 + \dots + \left(\frac{\partial y}{\partial x_n} dx_n\right)^2} \quad (3)$$

For this analysis, the uncertainties of the individual measurements were given in manufacturer specifications for the devices used to make the measurements and are shown in Table 9. The wing area and angle of attack are assumed to be accurate.

Table 9. Measurement uncertainties.

Measurement	Uncertainty
N	0.0625 lb _f
A	0.075 lb _f
V	0.25 mph
ρ	0.01 psi

The uncertainties were then calculated for the 50 mph, middle wing configuration for the lift and drag coefficients. The maximum uncertainty for C_L was 0.038 and for C_D was 0.045. The maximum value of C_L for this test was 0.75 giving an uncertainty of approximately 5%. For this test the maximum value of C_D was 0.41 giving an uncertainty of 11%.

Conclusions and Recommendations

Section 1 - Conclusions

The model was tested OGE with the wing installed both on the front of the missile and in the middle and the sweep angle varying from 0 to 90 deg. The wing stalled at an angle of attack of either 2 or 4 deg depending on the wing placement. The middle wing configuration produced more lift, but also significantly more drag than the front wing. The validity of the drag calculations is up for debate due to the fact that in certain configurations, a negative drag was measured. In order to get a true understanding of what is happening, additional testing will need to be accomplished using pressure transducers and some sort of flow visualization. The model also showed good longitudinal stability in the middle wing configuration, but poor stability with the front wing. This is caused by the tail not being large enough to overcome the increased moment arm between the lift and the CG.

The model was also tested inverted over the ground plane to simulate dropping after release from an aircraft. With the wing installed in the middle the model exhibited a higher C_L but also a higher C_D than in identical conditions OGE. The higher C_L was expected, but the increase in C_D was somewhat unexpected even though several studies have shown that certain aircraft do experience higher drag IGE than OGE. The model also performed well longitudinally IGE at all sweep angles except for 0 deg. This wouldn't cause a problem because assuming the missile is dropped from the aircraft at $\lambda = 90$ deg and then swept to the optimal angle, if it did sweep to $\lambda = 0$ deg, the missile would be well clear of the aircraft where it is stable OGE.

The IGE tests with the wing in the front showed an increase in lift for most configurations. There were a couple of instances where the lift was less IGE than OGE. The drag increase for this configuration was significant, with the drag curves looking more like traditional C_D versus alpha plots. The drag also never goes to zero IGE. Much like the OGE, the front wing setup performed poorly IGE with regards to longitudinal stability.

It was tough to get a true idea of the full ground effects on this model because of the small range of angles of attack that could be tested due to model-ground plane interferences. It would also be helpful to run the missile inverted without the ground plane to verify the approach used in analyzing the data, and also to rule out any other effects. Since the true effects of oblique wings are seen at transonic and supersonic speeds, this study needs to be repeated at those speeds because these results would not apply to the more complex aerodynamics in these regimes.

Section 2 - Recommendations

This study only provides a first look at ground effects for a missile with an oblique wing installed. Based on the results and findings of this study, the following are recommendations for further research:

- redesign the airfoil to avoid the wing stall
- strengthen the wing along its span in order to be able to test at higher Re
- add some method of flow visualization to see the span wise airflow
- accomplish a CFD analysis to validate results
- re-accomplish these tests at both transonic and supersonic speeds

- run front wing tests with pressure transducers and flow visualization to try and diagnose cause of negative drag
- design a smaller model to allow for more ground plane heights and angles of attack to be tested

Appendix A: Sample Calculations

Data Reduction

Test condition: Missile with no wing installed

$$U = 105.248 \text{ mph} = 154.364 \text{ ft/s}$$

$$\alpha = 12.348 \text{ deg}$$

Test room conditions:

$$T = 534.07 \text{ R}$$

$$P = 14.278 \text{ psi}$$

$$R = 1716 \text{ ft-lb/slug-R}$$

$$\mu = .372 \times 10^{-6} \text{ slug/ft-s}$$

$$\gamma = 1.4$$

$$S = \text{ref area} = 0.4 \text{ ft}^2$$

$$\rho = \frac{P}{RT} = .00224 \frac{\text{lb}_m}{\text{ft}^3}$$

$$q = \frac{1}{2} \rho U^2 = 26.68 \frac{\text{lb}_f}{\text{ft}^2}$$

$$a = \sqrt{\gamma RT} = 1132.72 \frac{\text{ft}}{\text{sec}}$$

Corrected forces obtained from MATLAB

$$A = .1024 \text{ lb}_f$$

$$Y = -.004 \text{ lb}_f$$

$$N = -1.2158 \text{ lb}_f$$

$$l = -.0035 \text{ in-lb}_f$$

$$m = 1.9175 \text{ in-lb}_f$$

$$n = 0.008 \text{ in-lb}_f$$

Angles used

$$\theta = \alpha = 12.348 \text{ deg}$$

$$\psi = 0 \text{ deg}$$

Now to convert from body axes to wind axes

$$\begin{bmatrix} D \\ S \\ L \end{bmatrix} = \begin{bmatrix} A \cos \theta \cos \psi + Y \sin \psi + N \sin \theta \cos \psi \\ -A \sin \psi \cos \theta + Y \cos \psi - N \sin \theta \sin \psi \\ -A \sin \theta + N \cos \theta \end{bmatrix}$$

$$D = .3062 \text{ lb}_f$$

$$S = .004 \text{ lb}_f$$

$$L = .6636 \text{ lb}_f$$

Add blockage corrections [32]

$$\varepsilon_{sb_b} = \frac{\kappa_3 \tau_1 (\text{Body Volume})}{C^{3/2}} = .005489$$

$$U_{\text{corr}} = U (1 + \varepsilon) = 155.369 \text{ ft/s} = 105.934 \text{ mph}$$

$$q_{\text{corr}} = q (1 + \varepsilon) = 26.974 \text{ lb}_f/\text{ft}^2$$

$$C_L = \frac{L}{\frac{1}{2} q_{\text{corr}} S} = .061$$

$$C_D = \frac{D}{\frac{1}{2} q_{\text{corr}} S} = .028$$

$$M = \frac{U_{\text{corr}}}{a} = .137$$

$$\text{Re} = \frac{\rho U_{\text{corr}} l}{\mu} = 2.22 \times 10^6$$

Error Analysis

$$C_L = \frac{L}{\frac{1}{2} \rho V^2 S}$$

and

$$L = N \cos \alpha - A \sin \alpha$$

so,

$$C_L = \frac{N \cos \alpha - A \sin \alpha}{\frac{1}{2} \rho V^2 S}$$

The uncertainty is given by:

$$dC_L = \sqrt{\left(\frac{\partial C_L}{\partial N} dN\right)^2 + \left(\frac{\partial C_L}{\partial A} dA\right)^2 + \left(\frac{\partial C_L}{\partial \rho} d\rho\right)^2 + \left(\frac{\partial C_L}{\partial V} dV\right)^2}$$

With the individual partial derivatives:

$$\frac{\partial C_L}{\partial N} = \frac{\cos \alpha}{\frac{1}{2} \rho V^2 S} = 0.591$$

$$\frac{\partial C_L}{\partial A} = \frac{-\sin \alpha}{\frac{1}{2} \rho V^2 S} = -0.108$$

$$\frac{\partial C_L}{\partial \rho} = \frac{-1(N \cos \alpha - A \sin \alpha)}{\frac{1}{2} \rho^2 V^2 S} = -0.014$$

$$\frac{\partial C_L}{\partial V} = \frac{-2(N \cos \alpha - A \sin \alpha)}{\frac{1}{2} \rho V^3 S} = -0.026$$

Multiplying by the uncertainties for each measurement given in Table 9 gives $dC_L = 0.038$.

Appendix B. Additional Plots

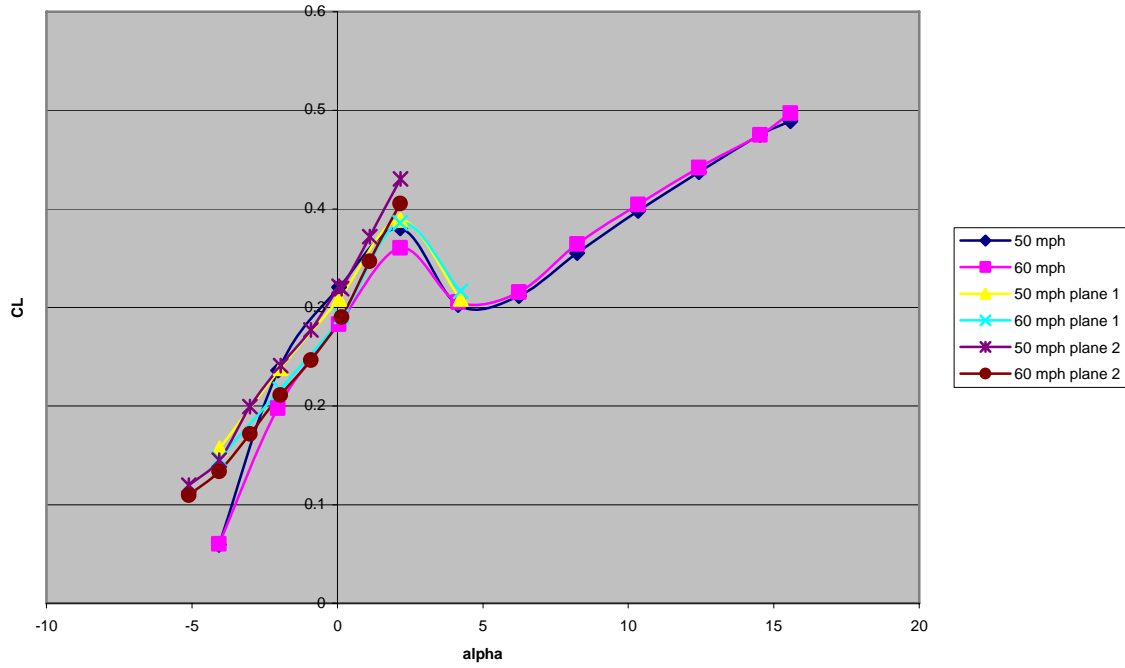


Figure 59. Front wing C_L vs α – $\lambda = 0$ deg IGE.

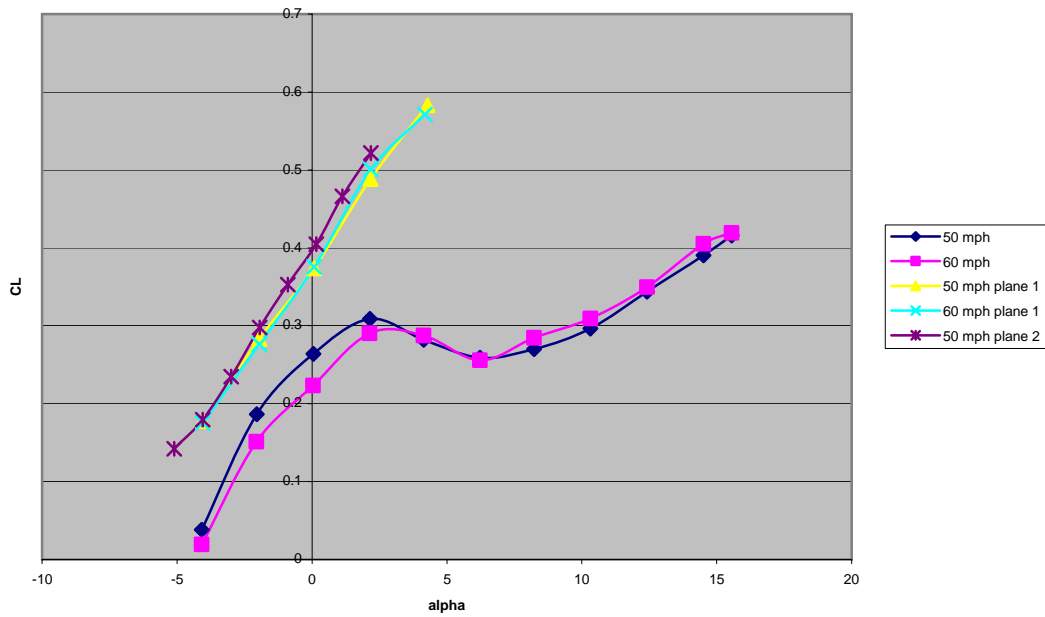


Figure 60. Front wing C_L vs α – $\lambda = 15$ deg IGE.

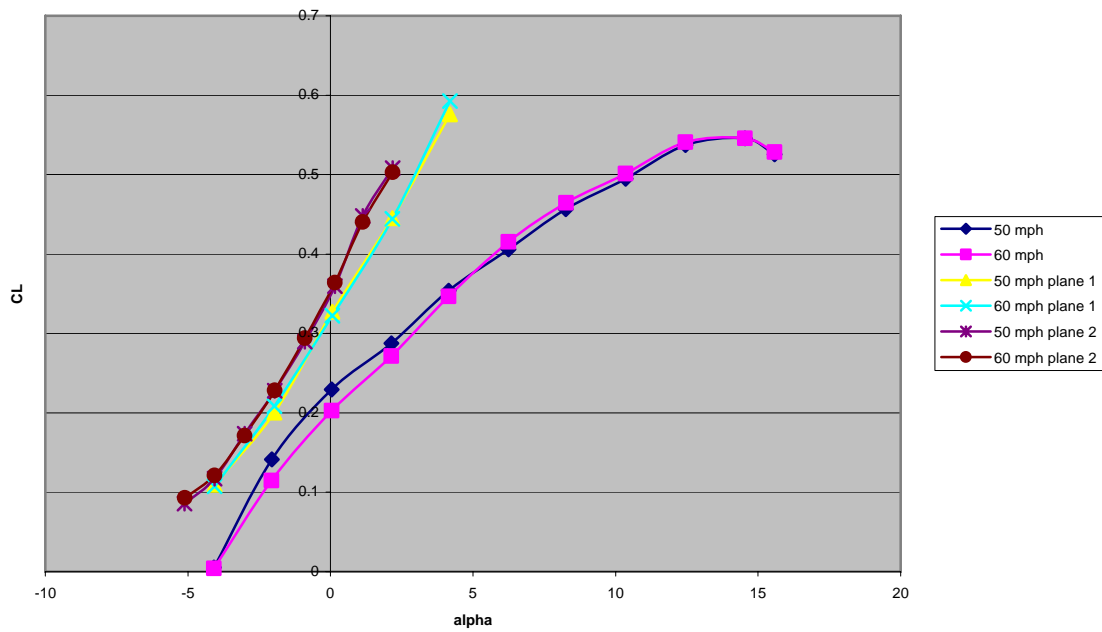


Figure 61. Front wing C_L vs α – $\lambda = 30$ deg IGE.

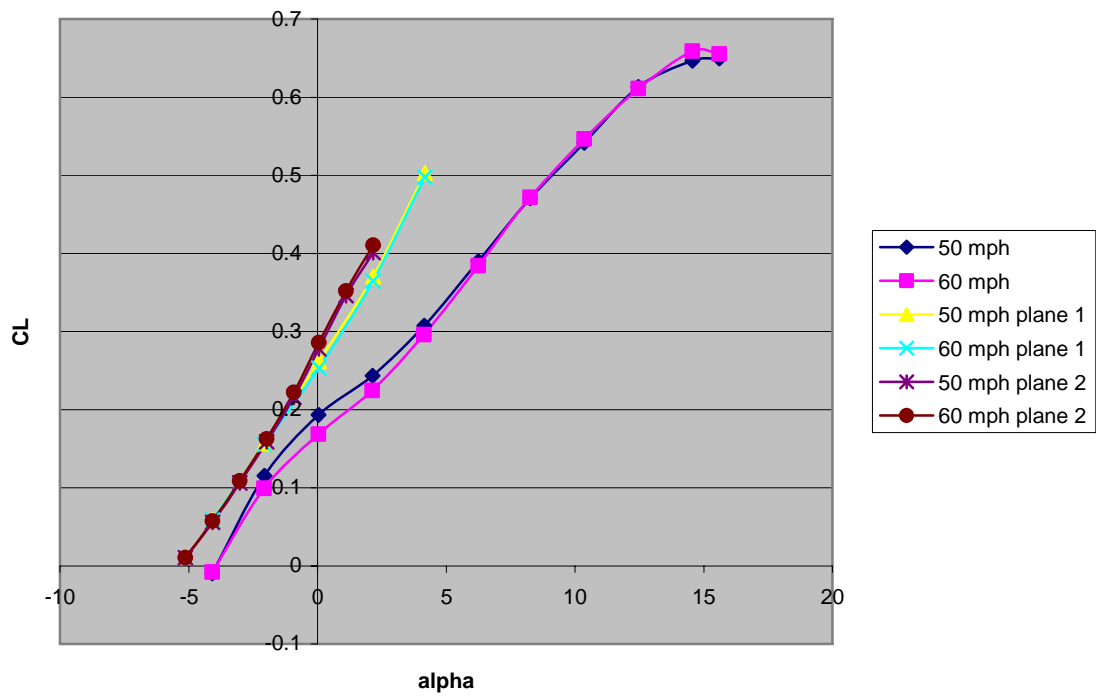


Figure 62. Front wing C_L vs α – $\lambda = 45$ deg IGE.

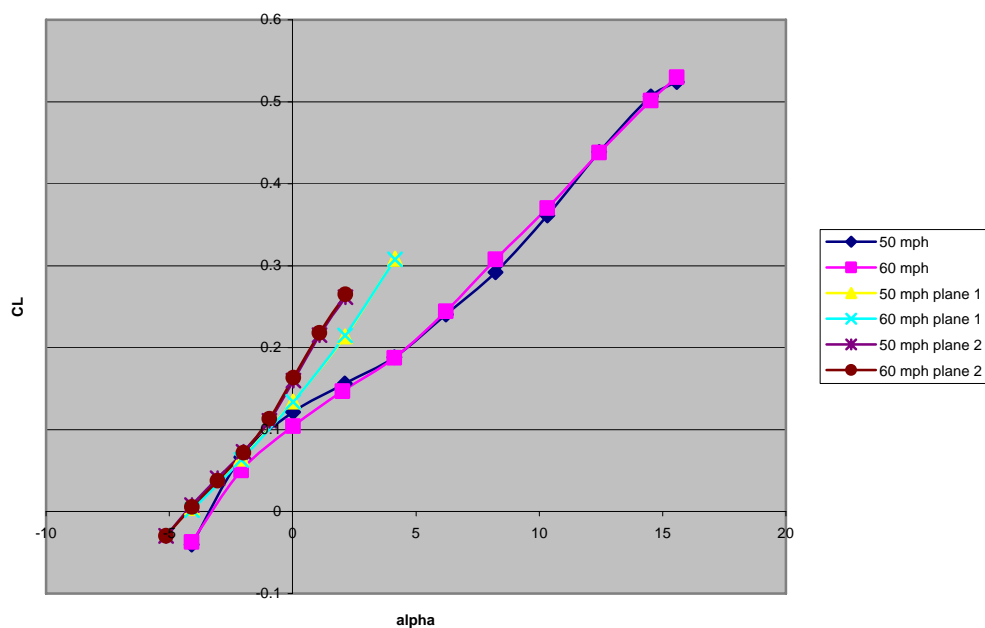


Figure 63. Front wing C_L vs α – $\lambda = 60$ deg IGE.

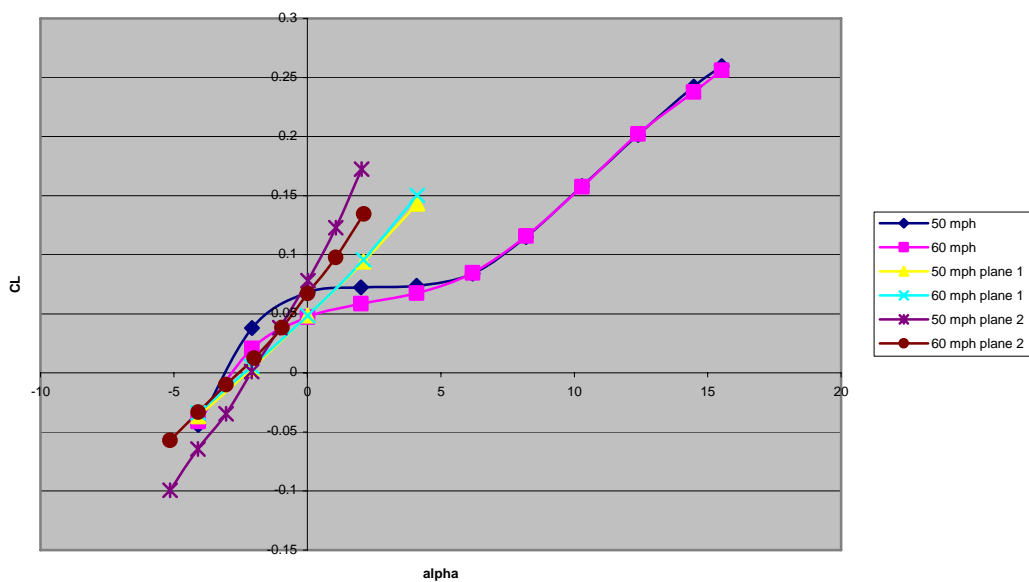


Figure 64. Front wing C_L vs α – $\lambda = 75$ deg IGE.

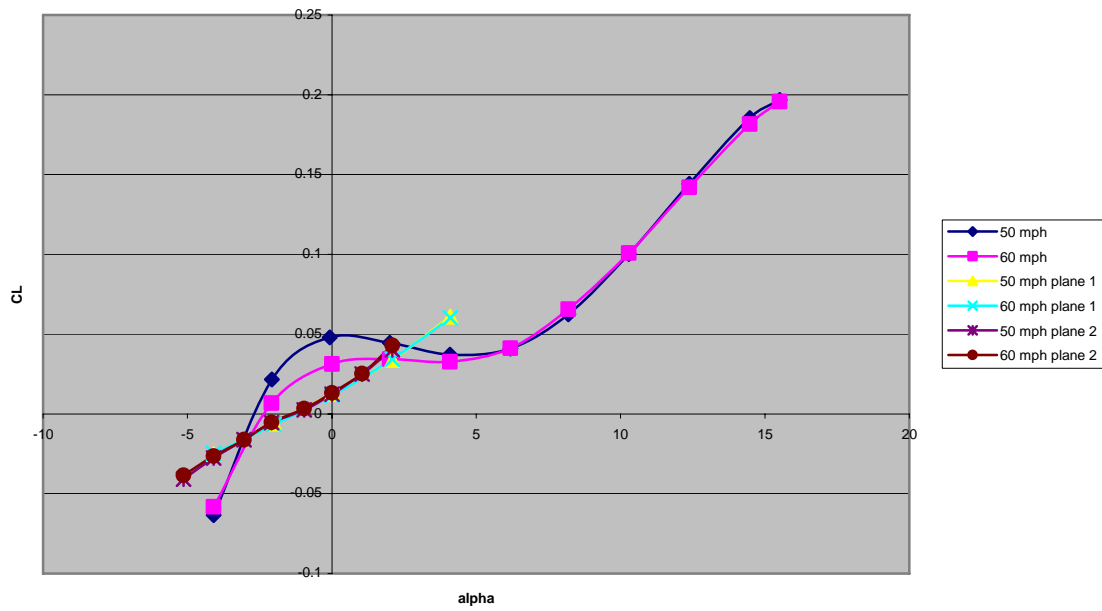


Figure 65. Front wing C_L vs α – $\lambda = 90$ deg IGE.

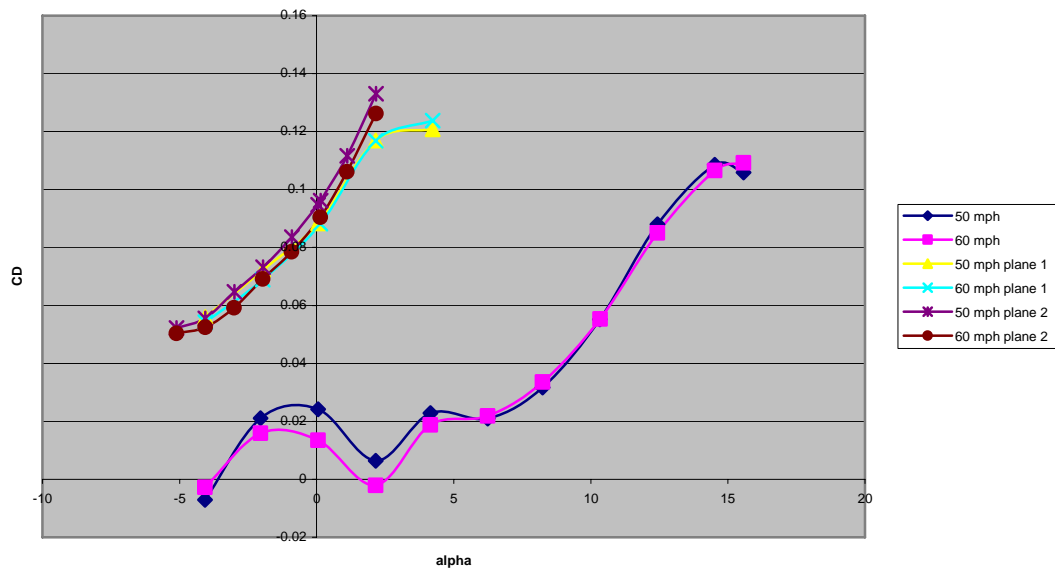


Figure 66. Front wing C_D vs α – $\lambda = 0$ deg IGE.

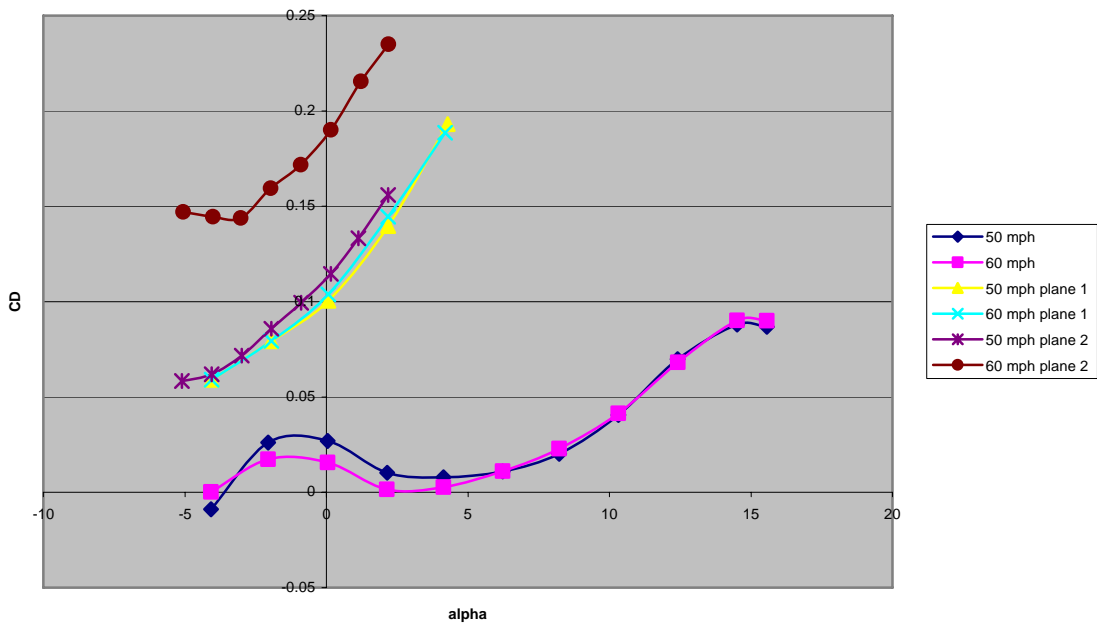


Figure 67. Front wing C_D vs α – $\lambda = 15$ deg IGE.

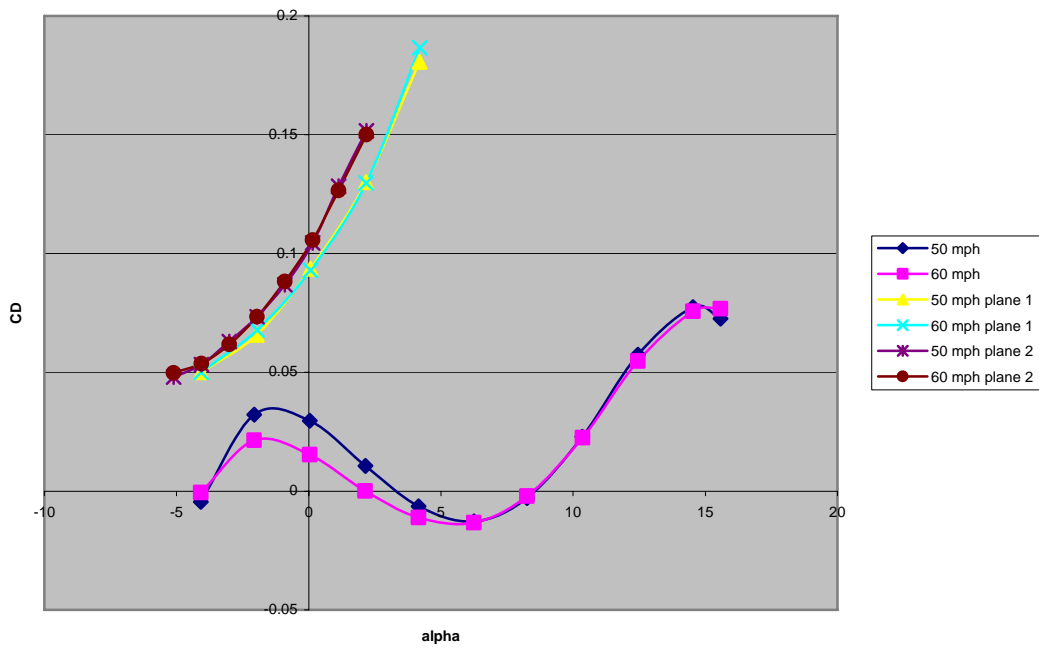


Figure 68. Front wing C_D vs α – $\lambda = 30$ deg IGE.

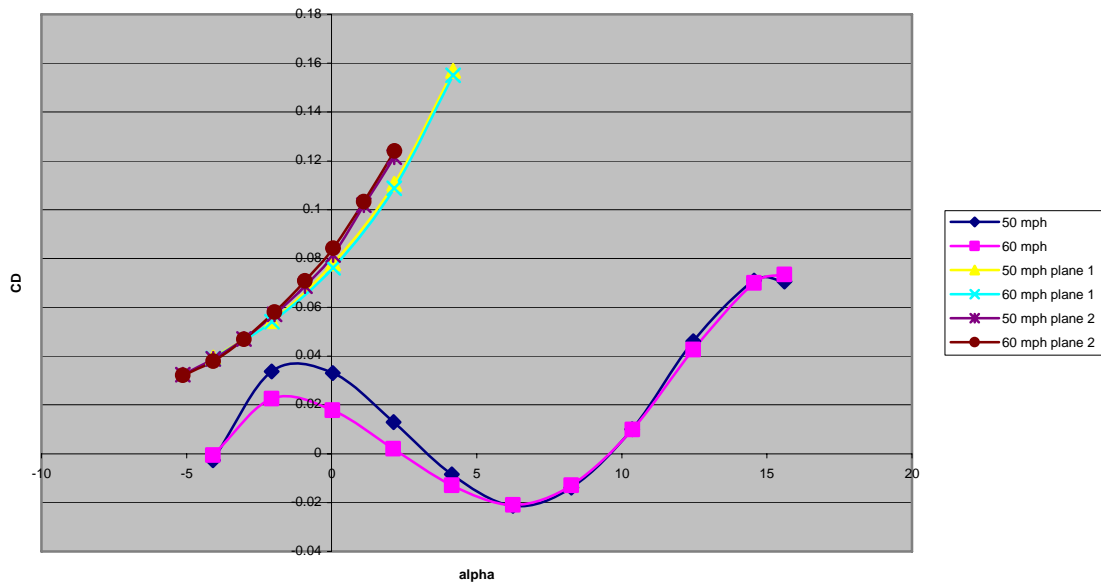


Figure 69. Front wing C_D vs α – $\lambda = 45$ deg IGE.

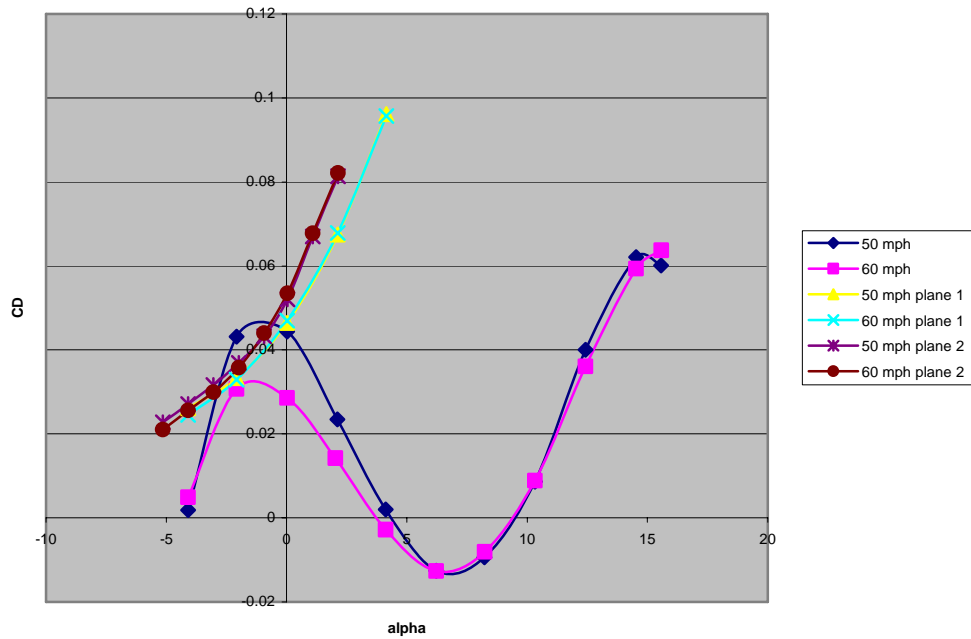


Figure 70. Front wing C_D vs α – $\lambda = 60$ deg IGE.

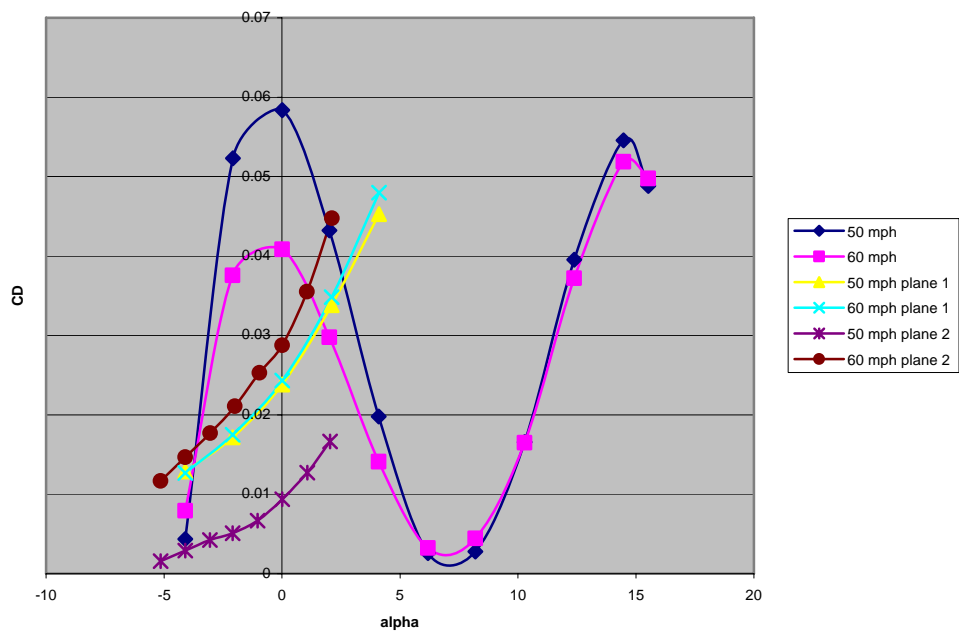


Figure 71. Front wing C_D vs α – $\lambda = 75$ deg IGE.

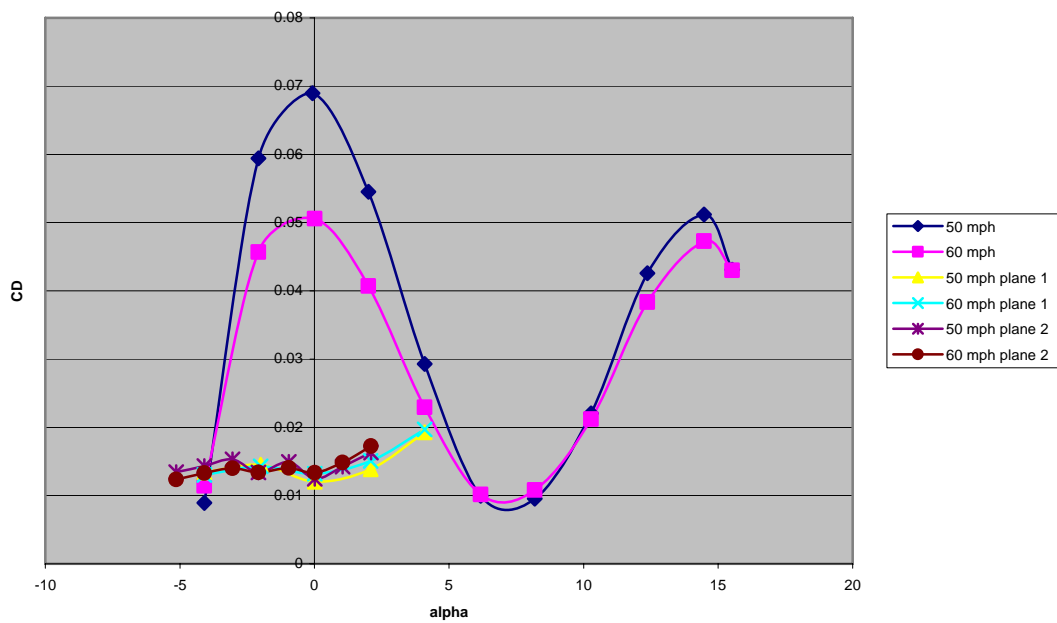


Figure 72. Front wing C_D vs α – $\lambda = 90$ deg IGE.

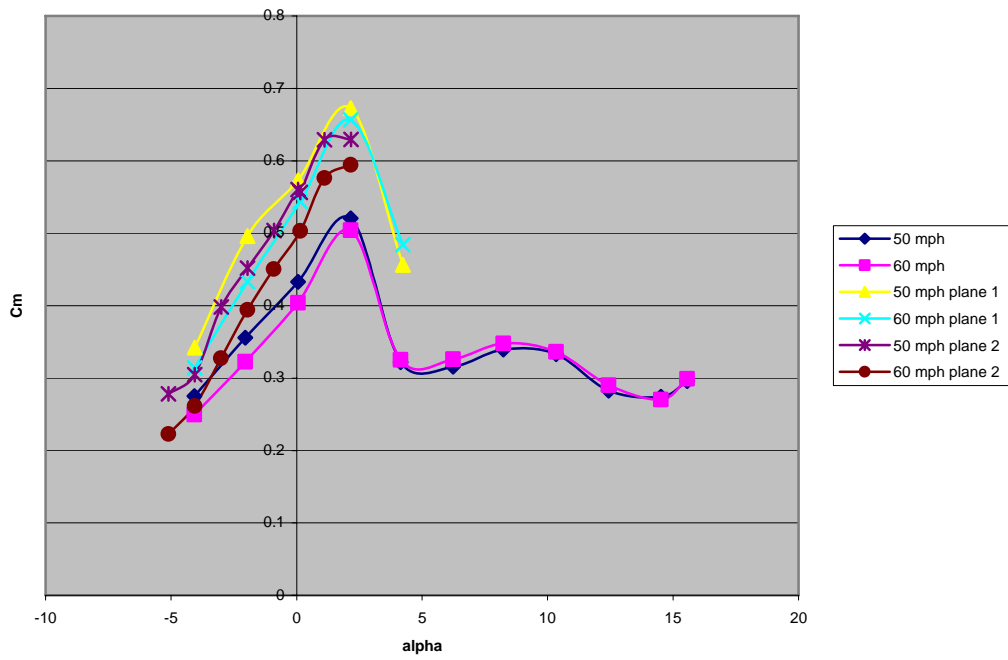


Figure 73. Front wing C_m vs α – $\lambda = 0$ deg IGE.

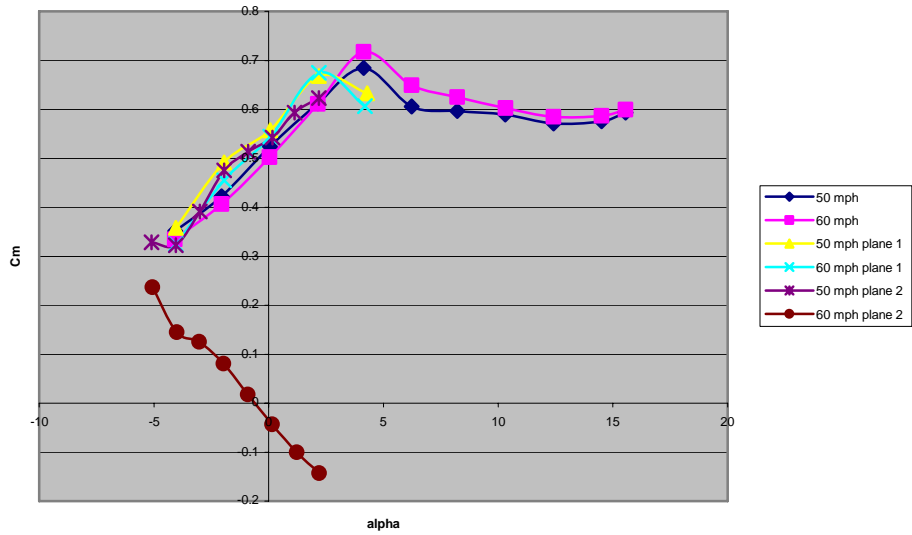


Figure 74. Front wing C_m vs α – $\lambda = 15$ deg IGE.

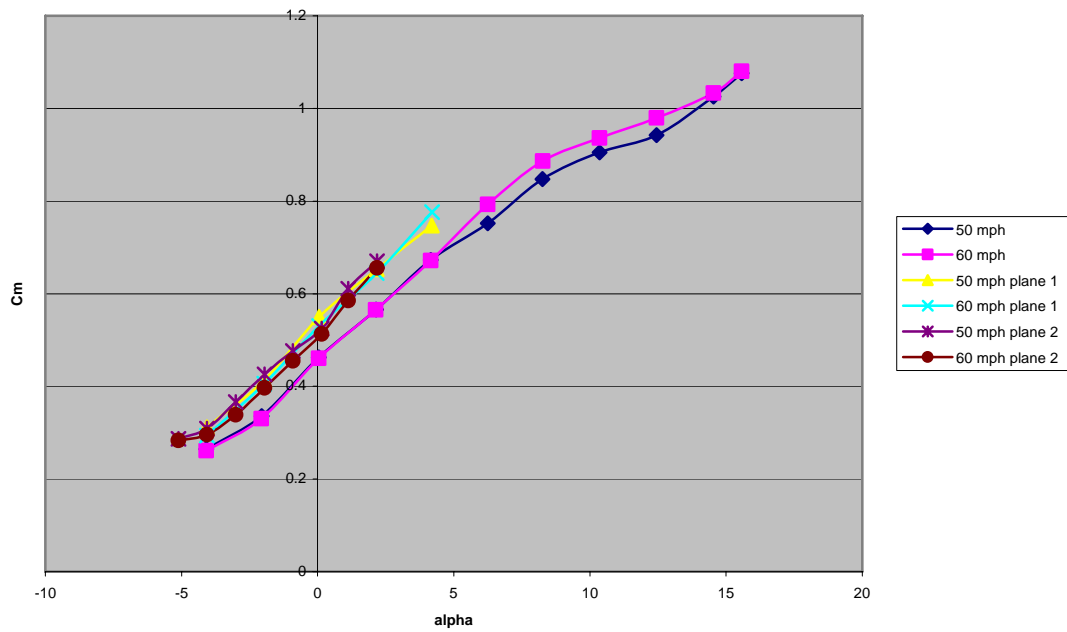


Figure 75. Front wing C_m vs α – $\lambda = 30$ deg IGE.

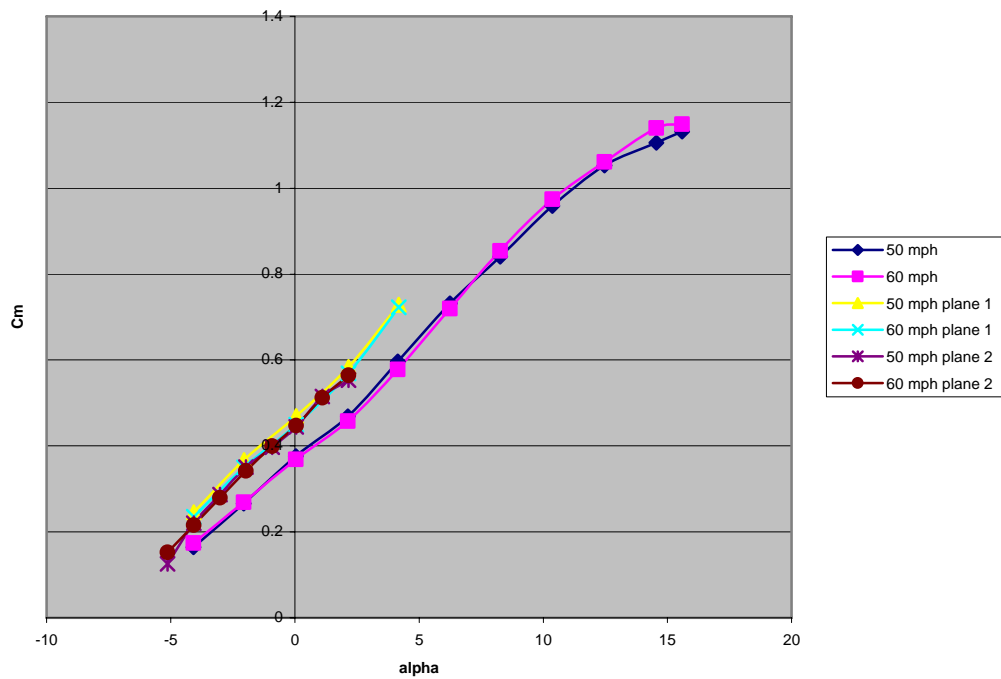


Figure 76. Front wing C_m vs α – $\lambda = 45$ deg IGE.

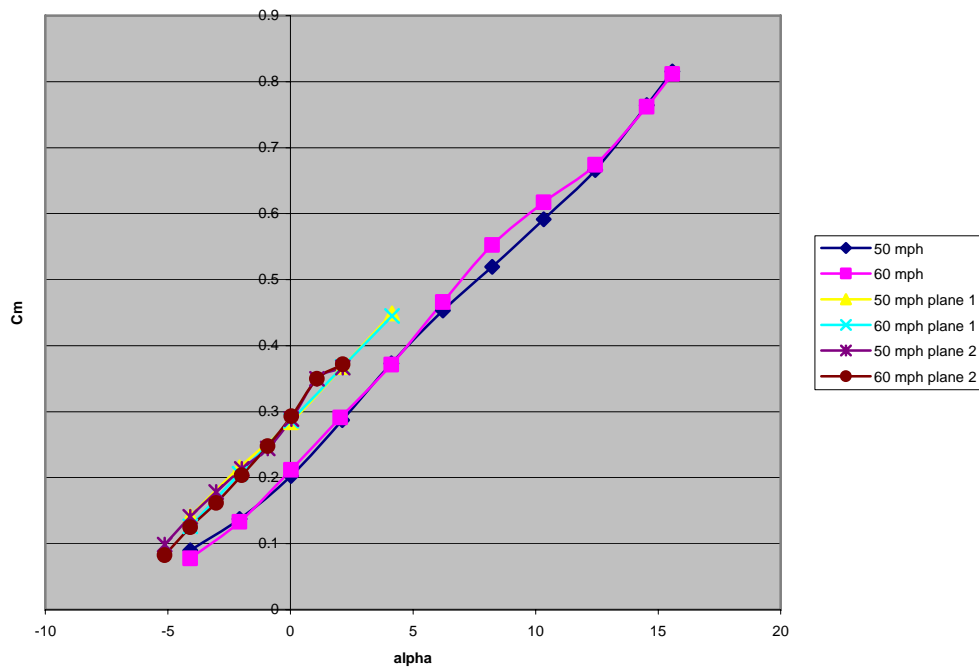


Figure 77. Front wing C_m vs α – $\lambda = 60$ deg IGE.

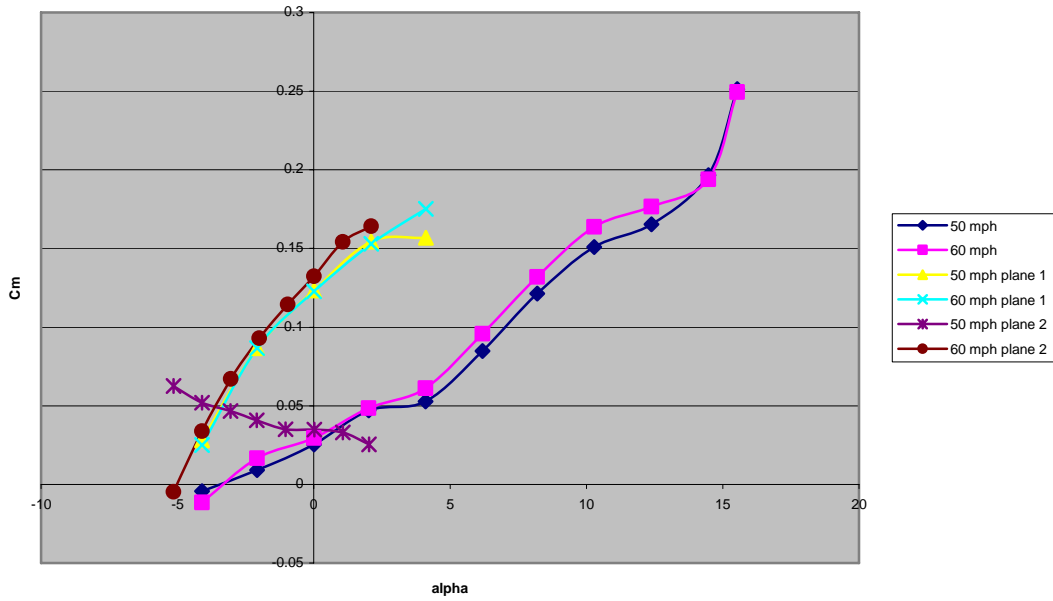


Figure 78. Front wing C_m vs α – $\lambda = 75$ deg IGE.

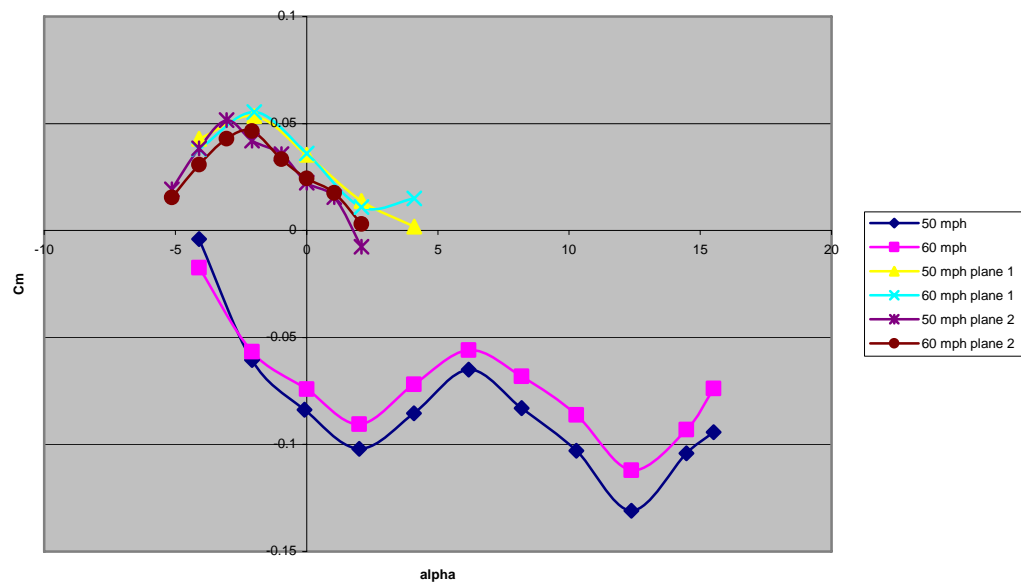


Figure 79. Front wing C_m vs α – $\lambda = 90$ deg IGE.

Appendix C: MATLAB Data Reduction Program

```

%*****
%*****
%*****      Lt. Dave Gebbie & Capt Anthony DeLuca      *****
%*****      Adapted fpr the Balance AFIT 1 by Lt. Rivera Parga*****
%*****      Calculation of Lift, Drag, Moments          *****
%*****      Re-adapted by Troy Leveron, ENS, USNR      *****
%***      Re-adapted by Brett Jones, ENS, USNR for UCAV Ground Effects Test***
%***      Re-adapted by Won In, Capt, USAF for UCAV Ground Effects Test*****
%***      Re-adapted by Matt Dillsaver, 1Lt, USAF for Oblique Wing Test*****
%*****Calculation of Lift, Drag, Moments*****
%*****
%*****

%This Code will transfer measured Forces and Moments on the balance to Wind
%(earth)centered frame of reference by correcting for tare effects,balance
%interactions, and wind tunnel irregularities, then plot lift and drag
%coefficients in as functions of AoA

clear; clc; format long;

%*****
%INPUT DECK
%FIRST FILL THE FOLLOWING INFORMATION
%*****

Masskg = 3.61;           %KGs
T_room = 73.1 + 459.67; %deg R  ****Changed for each day of testing****
P_barro = 29.2262 * 0.4911541; %Psi  *Changed for each day of testing****

% INPUT DATA FILE AND INPUT DATA TARE FILE
load MATT2OW0tareA_4to15B0.txt;           % Raw tare file to be read in.
TareFile=MATT2OW0tareA_4to15B0(:,1:9);
load MATT2OW0M50A_4to15B0.txt;           % Raw data file to be read in:
DataFile=MATT2OW0M50A_4to15B0(:,1:9);

%Offset distances from the Mounting Block to the Model C.G. (inches)

Y_cmb = 0.0;                                     %
X_cmb = 1.5625;           %inches (from origin @ balance center w/ + right)
Z_cmb = 0.0;           %inches (from origin @ balance center w/ + down)

%Required for the Solid Body blockage corrections due to wing and fuselage
Body_Volume = .4; %ft^3:
Wing_Area = 35/12^2; %ft^2

%*****
%I.- Room Conditions and Model Specifics
% Units are in ft, sec, lbm, psf, rankine, fps
%*****

Mass= (Masskg * 1000) * .0022046; % lbm
Gas_Const = 1716; % ft-lbf/slug-R
Density = (P_barro * 144)/(1716 * T_room); %lbm/ft^3 or lbf-s^2/ft^4
Root_Chord = 2/12 %ft
Span = 17.5/12 %ft
Aspect_Ratio = Span^2/Wing_Area;

```

```

Kinematic_Viscosity = .372e-6; %slug/ft-s
Speed_of_Sound = sqrt(1.4 * T_room * Gas_Const); %fps

%Distances between sensors (inches) to calculate moments

D1 = (2.10 / 2); D2 = D1; D3 = (1.7 / 2); D4 = D3; %inches

%*****
%II.-Solid Body Blockage corrections due to wing and fuselage (Pope pg 369)
%*****
K_1 = 1.12; % From fig. 10.2 assuming 4 digit airfoil and t/c=.15
delta = 0.122; % boundary correction factor (b/B) Ch 10
Tau_1 = 0.89; % factor from pg 369 fun. of tunnel shape and b/B
X_Section = (32/12)*(41/12) ; %ft^2
Wing_Volume = 29.6861/12^3 % ft^3
K_3 = 0.89;
Epsilon_sb_w = (K_1*Tau_1*Wing_Volume) / X_Section^(3/2);
Epsilon_tunnel_correction=1;
Epsilon_sb_b = (K_3*Tau_1*Body_Volume) / X_Section^(3/2);
Epsilon_tot = Epsilon_sb_w + Epsilon_sb_b+(Epsilon_tunnel_correction-1);

%*****
%VI. -CORRECT FORCES AND MOMENTS FOR BALANCE INTERACTIONS (BODY AXIS)
%*****

%Balance Interactions with off axis elements for the 25 lb balance
%Using average of the 25 lb calibration runs for N1 & N2 and the
%10 lb calibration for S1, S2 & A then normalizing by the actual
%sensor (N1, N2,...) in question. The sensor sequence in each row vector is:
%[N1 N2 S1 S2 A1 L2]

N1_I = ([1 -.010272 .01244 -.000593 .13758 .014914]);
N11 = N1_I(1,1);

N2_I = ([-.023 1 .00079 -.000296 .019354 .14516]);
N22 = N2_I(1,2);

S1_I = ([.002864 .00593 1 .002963 .089481 .000099]); S11 = S1_I(1,3);

S2_I = ([-.001576 .003939 -.026194 1 .028065 .007287]);
S22 = S2_I(1,4);

A_I = ([.209628 -.21866 .008038 -.007135 1 -.002077]);
A11 = A_I(1,5);

L_I = ([-.253931 -.239861 -.007284 .019533 .025824 1]);
L11 = L_I(1,6);

N1_normalized = (N1_I) .* [N11 N22 S11 S22 A11 L11].^(-1);
N2_normalized = (N2_I) .* [N11 N22 S11 S22 A11 L11].^(-1);
S1_normalized = (S1_I) .* [N11 N22 S11 S22 A11 L11].^(-1);
S2_normalized = (S2_I) .* [N11 N22 S11 S22 A11 L11].^(-1);
A_normalized = (A_I) .* [N11 N22 S11 S22 A11 L11].^(-1);
L_normalized = (L_I) .* [N11 N22 S11 S22 A11 L11].^(-1);

Interactions_Kij = [N1_normalized' N2_normalized' S1_normalized' S2_normalized'
A_normalized' L_normalized'];
%*****
%Load the static tare data for the alpha sweep w/o the wind , separate each
%force from the file, and fit a 4th order poly as an x-y plot (AoA vs.

```

```

%Force) for each of the 6 force sensors.
%*****

%load tare1.txt;      %raw tare data file to be read in
FILE=TareFile(:,1:9);

j=1;
k=1;
L=length(FILE);

for i=1:L                                %Run for all data points # of rows
    if i~=L                              %if current row is not last row, go to
next                                     %set next equal to the value of the
        NEXT=i+1;
    next row                             %set value2 as next row column 1
        VALUE2=FILE(NEXT,1);             %unless the it is the last value
    else if i==L                         %value2 set to 50 to end the sequence
        VALUE2=50;
    end
    end
    A(j,:)=FILE(i,:);                   %set row j of A equal to row i of FILE
    VALUE1=FILE(i,1);                   %set value1 equal to row i column 1 of
FILE                                     %if value1 equals value2, go to next
    if VALUE1==VALUE2
row                                     %if value1 and value2 are different
        j=j+1;
    else if VALUE1~=VALUE2               %if less than 20 values, ignored
check                                     %if more than 20 values
        if length(A(:,1))<5              %find length of A
due to angle change                     %Average all rows of the like
            j=1;
            clear A;
        else if length(A(:,1))>5
            C=length(A(:,1));
            for m=1:9
values in A                             %disregarding first 10 for
            B(k,m)=mean(A(4:C,m));        vibrations
            end
            j=1;
            k=k+1;
            clear A
        end
    end
end
end
end

if B(k-1,1)<B((k-2),1)
    B=B(1:(k-2),:);
end

tare=[B]
%*****End of Inserted Code*****
[row,col] = size(tare);

for k = 1:row
    theta_tare(k, :, :) = tare(k,1).*(pi/180);
    N1_tare(k, :, :) = tare(k,4);
    N2_tare(k, :, :) = tare(k,5);
    S1_tare(k, :, :) = tare(k,7);

```

```

S2_tare(k, :, :)      = tare(k, 8);
A_tare(k, :, :)      = tare(k, 6);
L_tare(k, :, :)      = tare(k, 9);

end

N1_poly = polyfit(theta_tare, N1_tare, 4);
N2_poly = polyfit(theta_tare, N2_tare, 4);
S1_poly = polyfit(theta_tare, S1_tare, 4);
S2_poly = polyfit(theta_tare, S2_tare, 4);
A_poly  = polyfit(theta_tare, A_tare, 4);
L_poly  = polyfit(theta_tare, L_tare, 4);

clear ('B', 'C', 'D', 'L')

%*****
%Load the specific test run files, subtract the effect of the static
%weight with the tare polynomials above, and correct for cross diagonal
%sensor interactions.
%*****

FILE=DataFile(:, :);      %Same as Above

j=1;
k=1;
L=length(FILE);

for i=1:L
    if i~=L
        next
        NEXT=i+1;
    next row
        VALUE2=FILE(NEXT, 1);
        else if i==L
            VALUE2=50;
        end
        end
        A(j, :)=FILE(i, :);
        VALUE1=FILE(i, 1);
        FILE
        if VALUE1==VALUE2
            row
                j=j+1;
            else if VALUE1~=VALUE2
                check
                    if length(A(:, 1))<5
                        due to angle change
                            j=1;
                            clear A;
                        else if length(A(:, 1))>5
                            values in A
                                C=length(A(:, 1));
                                for m=1:9
                                    vibrations
                                        B(k, m)=mean(A(4:C, m));
                                    end
                                    j=1;
                                    k=k+1;
                                    clear A
                                end
                            end
                        end
                    end
                end
            end
        end
    end
end

```

```

        end
    end

    if B(k-1,1)<B((k-2),1)
        B=B(1:(k-2),:)
    end

    sample_data=[B]

    %*****End of Inserted
    Code*****

    [row2,col2] = size(sample_data);

    for i = 1:row2

        %Angles of the model during test runs (Roll, Pitch {AoA}, Yaw {Beta}):

        phi = 0;
        theta(i,:) = sample_data(i,1) .* (pi/180); %radians
        si(i,:) = sample_data(i,2) .* (pi/180); %radians
        Wind_Speed(i,:) = sample_data(i,3) .* (5280/3600); %fps

        %Flight Parameters (Re#, Ma#, Dynamic Pressure):

        q = (.5 * Density) .* Wind_Speed.^2; %lbf/ft^2
        q_Corrected = q .* (1 + Epsilon_tot)^2; %lbf/ft^2
        Wind_Speed_Corrected = Wind_Speed .* (1 + Epsilon_tot); %fps
        Wind_Speed_Corrected_mph = Wind_Speed_Corrected .* (3600/5280);
        Mach_Number = Wind_Speed_Corrected ./ Speed_of_Sound; %NonDimensional
        Reynolds_Number = ((Density * Root_Chord) .* Wind_Speed_Corrected) ./
        Kinematic_Viscosity; %NonDimensional
        Flight_Parameters = [Mach_Number Reynolds_Number q_Corrected];

        %individual forces for each sensor:

        %NEW NOTATION

        N1_test(i,:,:) = sample_data(i,4);
        N2_test(i,:,:) = sample_data(i,5);
        S1_test(i,:,:) = sample_data(i,7);
        S2_test(i,:,:) = sample_data(i,8);
        A_test(i,:,:) = sample_data(i,6);
        L_test(i,:,:) = sample_data(i,9);
        %*****
        %V. Subtract the effect of static weight w/ tare polynomials above
        %*****

        %Evaluating the actual test theta angle (AoA) in the tare polynomial to
        %determine the tare values for the angles tested in each run.

        N1_eval = polyval(N1_poly,theta);
        N2_eval = polyval(N2_poly,theta);
        S1_eval = polyval(S1_poly,theta);
        S2_eval = polyval(S2_poly,theta);
        A_eval = polyval(A_poly,theta);
        L_eval = polyval(L_poly,theta);

        %The Time-Averaged (raw) forces N1, N2, S1, S2, A, L measurd in the wind
        %tunnel (body axis) with the tare effect of the weight subtracted off.

        N1_resolved = N1_test - (N1_eval);

```



```

N2_resolved = N2_test - (N2_eval);
S1_resolved = S1_test - (S1_eval);
S2_resolved = S2_test - (S2_eval);
A_resolved = A_test - (A_eval);
L_resolved = L_test - (L_eval);

Forces_minus_tare = [N1_resolved N2_resolved S1_resolved S2_resolved A_resolved
L_resolved]';

%Forces N1, N2, S1, S2, A, & L corrected for the balance interactions (body
axis)

Corrected_Data = (inv(Interactions_Kij) * Forces_minus_tare);

%*****
%Calculation of the Axial, Side, & Normal Forces from the corrected balance
%forces in the Body Axis reference frame
%*****

Forces_b(:,i) = [Corrected_Data(5,i); Corrected_Data(3,i) +
Corrected_Data(4,i); Corrected_Data(1,i) + Corrected_Data(2,i)];

%Calculation of the Drag, Side, & Lift Forces in the Wind Axis reference
%frame

Forces_w =
[Forces_b(1,:).*cos(theta').*cos(si')+Forces_b(2,:).*sin(si')+Forces_b(3,:).*si
n(theta').*cos(si');
-Forces_b(1,:).*sin(si').*cos(theta')+Forces_b(2,:).*cos(si')-
Forces_b(3,:).*sin(theta').*sin(si');
-Forces_b(1,:).*sin(theta')+Forces_b(3,:).*cos(theta')];

%First entry is the moments calculated by the balance or direct calculation
%in the Body Reference Frame. Balance measures Roll (l), Yaw is about the
%z-axis (n), and Pitch is about the y-axis (m). Distances from strain
%gages to C.G. are in INCHES. Moments are in-lbf

m = Corrected_Data(1,i) * D1 - Corrected_Data(2,i) * D2;
n = Corrected_Data(3,i) * D3 - Corrected_Data(4,i) * D4;
Moments_b(:,i) = [Corrected_Data(6,i); m; n];

%Second entry is the conversion from the "Balance Centeric" moments to the
%Wind Reference monments with respect to the Balance Center (bc)

Moments_w_bc = [Moments_b(1,:).*cos(theta').*cos(si')-
Moments_b(2,:).*sin(si')+Moments_b(3,:).*sin(theta').*cos(si');

Moments_b(1,:).*sin(si').*cos(theta')+Moments_b(2,:).*cos(si')+Moments_b(3,:).*
sin(theta').*sin(si');
-Moments_b(1,:).*sin(theta')+Moments_b(3,:).*cos(theta')];

%Finally, the balance centered moments are converted to moments about the
%Model's Center of Mass (cm) or Center of Gravity (CG)

cgdist=sqrt((X_cmb)^2+(Z_cmb)^2); %Obtaining the direct distance between the
%center of the balance and the center of
mass
w=atan(-Z_cmb/X_cmb); %Obtaining the angle between cgdist and the x axes at
zero angle of attack

X_cm(i,:) = cos(theta(i,:)+w)*cos(si(i,:))*(cgdist);
Y_cm(i,:) = Y_cmb + X_cm(i,:)*tan(si(i,:)); % appropriate for very
small y_cmb and reasonable si

```

```

Z_cm(i,:)= -sin(theta(i,:)+w)*(cgdist);

Moments_w_cg_u = [Moments_w_bc(1,:) + Z_cm(i,:)*Forces_w(2,:) + Forces_w(3,:)*
Y_cm(i,:);
                    Moments_w_bc(2,:) - X_cm(i,:)*Forces_w(3,:) + Forces_w(1,:)*
Z_cm(i,:);
                    Moments_w_bc(3,:) - Y_cm(i,:)*Forces_w(1,:) - Forces_w(2,:)*
X_cm(i,:)];

%*****
%Calculation of the actual Lift and Drag nondimensional Coefficients,
%uncorrected for tunnel effects, (Cl and Cd)
%*****

C_L_u = Forces_w(3,:) ./ (q_Corrected' .* Wing_Area); %Keuthe & Chow pg 178
C_D_u = Forces_w(1,:) ./ (q_Corrected' .* Wing_Area);
C_Y_u = Forces_w(2,:) ./ (q_Corrected' .* Wing_Area);
Coefficients = [C_L_u; C_D_u; C_Y_u]';

% Ave_Cl = mean(Coefficients(:,1));
% Ave_Cd = mean(Coefficients(:,2));

end

%*****
%***** Drag Coefficient Correction *****
%*****

C_D_o = min(Coefficients(:,2));
C_L_u_sqrd = Coefficients(:,1).^2;
Delta_C_D_w = ((delta * Wing_Area) / X_Section) .* C_L_u_sqrd;
C_D_Corrected = C_D_u' + Delta_C_D_w;

%*****
%***** Angle of Attack due to upwash Correction *****
%*****

alpha = sample_data(:,1);
Delta_alpha_w = ((delta * Wing_Area) / X_Section) .* (57.3 * C_L_u);
alpha_Corrected = alpha + Delta_alpha_w';

%*****
%***** Pitching Moment Correction *****
%*****

Cl_w_cg = Moments_w_cg_u(1,:) ./ (q_Corrected' .* (Wing_Area * Span*12));
Cm_w_cg_u = Moments_w_cg_u(2,:) ./ (q_Corrected' .* (Wing_Area * c_bar*12));
Cn_w_cg = Moments_w_cg_u(3,:) ./ (q_Corrected' .* (Wing_Area * Span*12));
Cm_w_cg_corrected = Cm_w_cg_u; % - Delta_C_m_cg_t';
Corrected_Moment_Coefficients = [Cl_w_cg' Cm_w_cg_corrected' Cn_w_cg'];

%*****
%**Obtaining moments coefficients corrected about the center of the balance
%*****

Cl_w_bc = Moments_w_bc(1,:) ./ (q_Corrected' .* (Wing_Area * Span * 12));
Cm_w_bc_u = Moments_w_bc(2,:) ./ (q_Corrected' .* (Wing_Area * c_bar * 12));
Cn_w_bc = Moments_w_bc(3,:) ./ (q_Corrected' .* (Wing_Area * Span * 12));

Cm_w_bc_corrected=Cm_w_bc_u;
Corrected_Moment_Coefficients_bc=[Cl_w_bc' Cm_w_bc_corrected' Cn_w_bc'];

%*****
%*****Output Variables Formatting*****

```

```

%*****

alpha = sample_data(:,1);

C_Y\r');
YY=[Flight_Parameters (Wind_Speed_Corrected .* (3600/5280)) alpha_Corrected
C_L_u' C_D_Corrected Corrected_Moment_Coefficients C_Y_u']%pressure]
wklwrite('output.xls',YY,2,1)

Max_Cl = max(Coefficients(:,1));

figure;
plot(alpha_Corrected,Coefficients(:,1),'b.-');
legend('100 mph ','\beta \approx 0\circ');
grid on;
title('\it C_L vs \alpha no winglets (50
mph)','FontWeight','bold','FontSize',11); xlabel('Angle of Attack (\alpha)');
ylabel('Lift Coefficient (C_L)');

```

References

1. Hirschberg, Michael J., Hart, David M., and Buetner, Thomas J. "A Summary of a Half-Century of Oblique Wing Research," *45th AIAA Aerospace Sciences Meeting and Exhibit*, AIAA 2007-150, 8-11 January 2007.
2. Jones, R.T., "Aerodynamic Design for Supersonic Speeds," *Proceedings of the 1st International Congress in the Aeronautical Sciences (ICAS), Advances in Aeronautical Sciences*, Vol 1., Pergamon Press, NY, 1959.
3. Kroo, I.M., "The Aerodynamic Design of Oblique Wing Aircraft," *Proceedings of the AIAA/AHS/ASEE Aircraft Systems Design and Technology Meeting*, CP 86-2624, AIAA, Washington D.C., 1986.
4. Wikipedia contributors, 'Oblique wing', *Wikipedia, The Free Encyclopedia*, http://en.wikipedia.org/w/index.php?title=Oblique_wing&oldid=107164503
5. Jones, Brent L., "Experimental Investigation into the Aerodynamic Ground Effect of a Tailless Chevron-Shaped UCAV." MS thesis, AFIT/GAE/ENY/05J-04. Department of Aeronautics and Astronautics, Air Force Institute of Technology (AU), Wright-Patterson AFB OH, June 2005.
6. Pendleton, Linda D., "Ground Effect," *AV Web*, Aviation Publishing Group, 2005. <http://www.avweb.com/news/airman/185905-1.html>.
7. van Opstal, Edwin and others. *The WIG Page*. <http://www.se-technology.com/wig/index.php>.
8. Cole, William. "The Pelican: A Big Bird for the Long Haul," *Boeing Frontiers Online*, http://www.boeing.com/news/frontiers/archive/2002/september/i_pw.html.
9. Jones, R.T., "Technical Note: The Flying Wing Supersonic Transport," *Aeronautical Journal*, March 1991.
10. Campbell, J.P., and Drake, H.M., "Investigation of stability and control characteristics of an airplane model with a skewed wing in the Langley free flight tunnel." NACA TN 1208, May 1947.
11. Kempel, R.W., McNeill, W.E., and Maine, T.A., "Oblique-Wing Research Airplane Motion Simulation with Decoupling Control Laws," *AIAA 26th Aerospace Sciences Meeting*, AIAA-88-0402, 11-14 January 1988.
12. Halloran, Michael and O'Meara, Sean, "Wing in Ground Effect Craft Review," DSTO-GD-0201.
13. Wieselsberger, C. "Wing Resistance Near the Ground," NACA TM 77, 1922.

14. McCormick, Barnes W. *Aerodynamics, Aeronautics, and Flight Mechanics*. New York: John Wiley & Sons, Inc., 1995.
15. Raymond, Arthur E. "Ground Influence on Aerofoils," NACA TN 67, 1921.
16. Schweikhard, William. "A Method for In-flight Measurement of Ground Effect on Fixed-Wing Aircraft," *Journal of Aircraft*, 4 (2): 101-104 (March-April 1967).
17. Chang, Ray Chung and Muirhead, Vincent U. "Effect of Sink Rate on Ground Effect of Low-Aspect-Ratio Wings," *Journal of Aircraft*, 24 (3): 176-180 (March 1986).
18. Baker, Paul A., Schweikhard, William G., and Young, William R. "Flight Evaluation of Ground Effect on Several Low-Aspect-Ratio Airplanes," NASA TN D-6053, 1970.
19. Lee, Pai Hung, Lan, C. Edwards, Muirhead, Vincent U. "An Experimental Investigation of Dynamic Ground Effect," NASA CR 4105, 1987.
20. Curry, Robert E. "Dynamic Ground Effect for a Cranked Arrow Wing Airplane," NASA TM 4799, 1997.
21. Curry, Robert E. and Owens, Lewis R., "Ground-Effect Characteristics of the Tu-144 Supersonic Transport Airplane," NASA TM 2003-212035, 2003.
22. Turner, Thomas R., "Endless-belt Technique for Ground Simulation," *Proceedings of Conference on VSTOL/STOL Aircraft*, NASA SP 116, Paper 25: 445, 1966.
23. Kemmerly, Guy T. and Paulson, John W., "Investigation of a Moving-Model Technique for Measuring Ground Effects." NASA TM 4080, 1989.
24. Deluca, Anthony M., "Experimental Investigation into the Aerodynamic Performance of Both Rigid and Flexible Wing Structured Micro-Air-Vehicles." MS thesis, AFIT/GAE/ENY/04-M06. Department of Aeronautics and Astronautics, Air Force Institute of Technology (AU), Wright-Patterson AFB OH, March 2004.
25. Dike, Christopher, A "Wind Tunnel Investigation of Joined Wing Scissor Morphing." MS thesis, AFIT/GAE/ENY/06J-02. Department of Aeronautics and Astronautics, Air Force Institute of Technology (AU), Wright-Patterson AFB OH, June 2006.
26. Corneille, Jennifer, "Wind Tunnel Investigation of Joined Wing Configurations." MS thesis, AFIT/GAE/ENY/99J-02. Department of Aeronautics and Astronautics, Air Force Institute of Technology (AU), Wright-Patterson AFB OH, June 1999.
27. *EDEN 333*. Technical Specifications. Stratasys Inc. © 2003. 3 May 2005. http://www.stratasys.com/NA/pdfs/PS_eden333.pdf.

28. *FullCure*TM 700 Series. Technical Specifications. Stratasys Inc. © 2005. 25 March 2005. http://www.stratasys.com/NA/pdfs/Eden_FullCure700.pdf.
29. In, Won, "Experimental Investigation into the Aerodynamic Ground Effect of a Tailless Chevron and Lambda-Shaped UCAVs." MS thesis, AFIT/GAE/ENY/06M16. Department of Aeronautics and Astronautics, Air Force Institute of Technology (AU), Wright-Patterson AFB OH, March 2005.
30. Gebbie, David A., "Experimental Study of the Subsonic Aerodynamics of a Blended Wing Body Air Vehicle with a Focus on Rapid Technology Assessment." MS thesis, AFIT/GAE/ENY/05-M09. Department of Aeronautics and Astronautics, Air Force Institute of Technology (AU), Wright-Patterson AFB OH, March 2005.
31. Nelson, Robert C. *Flight Stability and Automatic Control*. New McGraw Hill, Inc., 1998.
32. Barlow, Jewel B., Rae, William H. Jr., and Pope, Alan. *Low-Speed Wind Tunnel Testing*. New York: John Wiley & Sons, Inc., 1999.
33. Class Notes, AERO 517. Air Force Institute of Technology, Summer 2006.
34. Tang, L., Liu, D., and Chen, P. "Extension of Projectile Range Using Oblique-Wing Concept." *AIAA 23rd Applied Aerodynamics Conference*, AIAA 2005-4600, June 2005.

Vita

Captain Matthew J. Dillsaver was born in Tulsa, OK. He graduated from Booker T. Washington High School in 1998. He then entered The University of Oklahoma where he earned a Bachelor's of Science in Mechanical Engineering. After college he attended Officer Training School at Maxwell AFB, AL and was commissioned in February 2003.

His first assignment was at Tinker AFB in the KC-135 Systems Program Office where he was a Mechanical Systems Engineer. He was also an Aircraft Battle Damage Repair Engineer which allowed him to deploy to Southwest Asia in January 2005. In August 2005, he entered the Graduate School of Engineering and Management, Air Force Institute of Technology. Upon graduation, he will be assigned to the Air Force Seek Eagle Office at Eglin AFB.

REPORT DOCUMENTATION PAGE				Form Approved OMB No. 074-0188	
<p>The public reporting burden for this collection of information is estimated to average 1 hour per response, including the time for reviewing instructions, searching existing data sources, gathering and maintaining the data needed, and completing and reviewing the collection of information. Send comments regarding this burden estimate or any other aspect of the collection of information, including suggestions for reducing this burden to Department of Defense, Washington Headquarters Services, Directorate for Information Operations and Reports (0704-0188), 1215 Jefferson Davis Highway, Suite 1204, Arlington, VA 22202-4302. Respondents should be aware that notwithstanding any other provision of law, no person shall be subject to a penalty for failing to comply with a collection of information if it does not display a currently valid OMB control number.</p> <p>PLEASE DO NOT RETURN YOUR FORM TO THE ABOVE ADDRESS.</p>					
1. REPORT DATE (DD-MM-YYYY) 22 Mar 07		2. REPORT TYPE Master's Thesis		3. DATES COVERED (From – To) 22 Aug 06 – 22 Mar 07	
4. TITLE AND SUBTITLE Experimental Investigation of Oblique Wing Aerodynamics at Low Speed				5a. CONTRACT NUMBER	
				5b. GRANT NUMBER	
				5c. PROGRAM ELEMENT NUMBER	
6. AUTHOR(S) Dillsaver, Matthew, J., Captain, USAF				5d. PROJECT NUMBER	
				5e. TASK NUMBER	
				5f. WORK UNIT NUMBER	
7. PERFORMING ORGANIZATION NAMES(S) AND ADDRESS(S) Air Force Institute of Technology Graduate School of Engineering and Management (AFIT/EN) 2950 Hobson Way WPAFB OH 45433-7765				8. PERFORMING ORGANIZATION REPORT NUMBER AFIT/GAE/ENY/07-M10	
9. SPONSORING/MONITORING AGENCY NAME(S) AND ADDRESS(ES) AFRL/VAAA Attn: Mr. Carl Tilmann Bldg 45, RM 2624077 WPAFB OH 45433-7765 DSN: 785-4539				10. SPONSOR/MONITOR'S ACRONYM(S)	
				11. SPONSOR/MONITOR'S REPORT NUMBER(S)	
12. DISTRIBUTION/AVAILABILITY STATEMENT APPROVED FOR PUBLIC RELEASE; DISTRIBUTION UNLIMITED.					
13. SUPPLEMENTARY NOTES					
14. ABSTRACT <p>In an effort to increase the range of missiles and guided bombs, the USAF is looking at options for new wing configurations. One such configuration being considered is oblique wings. An oblique wing is a wing that pivots about a point on the aircraft fuselage thereby having one side swept forward and the other swept aft. Additional interest is looking at a wing only configuration that also rotates with one wing tip forward of the other. Studies have shown that this configuration can provide less drag for a given lift at both supersonic cruise and subsonic loiter conditions. This experiment focused on the low speed performance of a missile model with an oblique wing. The wing was tested at seven different sweep angles and at two different speeds. In order to simulate the missile dropping from an aircraft the model was inverted over a stationary ground plane in the tunnel and tested at the same wing obliquity angles. Stalling was found at certain conditions including sweep angles of 0, 15, and 30 deg. The ground plane was shown to result in an increase in lift as well as an increase in drag. The ground plane was also shown to add more longitudinal stability, thus making the missile better performing when dropped from an aircraft.</p>					
15. SUBJECT TERMS Oblique Wing, Ground Effect, Weapon Separation, Aerodynamics					
16. SECURITY CLASSIFICATION OF:			17. LIMITATION OF ABSTRACT UU	18. NUMBER OF PAGES 103	19a. NAME OF RESPONSIBLE PERSON Dr. Milton Franke
REPORT U	ABSTRACT U	c. THIS PAGE U			19b. TELEPHONE NUMBER (Include area code) (937) 255-6565, ext 4720; e-mail: Milton.franke@afit.edu